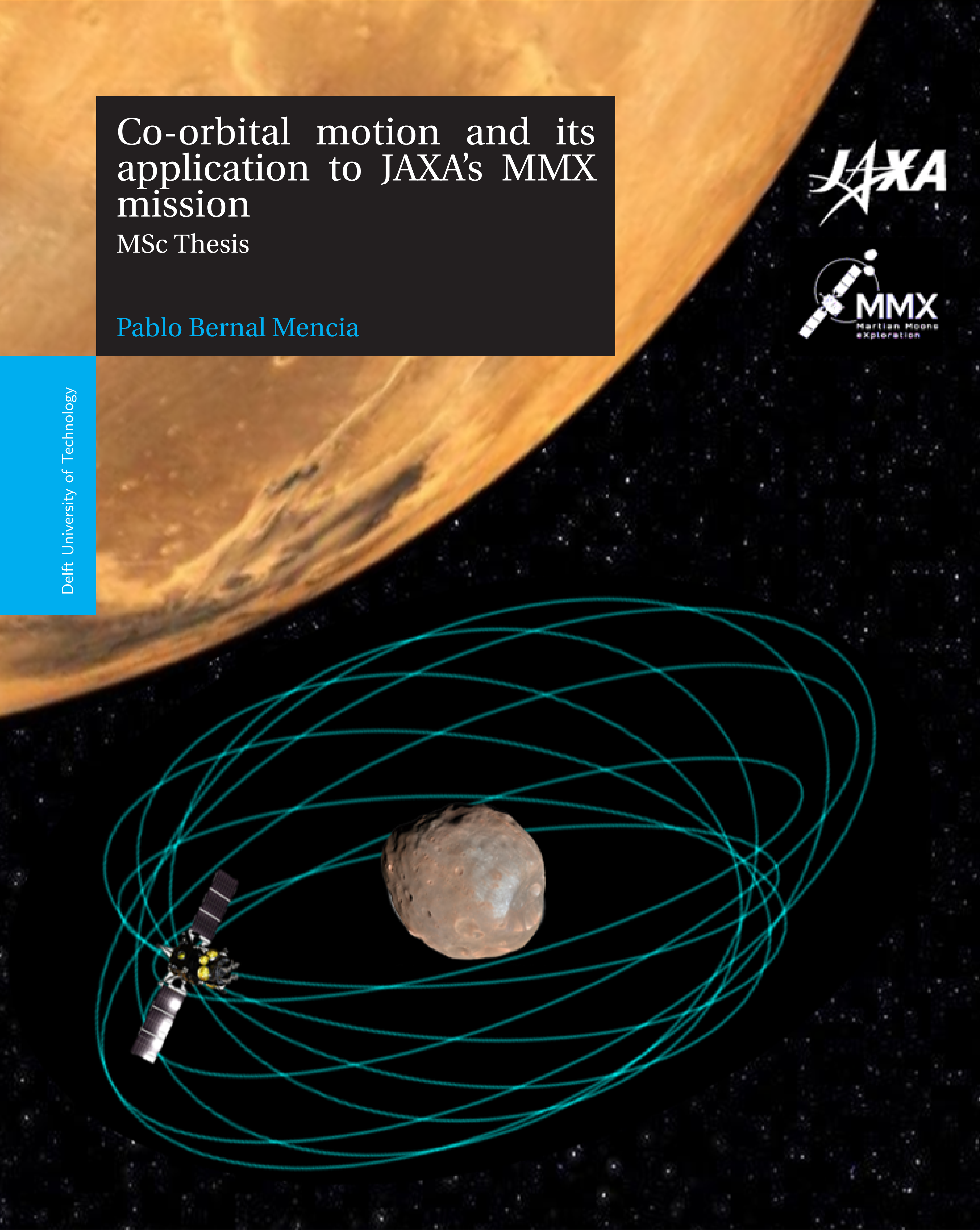

Co-orbital motion and its application to JAXA's MMX mission

MSc Thesis

Pablo Bernal Mencia

Delft University of Technology

Challenge the future

Co-orbital motion and its application to JAXA's MMX mission

MSc Thesis

by

Pablo Bernal Mencia

in partial fulfillment of the requirements for the degree of

Master of Science

in Aerospace Engineering

at Delft University of Technology,

to be defended publicly on Wednesday December 12, 2018 at 9:00 AM.

Student number:	4624580
Supervisor:	Ir. Noomen
Thesis committee:	Prof. Visser
	Prof. Kawakatsu
	Dr. Van Horssen
	Ir. Noomen

Delft University of Technology

Preface

This thesis is the result of the collaboration of the Delft University of Technology and the Institute of Astronautical and Space Sciences of JAXA, whose support has been crucial for the success of the project. In particular, the supervision of Ir. Noomen and Prof. Kawakatsu, together with the strong collaboration of Dr. Baresi, has been inestimable. I would like to take this opportunity to acknowledge their complete support and commitment to my work, without which this thesis would never have been possible.

Pablo Bernal Mencia
Delft, December 2018

SUMMARY

In the framework of JAXA's MMX mission to explore the Martian moon of Phobos, an analysis of the stability of three-dimensional quasi-satellite orbits in the Mars-Phobos circular restricted three-body problem was conducted. For this analysis, notions of co-orbital motion, interpreted as the slow motion of the guiding center of the trajectory along the disturbing potential of Phobos, were used. After identifying and analyzing different regions of stability for three quasi-satellite orbits at 100, 50 and 30 km from the center of Phobos, several conclusions were drawn regarding the dynamics of the ballistic escape of the spacecraft, interpreted in terms of co-orbital motion. By making use of these insights, a novel methodology to find periodic quasi-satellite orbits able to reach high latitudes over the surface of Phobos was derived. This methodology consists of two steps: a multi-objective minimization using co-orbital parameters as target functions, to isolate regions with potential periodic orbits; followed by a shooting algorithm to arrive at the final periodic orbit. As a result of this new methodology, two periodic orbits were found at 50 and 30 km from the center of Phobos, able to reach latitudes as high as 54° and 32° respectively. This resulting orbits represent an important contribution to both the operations and the scientific return of the Phobos proximity phase within MMX. Moreover, the innovative methodology to search for periodic orbits proposed here has potential to be generalized for different missions, not just around Phobos but also for other planetary systems such as the Earth-Moon.

Contents

List of Abbreviations

2D	Two-Dimensional
3D	Three-Dimensional
AU	Astronomical Unit
BVP	Boundary Value Problem
CNES	Centre National d'Etudes Spatiales
CR3BP	Circular Restricted Three-Body Problem
DePhine	Deimos and Phobos Interior Explorer
DRO	Distant Retrograde Orbit(s)
ER3BP	Elliptical Restricted Three-Body Problem
HiRISE	High Resolution Imaging Science Experiment
HSO	Horseshoe Orbit
ISAS	Institute of Space and Astronautical Science
JAXA	Japanese Aerospace eXploration Agency
KPI	Key Performance Index
MMX	Martian Moons eXploration
MRO	Mars Reconnaissance Orbiter
MSc	Master of Science
NSGA-II	Elitist Non-dominated Sorting Genetic Algorithm
PADME	Phobos And Deimos and Mars Environment
PPP	Phobos Proximity Phase
PRIME	Phobos Reconnaissance and International Mars Exploration
PRR	Preliminary Requirements Review
RK45	Runge-Kutta 4(5)
QSO	Quasi-Satellite Orbit
SLSQP	Sequential Least Squares Quadratic Programming
STM	State Transition Matrix
TPO	TadPole Orbit

NOMENCLATURE

LATIN SYMBOLS

a	Semi-major axis [km or non-dimensional]
b	Stability index
C_j	Jacobi constant
e	Eccentricity
GM	Mass times the universal gravitational constant [$km^3 s^{-2}$]
i	Inclination [°]
$\mathscr{I}_{6\times 6}$	6×6 eye matrix
j	Imaginary unit
L_k	Lagrange point k
n	Mean motion
r_{min}	Minimum distance
$\mathbf{r}_1$	Position vector of the third body from the first primary
$\mathbf{r}_2$	Position vector of the third body from the second primary
R_{mean}	Mean radius
R	Disturbing function
$\mathbf{s}$	State
T	Period [days, hours or revolutions]
U_g	Gravitational potential
X_0	Initial value of the variable X
X_{av}	Average value of the variable X
X_{slow}	$slow$ component of the variable X

GREEK SYMBOLS

ϵ	Small quantity
Φ	State transition matrix
λ	Eigenvalue
μ	Mass parameter
σ	Standard deviation
τ	True anomaly of second primary [rad]

1

INTRODUCTION

Martian Moons Exploration (MMX) is a space mission under development by the Institute of Space and Astronautical Sciences (ISAS) of the Japanese Aerospace Exploration Agency (JAXA). MMX will be launched in 2024 targeting the Martian system, with the goal of unveiling the origin of the Martian moons Phobos and Deimos, which is still one of the most intriguing mysteries of the Solar System. For this, MMX will orbit around Phobos from a safe distance for as long as about three years, investigating and characterizing the moon before launching several rovers to its surface and retrieving a sample from its soil. This Phobos Proximity Phase (PPP) is therefore the longest stage of the MMX mission and clearly the most challenging in terms of orbit design and maintenance. The present thesis will be focused on this part of the MMX mission, aiming to contribute to the design of the orbits for the MMX spacecraft around Phobos.

Due to its tiny mass and small density, combined with its proximity to Mars, Phobos has a sphere of influence which is embedded within its own surface, which means that there is no possibility to orbit the moon in a Keplerian-like manner. Therefore, a three-body solution is required to safely remain in the vicinity of Phobos for a long time. Since also the Lagrange colinear points are very close to the surface, Halo or Lyapunov orbits are not safe enough to maintain them for a long time. In this context, Quasi-Satellite Orbits (QSO's) –also known as Distant Retrograde Orbits (DRO's)– are clearly the most suitable solution. QSO's are a particular type of co-orbital or 1:1 resonant motion where the spacecraft orbits the first primary (Mars) under the perturbation of the second primary (Phobos) in such a way that, on a synodic frame, a spacecraft describes an ellipse-like retrograde trajectory centered on the second primary.

The dynamics around Phobos are very uncertain, not only because of the combined attraction of Phobos and Mars, but also due to uncertainties such as the very irregular and still not well determined gravity field of the moon. Because of this, the approach to be followed by MMX will be to use planar QSO's around Phobos for most of the duration of the PPP, whose dynamics are better understood and predictable, making the orbit easier to maintain. Nevertheless, in order to correctly characterize the moon's surface and gravity, improving not only the scientific return of the mission but also the robustness of the navigation and landing site selection, a three-dimensional QSO will be required. In this sense, periodic and stable 3D QSO's are the safest and most robust solution, however the search for those is very challenging because of the high number of independent variables together with the absence of analytic tools.

Through the use of the concepts defined for the first time by Namouni [1], co-orbital motion can be interpreted in terms of a guiding center of the spacecraft, slowly moving in the bosom of the averaged disturbing potential of the moon. The existence of an additional quasi-constant of the averaged motion makes this theory interesting for the study of Tadpole orbits (TPO's), Horseshoe orbits (HSO's) and QSO's. Nevertheless, these co-orbital concepts have never been applied to the orbit design of a space mission such as MMX. For this reason and in line with the necessities of the PPP of MMX highlighted before, the goal of this thesis is to exploit the theory of co-orbital motion to extract insights about the stability and periodicity of three-dimensional QSO's around Phobos. The research question that this thesis aims solve is:

How can co-orbital motion be applied to the search of periodic and stable three-dimensional Quasi-Satellite orbits around Phobos?

In order to give an answer to this question, several orbits located in different regions and energy levels around Phobos were studied aiming to correlate their stability and periodicity with their co-orbital parameters. Using the insights resulting from this analysis, a novel methodology to find periodic 3D QSO's with high inclination was proposed. This approach uses a multi-objective optimization with certain co-orbital parameters as target functions, in order to identify regions where a potential periodic orbit might exist. By using orbits in those regions as first guess for a conventional shooting algorithm, periodic QSO's were identified at 30 and 50 km far from the surface of Phobos, able to reach latitudes as high as 32° and 54° respectively.

The innovation of this thesis lays on the application of co-orbital motion theory (typically used in astronomy) for mission design of a real mission such as MMX. The relevance of the results of this work is twofold: First, the proposition of a novel strategy to search periodic orbits in the Circular Restricted Three-Body Problem (CR3BP). Second, the discovery of two periodic and stable orbits able to reach high latitudes over Phobos, which will be further studied by ISAS regarding the actual mission design of MMX.

The report is structured as follows. First, a brief overview of the context of the MMX and its PPP will be provided in Chapter 2. Second, the mathematical background of the thesis will be provided in Chapters 3 and 4. Chapter 3 will be focused on the dynamics model used for orbit propagation, introducing the expressions of the equations of motion, the Jacobi constant and the state transition matrix in curvilinear coordinates. Chapter 4 will verse on the theory of co-orbital motion that will later be used to interpret the QSO dynamics. Concepts such as guiding center, disturbing function and adiabatic invariant will be introduced in this chapter. Third, after setting the introduction and mathematical background of the problem, Chapters 5 and 6 will deal with the analysis of the stability of the three-dimensional QSO's for the three levels of energy to be flown by MMX. Chapter 5 will introduce the concept of the time-to-escape map and show the results of a bifurcation analysis to find periodic three-dimensional QSO's. On the other hand, Chapter 6 will focus on applying the theory introduced in Chapter 4 to the study of the stability in the various regions of the time-to-escape maps. Fourth, based on the conclusions extracted from the analyses conducted in Chapters 5 and 6, Chapter 7 will present the methodology to find periodic QSO's on the stability islands of the time-to-escape map. The resulting two periodic orbits found on the stability islands of QSO-M and QSO-L will be presented and examined here. Finally, overall conclusions will be drawn in Chapter 8, followed by recommendations for further work proposed in Chapter 9. Additionally, two appendices can be found at the end of the report, dealing with the validation of some of the tools used for this work, and providing additional figures omitted from the main body of the report for readability reasons.

2

Martian Moons Exploration

MMX is a mission currently being developed by ISAS/JAXA, targeting the Martian moon of Phobos, and with Deimos as a secondary target [2]. At the moment, the mission is at its Phase A (accepted proposal) and very close to its Preliminary Requirements Review (PRR). MMX is a sample-return mission and, as such, it inherits from renowned preceding JAXA missions like Hayabusa [3] and Hayabusa-2 [4]. The mission design of MMX is also supported by the French Centre National d'Etudes Spatiales (CNES).

2.1. Mars-Phobos system

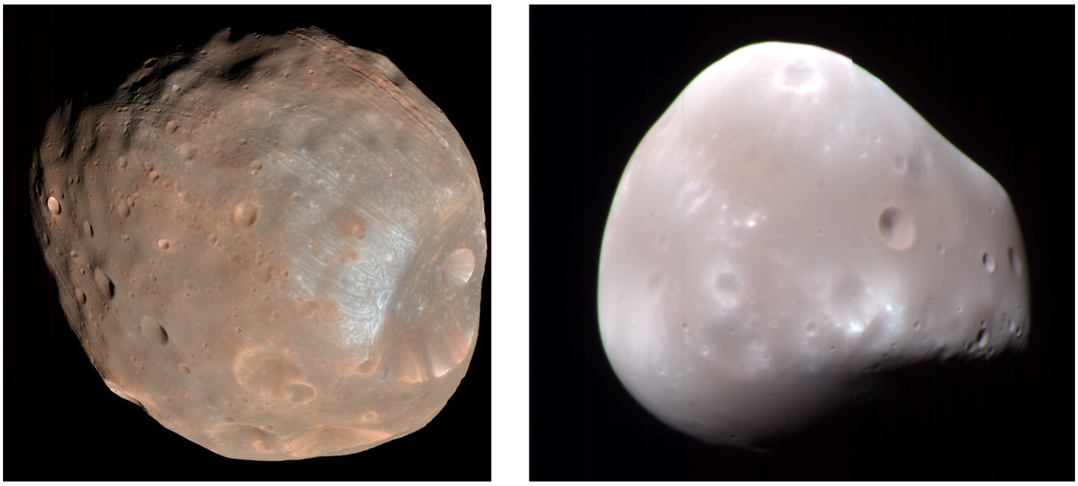

Figure 2.1: Photographs of the Martian moons Phobos (left) and Deimos (right) taken by the *High Resolution Imaging Science Experiment* (*HiRise*) onboard the *Mars Reconnaissance Orbiter* (*MRO*). Credits: NASA/JPL/University of Arizona.

Mars is stably orbited by two tiny satellites named Phobos and Deimos, which are the primary and secondary targets of MMX. Fig. 2.1 shows images of these two Martian moons, as taken by the HiRISE camera onboard MRO. As shown, the appearance of the surface differs substantially between both moons: while Phobos has a reddish color and is highly populated by craters, Deimos has a much smoother surface with a lighter color. The phenomena behind this different morphology are thought to be past secondary impacts of ejecta coming from the surface of Mars towards Phobos, which is very close to the surface of the Red Planet [5]. This intimate connection between Phobos and Mars is the reason why this moon was selected as the major target of MMX. For this reason, Deimos will not be further addressed in this study. The most relevant physical parameters of Phobos and Mars, as well as their respective orbits are summarized in Table 2.1.

Table 2.1: Physical and orbital parameters in the Mars-Phobos system [6].

	Mars	**Phobos**
a [km]	$2.28 \cdot 10^8$	9377.2
T	687 days	7.65 h
e	0.0934	0.0156
i [°]	1.8488	1.0668
GM [$km^3 s^{-2}$]	42828.37	0.0007113901872
R_{mean} [km]	3396.0	11.1

2.2. PAST MISSIONS

Two reasons have traditionally motivated missions to the Martian moons: their unclear origin, further explained in the next section, and their potential to support future manned missions to Mars [7]. Landing and setting up a base on Phobos is far less expensive than doing so in Mars, because of its tiny mass and its abundance of water. From a space base located there, astronauts would be able to control rovers on the Martian surface in real time, with no communication delay.

For these two reasons, there have been several attempts to study Phobos and Deimos in the past. In 1988 and for the first time, two space missions belonging to the Soviet *Phobos program* were launched in order to investigate the Martian moon [8]: Phobos 1 and Phobos 2. However, both missions failed before completing their goals. Phobos 1 was lost along its interplanetary course due to an error in the attitude control system, while Phobos 2 failed just before the release of two rovers over the surface of the moon [9]. Nevertheless, Phobos 2 managed to obtain several images of the Martian moon before its critical failure, one of which is presented in Fig. 2.2.

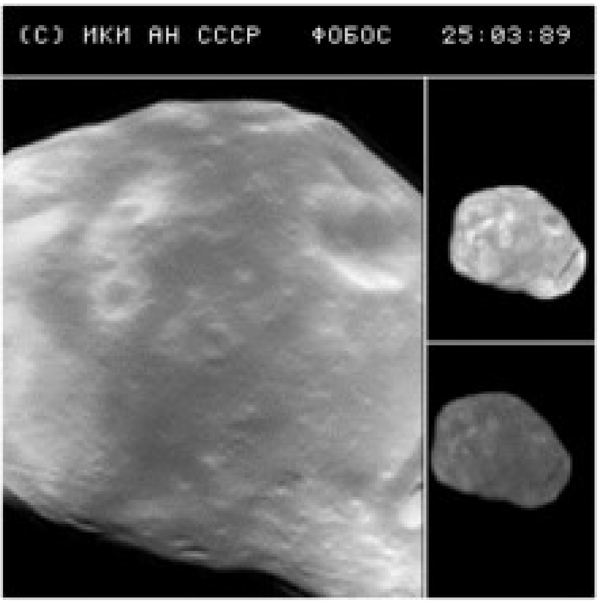

Figure 2.2: Image of Phobos taken by the *Phobos 2* probe before its critical failure [10].

In 2011, decades after the failure of the *Phobos program*, the Russian spacecraft Phobos-Grunt was launched aiming to return a sample from the surface of Phobos [11]. The goals and profile of the Phobos-Grunt mission were very similar to the ones of MMX (see Section 2.3), with the exception of leaving part of the lander after the sample-return, to continue studying Phobos' surface for about a year. Despite the failure of Phobos-Grunt, because of an error in the propulsion system along its interplanetary course, the heritage of this mission has motivated future missions to the Martian moons such as MMX, and other proposals like PRIME [12], Phobos Surveyor [13], PADME [14] or DePhine [15].

2.3. GOALS, SPECIFICATIONS AND PHASES

The origin of the Martian moons is at the moment one of the mysteries in the Solar System, as there are contradictory clues that point towards different explanations. The leading two theories are [16]:

- **Capture:** Early estimations of the composition and density of the bodies suggested that the Martian moons could be actually captured carbonaceous chondritic asteroids [17]. If that were the case, Phobos and Deimos would likely have been formed in the Main Belt, beyond the snow line, and then have migrated inwards. After that, they would have been captured by Mars' gravity and atmospheric drag [18][19][20][21].

- **Impact:** Other observations on the composition however point at a formation of the Martian moons from a circum-Martian accretion disk originated by a large collision with Mars [22][23].

Motivated by this discrepancy, the mission goal of MMX is to unveil the origin of the Martian moons, by sampling the surface of Phobos and returning the sample back to Earth. MMX is set for launch in the summer of 2024, with a total dry mass of about 3500 kg and a ΔV budget of 5 km/s. The overall duration of the mission is about five years, of which the first and last one will be spent on the interplanetary trip from the Earth to the Martian system and back. Hence, three years of the mission duration will be spent on the PPP, while MMX will be performing close observations of Phobos and sampling the surface of the moon. The PPP it is the phase of MMX on which the present study is focused, so a full additional section is devoted to this stage.

2.4. PPP MISSION DESIGN

Due to the small mass parameter of Phobos, combined with its proximity to Mars (see Tab. 2.1), the Hill's sphere of the moon is located within its surface, which makes orbiting the moon in a Keplerian way impossible. Because of the proximity of the Lagrangian points L_1 and L_2 to the surface, Halo and Lyapunov orbits are undesired for a 3-years long PPP around Phobos [24]. By contrast, QSO's are very stable and can be designed to be periodic at a safe distance from the surface of the moon, which makes them the most suitable kind of orbit for the PPP of MMX [24].

2.4.1. PERIODIC PLANAR QSO

In the planar case ($z = \dot{z} = 0$) it is possible to obtain periodic and neutrally stable QSO's at any altitude over Phobos [25]. Although there is no guarantee of maintaining this stability in higher-fidelity models, literature confirms that some of these planar QSO's are able to remain quasi-periodic for weeks [24][26]. For this reason, together with the superior knowledge of planar QSO dynamics when compared with the three-dimensional case [27], the current design of the PPP of MMX has three planar periodic QSO's as baseline [28].

Fig. 2.3 shows the required relationship between the initial values of ρ and $\dot{\theta}$ (see Section 3.3) to achieve periodicity in a planar QSO around Phobos, when fixing the remaining coordinates at zero. This family of planar periodic QSO's can be retrieved through a shooting method followed by a continuation technique, as explained in [29][30]. As shown, in the planar case there is freedom to chose the amplitude of the orbit, achieving periodicity in all cases. Of this continuous set of potential solutions, the current plan of MMX is to fly three planar QSO's at different altitudes, in order to gradually characterize the gravitational environment of Phobos. As the accuracy of the model of the gravitational field of Phobos is improved, the spacecraft will move to a lower altitude QSO with increased reliability of the navigation system. The three baseline QSO's to be flown by MMX are:

QSO-H: High QSO, with a minimum distance of 100 km to the center of Phobos.

QSO-M: Medium QSO, with a minimum distance of 50 km to the center of Phobos.

QSO-L: Low QSO, with a minimum distance of 30 km to the center of Phobos.

The three periodic and planar QSO's to be flown by MMX are depicted in Fig. 2.4 for visual comparison. Section 2.4.2 explains in further detail the characteristics of these three orbits.

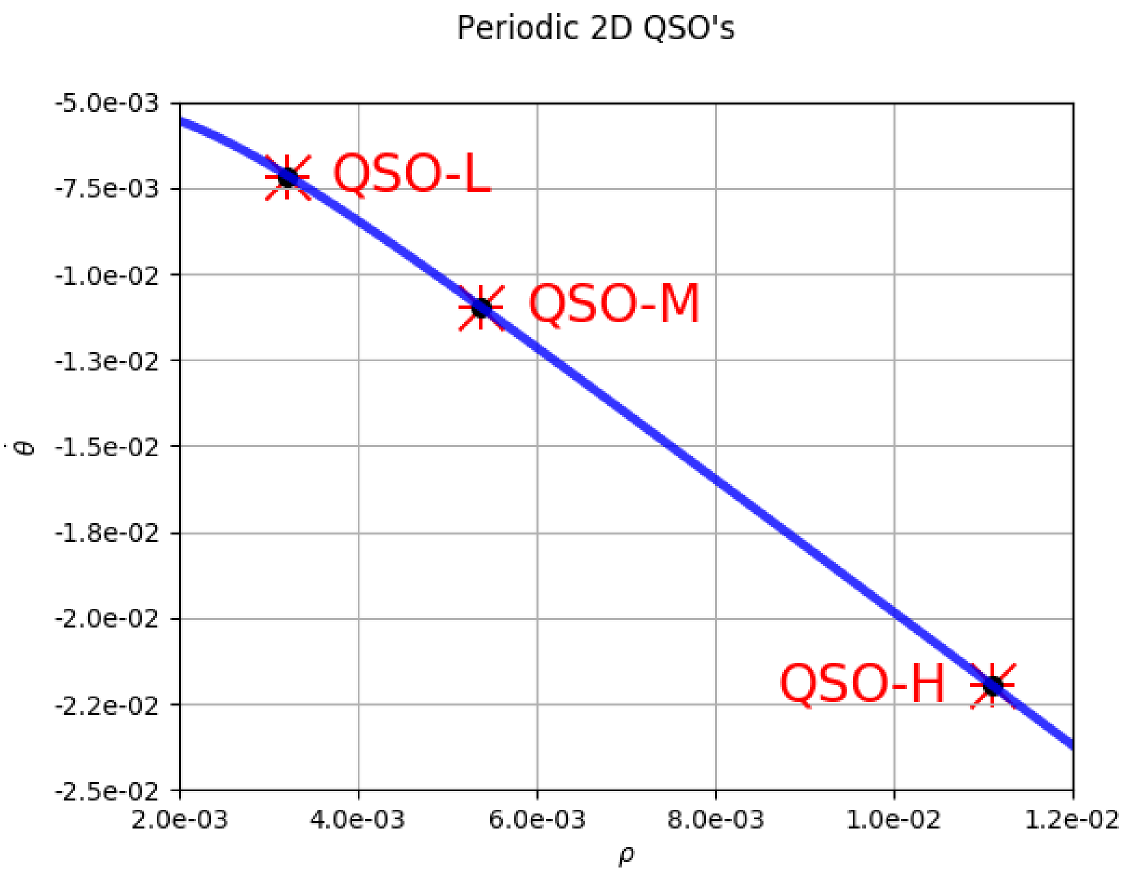

Figure 2.3: Initial conditions for $\theta = z = \dot{\rho} = \dot{z} = 0$, leading to periodic QSO on the equatorial plane of Phobos. Nominal QSO's of MMX highlighted in red.

2.4.2. BASELINE MMX QSO

As introduced in Section 2.4.1, MMX will make use of three nominal QSO's at different altitudes over the surface of Phobos, of 100, 50 and 30 km from the center of the moon as shown in Fig. 2.4. The initial conditions and mean orbital elements of these orbits are summarized in Tab. 2.2. As shown, when the size of the QSO decreases, so does the period of the orbit, as already noted in [28][31]. Nevertheless, when the orbit is sufficiently large, the period is very close to one orbital revolution of Phobos. The mean and initial eccentricity of the orbits also decrease with the size of the QSO, since this is the major parameter governing the amplitude of the fast motion (i.e. the amplitude of the QSO) [32][33]. On the contrary, the Jacobi constant C_j increases as the size of the QSO goes down, because the gravitational potential of Phobos is stronger as the distance of the orbit to its center decreases.

The shape of the slow disturbing function (see Chapter 4) in the three baseline QSO's of MMX is depicted in Fig. 2.5. The guiding center in all three orbits is located at the bottom of the QSO valley and it has no kinetic energy (see Eq. (4.12)) so it always remains there while the spacecraft moves around it. To be noted is the fact that these slow disturbing functions are all very symmetric in θ_{slow}. Due to the gravitational term in the definition of the disturbing function, the smaller the QSO, the closer is the spacecraft to the center of Phobos, so the higher the value of the slow disturbing function at the location of the guiding center. Regarding the maxima of the function, their location is governed by the eccentricity of the orbit (see Section 4.2), so they are further apart from Phobos as the size of the QSO increases. Although Fig. 2.5 seems to suggest that the values of the peaks is also smaller the larger the QSO, due to the numerical construction of the figure, this is not the case. At the location of the peaks, all three functions tend to infinity, because the inclination is in all cases zero. Nevertheless, it is true that the increase in the slow disturbing function close to its asymptotes is sharper the larger the amplitude of the QSO.

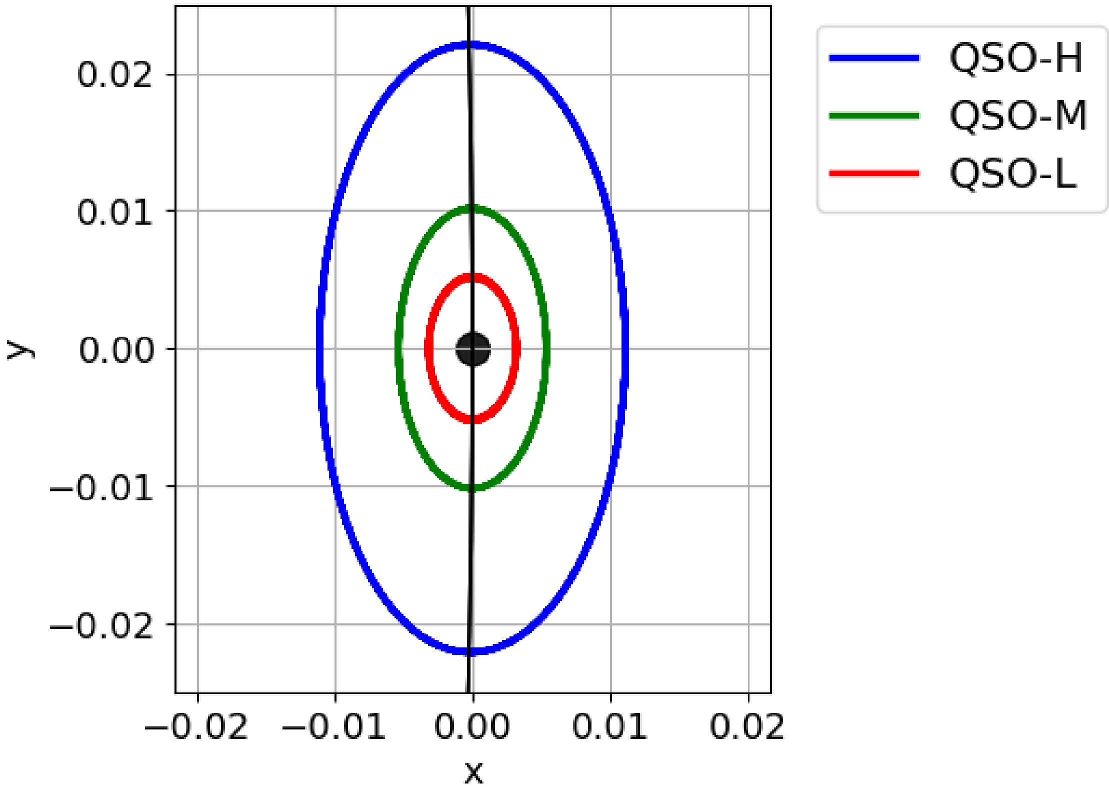

Figure 2.4: High, medium and low planar and periodic QSO's to be flown by MMX. Mars is located at (-1,0) and Phobos is at (0,0). The mean radius of Phobos is shown as a black circle.

Table 2.2: Mean orbital elements and initial conditions leading to the three baseline QSO's to be flown by MMX around Phobos. The coordinates and orbital elements not shown here are equal to zero. The exact meaning of the parameters is discussed in Chapter 3.

	QSO-H	**QSO-M**	**QSO-L**
r_{min} [km]	100	50	30
T [rev]	0.990291	0.931507	0.755556
$C_j - 3$	-0.0001234328435555	-0.0000289435706313	-0.0000101835101867
ρ_0	-0.0111081731309235	-0.0053754664413856	-0.0032050515370219
$\dot{\theta}_0$	0.0219783044464176	0.0109615884583334	0.0071360500278927
a_0	0.9998672787982409	0.9994355445926816	0.9984997713566375
e_0	0.0112423864357207	0.0059432765632975	0.0047123497825057
a_{av}	1.00000116288	1.00000292479	1.00000361087
e_{av}	0.0112001826189	0.00577479742522	0.0043246687166
R_{slow}/μ	61.0405814326	130.857949746	240.822346891

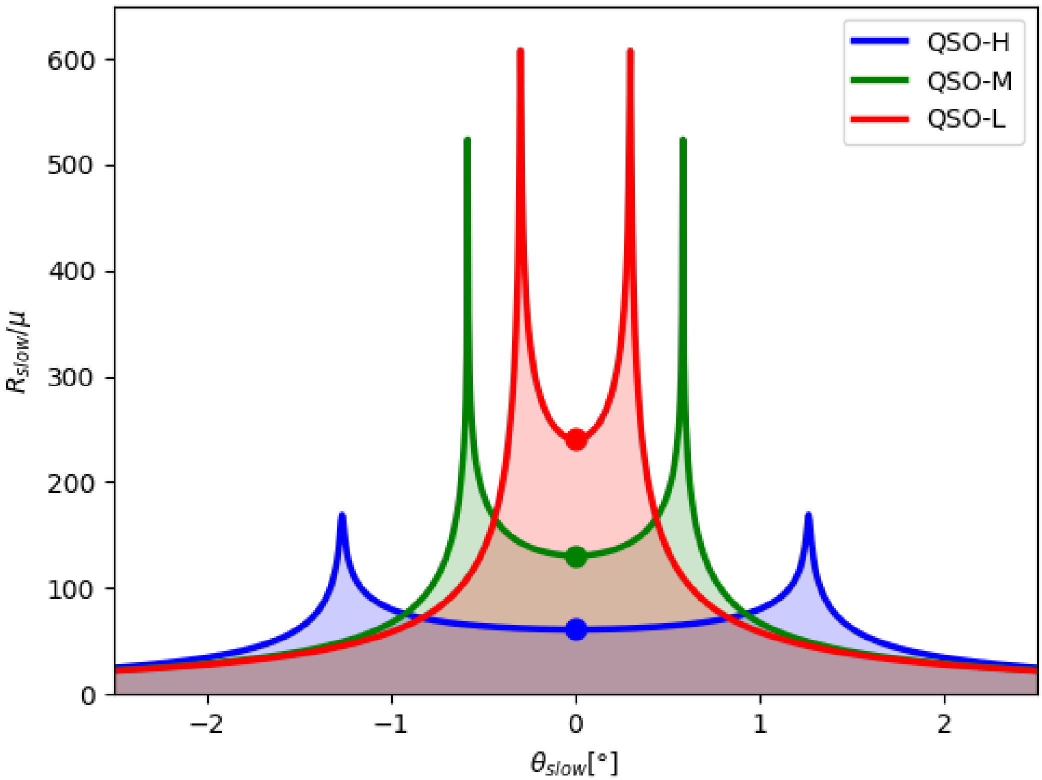

Figure 2.5: Disturbing function and location of the guiding center in the three baseline 2D QSO's of MMX. In reality, all peaks go to infinity.

3

Dynamics Model

The current chapter is focused on the models of the dynamics for the Phobos-Mars systems that will hereafter be used for orbit propagation and visualization purposes. First, an overview of the forces present in the system and the simplifications being made will be provided. Second, the commonly used Cartesian synodic coordinate system will be presented and its equations of motion and Jacobi constant will be provided. Finally, the curvilinear frame to be used for orbit propagation will be briefly introduced, presenting again equations of motion, Jacobi constant and the expression of the Jacobian.

3.1. Circular Restricted Three-Body Problem: Phobos-Mars

First introduced by Newton, the Three-Body Problem is probably the most well-known and studied dynamic problem, as some of the greatest physicists and mathematicians in history have dealt with it. The problem consists of three point masses that interact with each other through gravity and inertia. This will be the case of MMX when flying close to Phobos, with the spacecraft, Phobos and Mars. Given the tiny mass of the MMX spacecraft compared to those of Phobos and Mars, it is reasonable to neglect the effect of the spacecraft on the planet and the moon, leading to the Restricted Three-Body Problem. Furthermore, given the small eccentricity of the orbit of Phobos with respect to Mars ($e = 0.0151$), this can be neglected, which implies modeling the dynamics as a Circular Restricted Three-Body Problem (CR3BP) [34].

Nevertheless, on top of the inertial and point-mass gravitational accelerations, there are other forces acting on the bodies. The main perturbations from the CR3BP, ordered according to their relevance in the vicinity of Phobos, are [6]:

- Phobos eccentricity
- Phobos irregular gravity field
- Mars irregular gravity field
- Third body accelerations (Sun, Jupiter, Earth...)
- Solar radiation pressure

Of these five kinds of perturbations, the eccentricity and spherical harmonics of Phobos are the major perturbations on orbits in the proximity of the moon [6]. Nevertheless, the present project is intended as a preliminary study for the mission design of MMX. Given the fact that extensive computation is required, even the perturbations caused by Phobos' eccentricity and irregular gravity field will be neglected hereafter. This means that the model for the dynamics in the PPP of MMX used in the present study will be the CR3BP.

In the CR3BP model used throughout this thesis, the unit of distance is the semi-major axis of the orbit of Phobos (9377.2 km). The unit of time is the orbital period of Phobos (7.65 h). Note that both the units of distance and time in the Phobos-Mars system are substantially smaller than the ones of the Moon-Earth system. Regarding MMX, this implies an additional difficulty to the operations in terms of communication and orbit maintenance. The unit of mass in the Phobos-Mars system is the sum of the masses of Phobos and Mars. The mass parameter of Phobos (relative mass in the system) is computed as follows:

$$\mu = \frac{GM_{Phobos}}{GM_{\male} + GM_{Phobos}} = 1.661025566426 \cdot 10^{-8}$$

With this formulation, the barycenter of the system is located on the line connecting planet and moon, at a distance μ from the planet and $1-\mu$ from the moon.

3.2. CARTESIAN SYNODIC FRAME

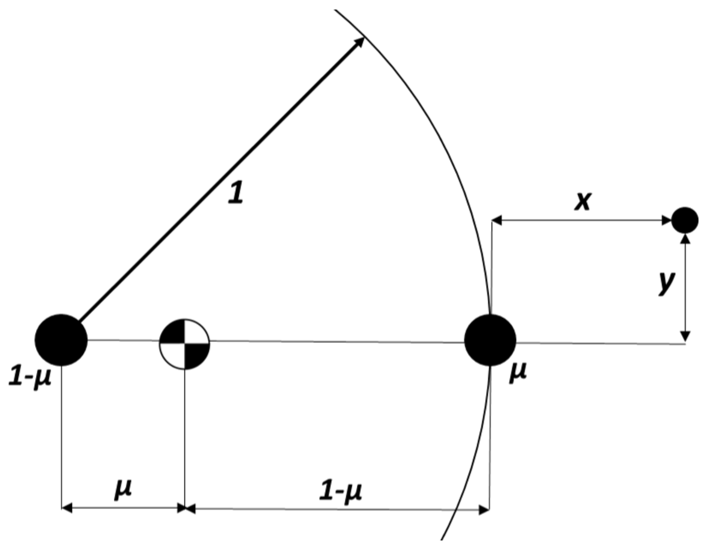

Figure 3.1: Cartesian synodic frame. Notice that the origin is located at the second primary and not at the barycenter of the system.

The Cartesian synodic frame, centered at and co-rotating with the moon, is the most commonly used system to model the CR3BP. The $x-y$ plane is the orbital plane of the moon, the z-axis points in the direction of the angular momentum on the moon and the x-axis points from the planet to the moon. This configuration is illustrated in Fig. 3.1. Although this will not be the coordinate system used to propagate the orbits in the present thesis, given its simplicity and the extensive literature on it, it will be used for validation purposes (see Appendix A). In addition, this system will be used to depict the trajectory of the spacecraft once the orbit has been integrated in the curvilinear frame.

3.2.1. EQUATIONS OF MOTION

One of the advantages of setting the origin of the coordinates at the position of the moon is the possibility to linearize the dynamics close to the secondary for some applications. The complete equations of motion in the Cartesian synodic frame for the motion of the spacecraft in the CR3BP are presented bellow [34]. Note that the right-hand sides provide the linearization of the expressions.

$$\ddot{x} - 2\dot{y} - (3-2\mu)x = -(1-\mu)\frac{1+x}{[(1+x)^2+y^2+z^2]^{3/2}} + (1-\mu)(1-2x) - \mu\frac{x}{[x^2+y^2+z^2]^{3/2}} \tag{3.1}$$

$$\ddot{y} + 2\dot{x} - \mu y = -(1-\mu)\frac{y}{[(1+x)^2+y^2+z^2]^{3/2}} + (1-\mu)y - \mu\frac{y}{[x^2+y^2+z^2]^{3/2}} \tag{3.2}$$

$$\ddot{z} + (1-\mu)z = -(1-\mu)\frac{z}{[(1+x)^2+y^2+z^2]^{3/2}} + (1-\mu)z - \mu\frac{z}{[x^2+y^2+z^2]^{3/2}} \tag{3.3}$$

3.2.2. JACOBI CONSTANT

In the CR3BP, there is a first integral of the motion which accounts for the energy level of the spacecraft. This is referred to as the Jacobi constant after its discoverer, and in the Cartesian synodic frame it has the following definition [34]:

$$C_j = -\left(\dot{x}^2+\dot{y}^2+\dot{z}^2\right) + \left(x^2+y^2\right) - 2\left(1-\mu\right)x - 2U_g - \mu = const. \tag{3.4}$$

where U_g is the gravitational potential, defined as:

$$U_g = -\frac{1-\mu}{\sqrt{(1+x)^2+y^2+z^2}} - \frac{\mu}{\sqrt{x^2+y^2+z^2}} \tag{3.5}$$

3.3. CURVILINEAR FRAME

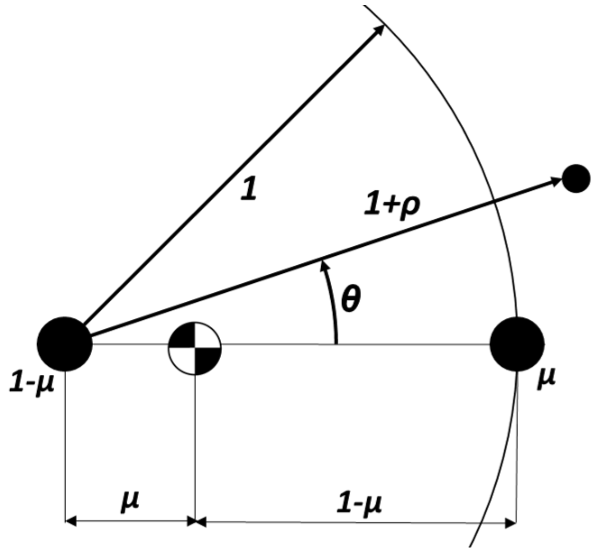

Figure 3.2: Curvilinear coordinates system.

Curvilinear coordinates are less commonly used, but in general they offer a better performance in terms of computational cost, due to their more accurate linearization, not only close to the moon but also for other kinds of co-orbital motion far from it (e.g. Horseshoe and Tadpole orbits) [32]. This is why the curvilinear frame will be the system used to numerically integrate the trajectories of the MMX spacecraft around Phobos. In the curvilinear system $1+\rho$ is the distance from the planet to the projection of the spacecraft on the orbital plane of the moon. θ is the angle formed between the moon, the planet and the projection of the spacecraft on the orbital plane of the moon. Finally, z is the out-of-plane coordinate, just as in the Cartesian frame. Fig. 3.2 illustrates the configuration of the curvilinear reference reference frame.

3.3.1. EQUATIONS OF MOTION

The linearized equations of motion for the CR3BP, re-written in curvilinear coordinates, read [33]:

$$\ddot{\rho} - 2\dot{\theta} - (3-2\mu)\rho = a_{i\rho} + a_{g1\rho} + a_{g2\rho} \tag{3.6}$$
$$\ddot{\theta} + 2\dot{\rho} = a_{i\theta} + a_{g2\theta} \tag{3.7}$$
$$\ddot{z} + (1-\mu)z = a_{g1z} + a_{g2z} \tag{3.8}$$

where the non-linear acceleration terms caused by inertia ($a_{i\rho}$, $a_{i\theta}$), main primary gravitation ($a_{g1\rho}$, a_{g1z}) and second primary gravitation ($a_{g2\rho}$, $a_{g2\theta}$, a_{g2z}) on the right-hand side of the equations are:

$$a_{i\rho} = 2\rho\dot{\theta} + (1+\rho)\dot{\theta}^2 \tag{3.9}$$
$$a_{g1\rho} = 1 - 2(1-\mu)\rho - (1-\mu)\frac{1+\rho}{[(1+\rho)^2+z^2]^{3/2}} \tag{3.10}$$
$$a_{g2\rho} = -\mu\frac{1+\rho-\cos\theta}{[(1+\rho-\cos\theta)^2+\sin^2\theta+z^2]^{3/2}} - \mu\cos\theta \tag{3.11}$$
$$a_{i\theta} = \frac{2\dot{\rho}(\rho-\dot{\theta})}{1+\rho} \tag{3.12}$$
$$a_{g2\theta} = -\mu\frac{\sin\theta}{(1+\rho)[(1+\rho-\cos\theta)^2+\sin^2\theta+z^2]^{3/2}} - \frac{\mu\sin\theta}{1+\rho} \tag{3.13}$$
$$a_{g1z} = (1-\mu)z - (1-\mu)\frac{z}{[(1+\rho)^2+z^2]^{3/2}} \tag{3.14}$$
$$a_{g2z} = -\mu\frac{z}{[(1+\rho-\cos\theta)^2+\sin^2\theta+z^2]^{3/2}} \tag{3.15}$$

3.3.2. JACOBI CONSTANT

The Jacobi constant can also be expressed in curvilinear coordinates, leading to the following formulation for the first integral:

$$C_J = -\left[\dot{\rho}^2 + (1+\rho)^2(\dot{\theta}^2-1) + \dot{z}^2\right] - 2\mu(1+\rho)\cos\theta - 2U_g + \mu = const. \tag{3.16}$$

where:

$$U_g = -\frac{1-\mu}{\sqrt{(1+\rho)^2+z^2}} - \frac{\mu}{\sqrt{(1+\rho-\cos\theta)^2+\sin^2\theta+z^2}} \tag{3.17}$$

3.3.3. JACOBIAN AND STATE TRANSITION MATRIX

For some computations regarding the stability of the orbits being simulated (e.g. the single-shooting algorithm) the Jacobian of the equations of motion is required. This can be computed from Eqs. (3.6) to (3.8) by differentiating each equation with respect to each coordinate in the system. Given the complexity of this derivation, *Maple* software was used for it, leading to Eq. (3.18).

$$\frac{\partial \mathbf{F}}{\partial \mathbf{s}} = \begin{bmatrix} Df_{1,1} & \dots & Df_{1,6} \\ \vdots & \ddots & \vdots \\ Df_{6,1} & \dots & Df_{6,6} \end{bmatrix} \tag{3.18}$$

with:

$$
\begin{aligned}
&Df_{1,1} = Df_{1,2} = Df_{1,3} = Df_{2,1} = Df_{2,2} = Df_{2,3} = Df_{3,1} = Df_{3,2} = Df_{3,3} = 0\\
&Df_{1,4} = Df_{2,5} = Df_{3,6} = 1\\
&Df_{1,5} = Df_{1,6} = Df_{2,4} = Df_{2,6} = Df_{3,4} = Df_{3,5} = 0\\
&Df_{4,1} = \left(1+\dot{\theta}\right)^2 + \left(1-\mu\right)\frac{2\left(1+\rho\right)^2 - z^2}{\left(\left(1+\rho\right)^2 + z^2\right)^{5/2}} + \mu\frac{1+3\cos^2\theta - 4\left(1+\rho\right)\cos\theta + 2\rho\left(2+\rho\right) - z^2}{\left(2\left(1+\rho\right)(1-\cos\theta) + \rho^2 + z^2\right)^{5/2}}\\
&Df_{5,1} = \frac{2\dot{\rho}\left(1+\dot{\theta}\right) - \mu\sin\theta}{\left(1+\rho\right)^2} - \mu\sin\theta\frac{5\left(1-\left(1+\rho\right)\cos\theta\right) + 8\rho + 4\rho^2 + z^2}{\left(1+\rho\right)^2\left(2\left(1+\rho\right)(1-\cos\theta) + \rho^2 + z^2\right)^{5/2}}\\
&Df_{6,1} = 3\left(1-\mu\right)\frac{\left(1+\rho\right)z}{\left(\left(1+\rho\right)^2 + z^2\right)^{5/2}} + 3\mu\frac{\left(1+\rho - cos\theta\right)z}{\left(1+\rho\right)^2\left(2\left(1+\rho\right)(1-\cos\theta) + \rho^2 + z^2\right)^{5/2}}\\
&Df_{4,2} = \mu\sin\theta\left(1 + \frac{-1 + 2\left(1+\rho\right)^2 - \left(1+\rho\right)\cos\theta - z^2}{\left(1+\rho\right)^2\left(2\left(1+\rho\right)(1-\cos\theta) + \rho^2 + z^2\right)^{5/2}}\right)\\
&Df_{5,2} = \frac{\mu\cos\theta}{1+\rho} - \mu\frac{\left(1+\rho\right)(1+\cos\theta)^2 - 2\left(1+\rho\right) + \left(\rho^2 + z^2\right)\cos\theta}{\left(1+\rho\right)\left(\left(1+\rho\right)^2\left(2\left(1+\rho\right)(1-\cos\theta) + \rho^2 + z^2\right)^{5/2}\right)}\\
&Df_{6,2} = \frac{3\mu\left(1+\rho\right)z\sin\theta}{\left(1+\rho\right)^2\left(2\left(1+\rho\right)(1-\cos\theta) + \rho^2 + z^2\right)^{5/2}}\\
&Df_{4,3} = 3\left(1-\mu\right)\frac{\left(1+\rho\right)z}{\left(\left(1+\rho\right)^2 + z^2\right)^{5/2}} + 3\mu\frac{\left(1+\rho - cos\theta\right)z}{\left(1+\rho\right)^2\left(2\left(1+\rho\right)(1-\cos\theta) + \rho^2 + z^2\right)^{5/2}}\\
&Df_{5,3} = \frac{3\mu z\sin\theta}{\left(1+\rho\right)\left(1+\rho\right)^2\left(2\left(1+\rho\right)(1-\cos\theta) + \rho^2 + z^2\right)^{5/2}}\\
&Df_{6,3} = \left(1-\mu\right)\frac{2z^2 - \left(1+\rho\right)^2}{\left(\left(1+\rho\right)^2 + z^2\right)^{5/2}} - \mu\frac{2\left(1+\rho\right)(1-\cos\theta) + \rho^2 - z^2}{\left(1+\rho\right)^2\left(2\left(1+\rho\right)(1-\cos\theta) + \rho^2 + z^2\right)^{5/2}}\\
&Df_{4,4} = Df_{4,6} = Df_{5,5} = Df_{5,6} = Df_{6,4} = Df_{6,5} = Df_{6,6} = 0\\
&Df_{4,5} = 2\left(1+\rho\right)\left(\dot{\theta}\right)\\
&Df_{5,4} = -2\frac{1+\dot{\theta}}{1+\rho}
\end{aligned}
$$

The previous analytic expression of the Jacobian in curvilinear coordinates becomes particularly useful for the computation of the so-called State Transition Matrix (STM). The STM is the result of a linearization of the motion for small deviations in the initial conditions with respect to a nominal reference trajectory. The STM relates the state of two different epochs: when multiplied by the deviation from the nominal initial conditions, the STM returns an approximation of the deviation from the nominal state at the propagated epoch. Mathematically, this is expressed as follows, Φ being the mathematical representation of the STM:

$$\Delta\mathbf{s}\left(\tau\right) = \Phi_{\left(\tau,\tau_0\right)} \cdot \Delta\mathbf{s}\left(\tau_0\right) \tag{3.19}$$

As shown, the STM is a function of the two epochs that it relates and, as such, it can be propagated using a numerical integrator. The differential equations that govern the evolution of the STM can be obtained by differentiating the equations of motion with respect to the state (**s**) and linearizing with respect to a nominal trajectory. As a result, the time evolution of the STM obeys the following relation:

$$\dot{\Phi}_{(\tau,\tau_0)} = \frac{\partial \mathbf{F}}{\partial \mathbf{s}}(\tau) \cdot \Phi_{(\tau,\tau_0)} \tag{3.20}$$

where the matrix $F(\tau)$ represents the Jacobian on the motion (Eq. (3.19)) substituted at the nominal position for the epoch τ. The initial condition from which the STM can be integrated over time is trivial, as it arises from the definition of the STM:

$$\Phi_{(\tau_0,\tau_0)} = \mathscr{I}_{6\times 6} \tag{3.21}$$

4

Co-orbital motion

In the Three-Body Problem, and in particular in the CR3BP, the condition for which the orbital periods of the third body (spacecraft) and the second primary (moon), in their respective orbits around the first primary (planet), are very close to each other, is referred to as *co-orbital motion* or *1:1 resonance*. Since the period of an orbit is determined by its semi-major axis, the added condition for co-orbital motion in the CR3BP is $a \approx 1$. There are three major kinds of co-orbits in the Three-Body Problem: TPO, HSO and QSO. An illustration of these three kinds of orbits is presented in Fig. 4.1.

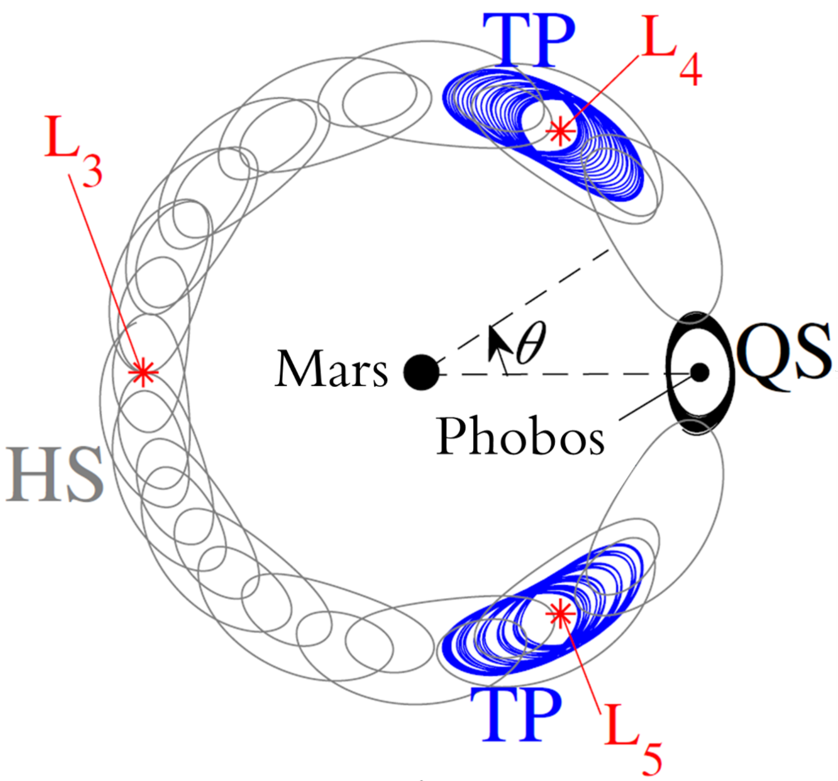

Figure 4.1: Types of co-orbital motion: Tadpole (TP), Horseshoe (HS) and Quasi-Satellite (QS) orbits [35]. The location of the Lagrange equilibrium points L_3, L_4, L_5 is depicted in red.

4.1. SLOW AND FAST DYNAMICS

One of the particularities of co-orbital motion is that the dynamics allow to be conveniently separated into two contributions, as illustrated in Fig. 4.2. Under the adiabatic hypothesis[1], the dynamics are decomposed in:

Fast: With an amplitude which depends on the differences in eccentricity and inclination, there is a *fast* oscillation of the spacecraft around a virtual center. This motion is due to the relative positioning between the spacecraft and Phobos on their respective areocentric orbits, and its characteristic time is the orbital period of the spacecraft and Phobos (very similar in theory).

Slow: The virtual center of the *fast* motion, commonly known as the guiding center of the motion, *slowly* moves in the synodic frame, triggered by the inertial and gravitational disturbance of Phobos on the orbital parameters of the spacecraft. In particular, the position of the guiding center is defined by the *slow* component of θ (θ_{slow}). The characteristic time of the *slow* component of the motion is usually at least one order of magnitude larger than that of the *fast* one. The *slow* motion is in general more insightful when it comes to understanding the effect of the gravitational and inertial perturbation that the moon exerts on the dynamics od the spacecraft.

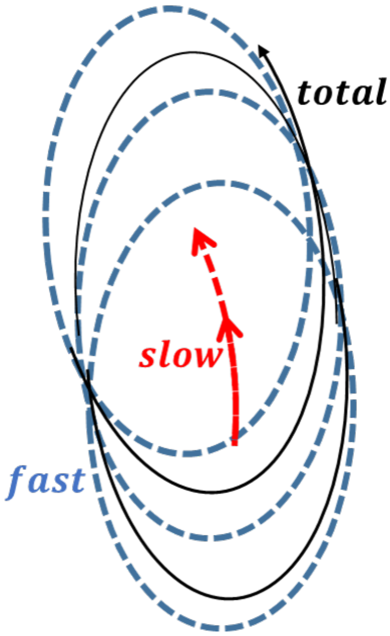

Figure 4.2: Co-orbital motion as a composition of slow and fast dynamics.

4.2. DISTURBING FUNCTION

The effect of the presence of the moon on the motion of the spacecraft has two contributions: gravitational and inertial [34]. These two forces allow to be modeled as the gradient of a potential, which is commonly referred to as the third-body disturbing function and is defined as:

$$R = \mu \left(\frac{1}{\|\mathbf{r_1} - \mathbf{r_2}\|} - \frac{\mathbf{r_1} \cdot \mathbf{r_2}}{\|\mathbf{r_2}\|^3} \right) \tag{4.1}$$

where $\mathbf{r_1}$ is the position vector going from the first primary to the third body and $\mathbf{r_2}$ is the vector from the first to the second primary. Note that the first term is the effect of the moon's gravity whereas the second one is due to inertia. When expressed in curvilinear coordinates, the disturbing function reads:

[1]The adiabatic hypothesis assumes that the fast and slow dynamics are uncoupled, and the overall motion can be perfectly described as the sum of the fast and slow contributions.

$$R = \mu\left(\frac{1}{\sqrt{\rho^2 + z^2 + 2\left(1+\rho\right)\left(1-\cos\theta\right)}} - \left(1+\rho\right)\cos\theta\right) \tag{4.2}$$

As explained in Section 4.1, when the dynamics are divided in slow and fast, the second primary's effect on the motion of the spacecraft is reflected in the slow component of the motion. Thus, the slow component of the disturbing function –hereafter slow disturbing function– plays a major role. The analytic derivation of the slow or averaged disturbing function is a subject undergoing intense study in the literature during the past decades. Some notable contributions are [36] and [37], but the most recent and general expression is provided in [33]:

$$\frac{R_{slow}}{\mu} \approx \frac{1 + f(\theta_{slow})e^2 + g(\theta_{slow})\sin^2 i}{\sqrt{a^2 - 2a\cos\theta_{slow} + 1}} - a\cos\theta_{slow}\left(1 - \frac{e^2}{2} - \frac{\sin^2 i}{4}\right) \tag{4.3}$$

where the sub-index *slow* represents the slow component of the variable in question. The f and g functions are defined as follows:

$$f(\theta_{slow}) = \frac{1}{4}\cdot\frac{\left(9 - e\cos^2\theta_{slow}\right)a^3 - 2a\left(a^2+1\right)\cos\theta_{slow}}{\left(1 - 2a\cos\theta_{slow} + a^2\right)^2} \tag{4.4}$$

$$g(\theta_{slow}) = -\frac{1}{4}\cdot\frac{a\cos\theta_{slow}}{1 - 2a\cos\theta_{slow} + a^2} \tag{4.5}$$

As exposed in [33], this expression is very accurate for small eccentricity and inclination, when the guiding center is located reasonably far from the moon ($\theta_{slow} \ll \epsilon$). Otherwise, the Taylor expansion in the eccentricity and inclination that is required to arrive at Eq. (4.3) does not converge. Therefore, Eq. (4.3) is in general valid to model the disturbing function in TPO and HSO, where the guiding center does not closely approach the position of the moon, whilst in QSO is does not perform well. Thus, for QSO a numerical averaging technique is required (see Section 4.5).

Fig. 4.3 presents the shape of the slow disturbing function depending on the location of the guiding center (θ_{slow}), which is the variable on which the function has the strongest dependence. As it is shown, the function has three maxima and three minima:

- There are two minima close to the location of the triangular equilibrium Lagrange points L_4 and L_5 ($\theta_{slow} \approx \pm 60°$). The location of these minima is slightly different from the location of the Lagrange points due to the effect of the eccentricity and inclination.
- There is a local maximum for $\theta_{slow} = \pm 180°$ (L_3), where the inertial term of the disturbing function is maximum (see Eq. (4.2)).
- There is a local minimum at the location of the moon ($\theta_{slow} = 0°$). Note that this minimum only exists when the orbit of the spacecraft has an eccentricity, so that the fast component of the motion (see Section 4.1) leads to a retrograde motion around the location of the moon. In absence of eccentricity, the spacecraft would be located at the same point as the moon, so that the slow disturbing function would have an asymptote at $\theta_{slow} = 0°$. Note that this minimum cannot be seen when looking at the expression of the full disturbing function (Eq. (4.2)) or at the approximation of the slow disturbing function provided before (Eq. (4.3)). The only way to obtain it is through the numerical average of the disturbing function for an orbit with eccentricity (see Section 4.5).
- Due to the effect of the eccentricity through the fast component of the motion, the maximum in the gravitational term of the disturbing function is not reached at the location of the moon, but at a distance which corresponds to the amplitude of the fast oscillation in θ, which is at $\theta_{slow} \approx \pm 2e$ [1]. Hence, there is a maximum in the slow disturbing function at both of these locations. Note that, in the absence of inclination, the spacecraft would pass through the location of the moon if the guiding center were located at those specific points. Thus, the two maxima would be unreachable asymptotes in the planar case.

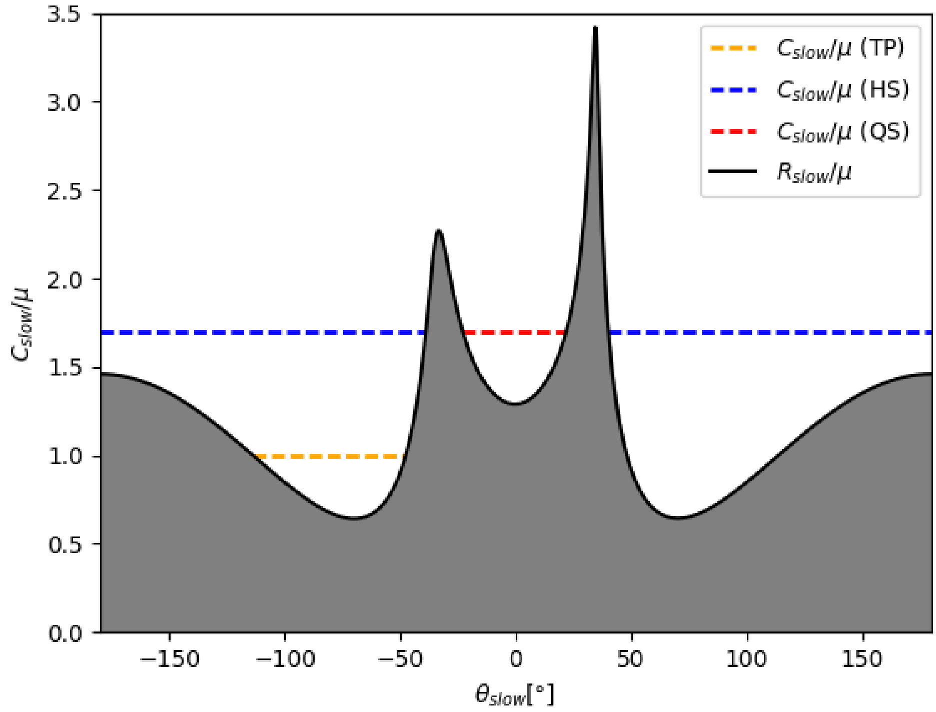

Figure 4.3: Types of co-orbital motion depending on the shape of the slow disturbing function, value of the adiabatic invariant and location of the guiding center, for $e = 0.3$ and $i = 0.1$ rad.

4.3. ADIABATIC INVARIANT

Following [33], Eq. (3.7) can be rewritten by making use of the definition of the disturbing function provided in Eq. (4.2), leading to the alternative expression:

$$\frac{d}{d\tau}\left[\frac{(1-\mu)^{2/3}}{(1+\dot{\theta})^{1/3}}\right] = \frac{\partial R}{\partial \theta} \tag{4.6}$$

Under the adiabatic assumption, Eq. (4.6) applies both to the fast and the slow dynamics independently. Hence, in the slow motion the following equation holds:

$$\frac{d}{d\tau}\left[\frac{(1-\mu)^{2/3}}{(1+\dot{\theta}_{slow})^{1/3}}\right] \approx \frac{\partial R_{slow}}{\partial \theta_{slow}} \tag{4.7}$$

According to Eq. (4.3), the slow disturbing function depends on four variables: position of the guiding center (θ_{slow}), semi-major axis (a), eccentricity (e) and inclination (i). Therefore, applying the chain rule, the time derivative of R_{slow} can be written as:

$$\frac{dR_{slow}}{d\tau} = \frac{\partial R_{slow}}{\partial \theta_{slow}}\dot{\theta}_{slow} + \frac{\partial R_{slow}}{\partial a}\dot{a} + \frac{\partial R_{slow}}{\partial e}\dot{e} + \frac{\partial R_{slow}}{\partial i}\dot{i} \tag{4.8}$$

In the case of TPO and HSO far from the moon, it is reasonable to neglect the dependence on the osculating elements (a, e, i) in Eq. (4.8), since they hardly change when the moon is far. Moreover, their influence on the slow disturbing function is subtle when θ_{slow} is large. With this assumption, Eq. (4.7) leads to a first integral of the slow motion, which is commonly referred to as the *adiabatic invariant*:

$$C_{slow} \approx \frac{1}{2}(1-\mu)\,\frac{3+\dot{\theta}_{slow}}{\sqrt[3]{1+\dot{\theta}_{slow}}}+R_{slow} \tag{4.9}$$

In addition, the velocity of the guiding center is related to the semi-major axis via the following expression [32][33]:

$$\dot{\theta}_{slow} \approx n-1=\frac{\sqrt{1-\mu}}{a^{3/2}}-1 \tag{4.10}$$

By substituting Eq. (4.10) into Eq. (4.9), the adiabatic invariant can be rewritten as:

$$C_{slow} \approx \sqrt{(1-\mu)\,a}+\frac{1-\mu}{2a}+R_{slow} \tag{4.11}$$

Eq. (4.11) can be seen as the "energy conservation" equation of the slow dynamics of the guiding center. If a constant term is added to both sides, the equation can be rewritten as:

$$C'_{slow} \approx T_{slow}+R_{slow} \tag{4.12}$$

with:

$$T_{slow}=\sqrt{(1-\mu)\,a}+\frac{1-\mu}{2a}-\sqrt{1-\mu}-\frac{1-\mu}{2} \tag{4.13}$$

Note that T_{slow} becomes zero when $a=1$ and therefore $\dot{\theta}_{slow}=0$, so the guiding center does not move. Hence, it will hereafter be referred to as the kinetic term of the adiabatic invariant. Furthermore, if the semi-major axis is assumed close to one and also the mass parameter is neglected when compared to the difference in semi-major axes ($\mu \ll a-1 \approx 0$) a multivariate Taylor expansion around $\mu \approx 1$, $a \approx 1$ provides the following expression for the kinetic term in the adiabatic invariant [38]:

$$T_{slow} \approx \frac{3}{8}(a-1)^2 \tag{4.14}$$

which indicates that the absolute value of the difference in semi-major axis is the key variable to determine the kinetic term in the adiabatic invariant. Moreover, the semi-major axis is the parameter that directly governs the velocity of the guiding center (see Eq. (4.10)), which further justifies the simile with the kinetic energy of a system.

4.4. TYPES OF CO-ORBITAL MOTION

As introduced in the beginning of the chapter, there are three major kinds of co-orbital motion: TPO, HSO and QSO. The distinction between these three kinds of orbits can be explained by looking at the shape of the slow disturbing function, the value of the adiabatic invariant and the location of the guiding center, as illustrated in Fig. 4.3. The points where the slow disturbing function crosses the value of the adiabatic invariant are boundaries to the motion of the guiding center. If the guiding center encounters one of these natural barriers, it will have lost all of its kinetic energy (see Eq. (4.12)) and will rebound back in the opposite direction. According to the location of these boundaries, the orbit can be classified as TPO, HSO or QSO. Furthermore, due to the shape of the slow disturbing function, intermediate orbits are also possible (e.g. a HS-QS orbit would be attained for $C_{slow}\mu = 2.5$ in Fig. 4.3).

The shape of the slow disturbing function depicted in Fig. 4.3 assumes that the osculating parameters of the spacecraft are constant, and only the dependence on the position of the guiding center is presented. Nevertheless, when the spacecraft approaches the position of the moon ($\theta_{slow} \ll 1$), the orbital elements vary and so does the disturbing function. If due to this change, one of the maxima of the disturbing function goes over or below the value of the adiabatic invariant, transitions between the various kinds of co-orbital motion might take place. This phenomenon is illustrated in Fig. 4.4, where the effect in increasing the eccentricity or the inclination on the slow disturbing function is highlighted. As shown, due to these changes, the guiding center might be enabled to access previously forbidden regions, leading to a transition from a HSO to a QSO (commonly referred to as *ballistic capture*) or vice versa.

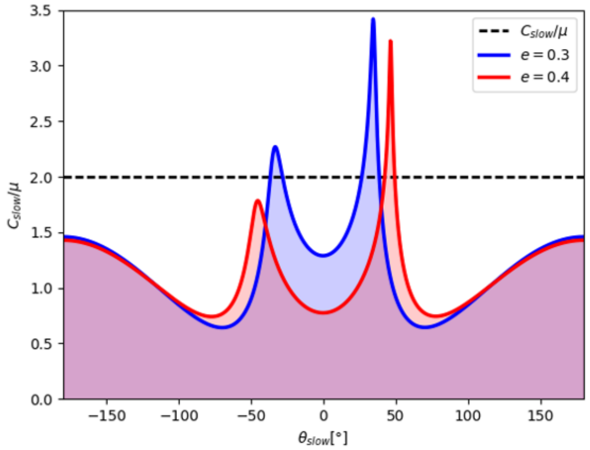

Figure 4.4: Examples of changes in the disturbing function triggering transitions between HSO and QSO. Left: increase in the eccentricity. Right: increase in the inclination.

4.5. NUMERICAL AVERAGING

As outlined over the previous sections, most of the analytic expressions for averaged variables in co-orbital motions break down when very close to the location of the moon, as is the case of QSO. Hence, a numerical approach is followed instead in order to obtain the slow component of all the variables required. The present section is devoted to the algorithm performing this numerical averaging.

As explained throughout Section 4.1, the fast component of the motion is due to the relative Keplerian motion between spacecraft and moon. As such, the characteristic time of this oscillation is equal to the orbital period of both bodies, which is nearly the same ($a \approx 1$). Hence, the independent variable with respect which to perform the numerical average could, in principle, be either the true anomaly of Phobos, or the true or mean anomaly of the spacecraft. Nevertheless, it is known that in the case of QSO, as the distance of the spacecraft to the moon decreases, so does the orbital period due to the effect of the moon's gravity [31]. Thus, it is not clear whether the period of the fast oscillation coincides with the period of the moon or that of the spacecraft itself. In order to discard both, a double average is performed with respect to the mean anomaly first and with the true anomaly of the moon later. Mathematically, this is expressed as:

$$X_{slow} = \frac{1}{(2\pi)^2} \int_{-\pi}^{\pi} \int_{-\pi}^{\pi} X \, dM d\tau \tag{4.15}$$

In order to implement Eq. (4.15) numerically in a fashion that maintains the shape of the array from input to output, for each epoch, first the closest epochs for which τ or M is phased in $\pm\pi$ are identified. After that, a simple numerical average is performed. Mathematically, this is equivalent to Eq. (4.16), where τ can also be substituted by M.

$$X_{slow}(\tau) \approx \frac{1}{N_M \cdot N_\tau} \sum_{M(\tau)-\pi}^{M(\tau)+\pi} \sum_{\tau-\pi}^{\tau+\pi} X(\tau) \tag{4.16}$$

where N_M is the number of samples taken in the average in M, and N_τ is the number of samples taken when averaging in τ.

In order to avoid offsets at the initial and final epochs, the propagation is slightly extended in both time directions. After the numerical average is performed, the results are trimmed to their original propagation time. This approach has no effects on the results, other than increasing the accuracy of the averaging technique at the beginning and at the end of the propagation time.

AVERAGE OF DISTURBING FUNCTION

In order to compute the complete profile of the slow disturbing function, it is necessary to eliminate the dependence on the position of the guiding center. In order to do so, first, the position of the guiding center (θ_{slow}) is computed through the algorithm presented above. Second, the coordinate θ is arbitrarily altered by subtracting its slow component and adding an arbitrary new one ($\hat{\theta}_{slow}$). This $\hat{\theta}_{slow}$ will range from $-180°$ to $180°$, covering all possible positions of the guiding center. Then, with the updated value of θ, the full (slow and fast together) disturbing function is computed through Eq. (4.2). The result is the value that the full disturbing function would have if the guiding center was located at $\hat{\theta}_{slow}$ instead of θ_{slow}. Mathematically, this is expressed as:

$$\theta_{new}(\tau) = \theta(\tau) - \theta_{slow}(\tau) + \hat{\theta}_{slow} \tag{4.17}$$

$$R(\tau)|_{\hat{\theta}_{slow}} = R(\theta_{new}(\tau)) \tag{4.18}$$

With that, the complete profile of the full disturbing function is computed at all epochs. Using that profile as input for the averaging algorithm exposed above, the slow disturbing function can be retrieved for each position in time and for every location of the guiding center $(\tau, \hat{\theta}_{slow})$.

5

PRELIMINARY 3D QSO STUDY

Periodic QSO's in the planar case are wellknown and there is extensive literature and analytic work on their dynamics and stability [39][27]. Besides, the period of these orbits (i.e. the time that the state takes to repeat itself) is relatively short, very close to the orbital period of the moon, which facilitates orbit determination and maintenance. This is why, for most of the three years of close observation of Phobos during the PPP of MMX, the spacecraft will fly the three orbits exposed in Section 2.4.2.

Nevertheless, a more complete physical and gravitational characterization of Phobos, which is one of the mission goals of MMX, requires the observation of high latitudes of the moon. Furthermore, the accurate characterization of the gravitational field of Phobos will improve the navigation model of the spacecraft, enhancing safety when decreasing the altitude to move from an outer QSO to an inner one. Since this is not achievable from an equatorial orbit such as QSO-H, QSO-M and QSO-L, there is a need to find three-dimensional periodic orbits that are stable and maintainable enough to be used by MMX. These orbits shall be able to access high latitudes of Phobos from a close but safe distance to the surface, ideally similar to the altitudes encountered in the baseline orbits presented in Section 2.4.2. An example of a generic (non-periodic) three-dimensional QSO is provided in Figs. 5.1 and 5.2. As shown, unlike in the 2-dimensional case, a range of latitudes over the surface of Phobos is covered by the ground track of this trajectory, rather than just the equator.

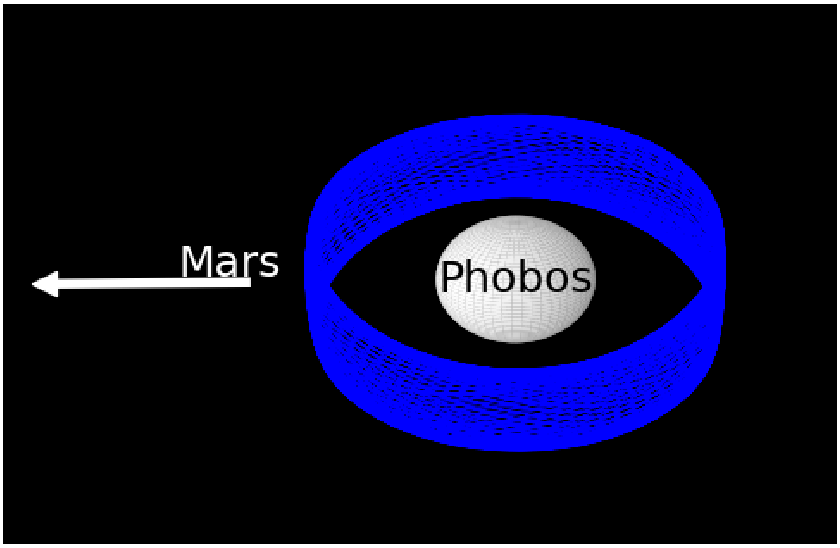

Figure 5.1: Three-dimensional trajectory of a generic out-of-plane QSO.

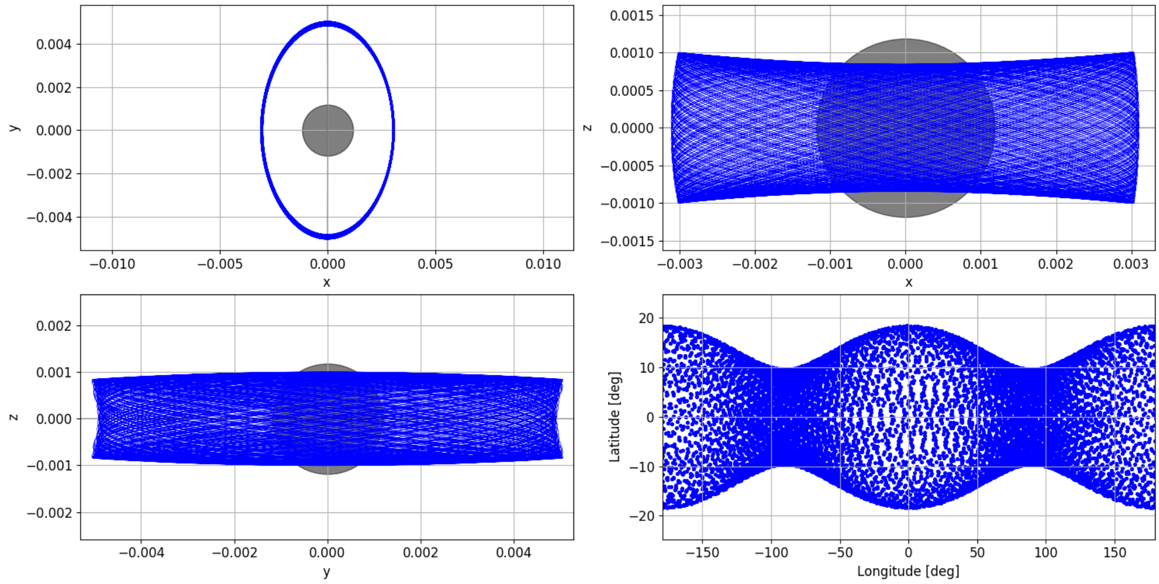

Figure 5.2: Trajectory projection on the x-y plane (top-left), x-z plane (top-right) and y-z planes (bottom-left) of a generic out-of-plane QSO. The ground track of the trajectory over the surface of Phobos is shown in the bottom-right figure. The simulation is for 100 revolutions.

5.1. TIME-TO-ESCAPE MAPS

When a non-periodic QSO around Phobos is propagated using the dynamical model described in Chapter 3, the outcome can be classified according to the following criterion [25]:

Impact: At some point along the propagation time, the position of the spacecraft lays within the surface of Phobos (modeled as a sphere with approximately the same volume as Phobos).

Escape: At some point along the propagation time, the spacecraft escapes from the QSO regime around Phobos, moving far from the vicinity of the moon.

Stable: At the end of the propagation time, the spacecraft has not escaped nor impacted with the surface of Phobos.

Only orbits that are classified as *stable* are desirable for MMX to fly around Phobos. However, this finite classification strongly depends on the propagation time (i.e. the longer the propagation time, the greater the chances of escaping or impacting with the surface). Hence, in order to identify regions in the design space where it is likely to find a stable and periodic QSO around Phobos, the time that it takes for the spacecraft to either escape or impact with Phobos is mapped. This kind of map will hereafter be referred to as *time-to-escape* map.

Note that the term *stable* used here does not respond to the concept of stability in a mathematical sense (i.e. small perturbations from the initial conditions are not increased exponentially). Here, the initial conditions are fixed for each position in the time-to-escape map and never perturbed.

5.1.1. IMPLEMENTATION

Starting from the initial conditions leading to each of the three nominal planar QSO's of MMX (see Tab. 2.2), two of the coordinates are modified in a grid search (ρ, z). In order to maintain the value of the Jacobi constant, the initial component of the velocity $\dot{\theta}$ is recomputed through the following expression, derived from Eq. (3.16):

$$\dot{\theta} = \sqrt{1 - \frac{C_j - \frac{2(1-\mu)}{\sqrt{(1+\rho)^2 + z^2}} - \frac{2\mu}{\sqrt{\rho^2 + z^2}} + 2\mu(1+\rho) - \mu}{(1+\rho)^2}} - 1 \tag{5.1}$$

where it was already taken into account that $\theta = \dot{\rho} = \dot{z} = 0$. With each of these initial conditions, the orbit is propagated with the equations of motion presented in Eqs. (3.6), (3.7) and (3.8), and a Runge-Kutta 4(5) numerical scheme with absolute and relative tolerances of 10^{-12}.

Along the propagation, two event functions are computed. When any of these functions changes sign, the propagation is terminated. The exact epoch when the function becomes zero is computed through a bisection algorithm. These two functions correspond to the escape and impact conditions, and they are designed as follows:

$$f_{imp} = (1 + \rho - \cos\theta)^2 + \sin^2\theta + z^2 - R_{mean}^2 \tag{5.2}$$

$$f_{esc} = |\theta_{slow}| - (1+\xi) \cdot 2\,e \tag{5.3}$$

The first function becomes zero at the moment when the spacecraft's position is over the sphere with the mean radius of Phobos. The second function ideally becomes zero when the guiding center is located just over one of the peaks of the disturbing function (see Fig. 4.3), thus, when the trajectory transitions from the QSO regime to a HSO, TPO or passing[1] orbit. The parameter ξ is a design parameter (set at $\xi = 0.5$) that accounts for the error in predicting the position of the extrema of the disturbing function. It is given a positive value in order to avoid mistaking a *stable* trajectory by an *escaping* one. The opposite error is however admissible, since in an escaping trajectory the guiding center will move far from the secondary, so in a later epoch the escape condition will be satisfied.

5.1.2. RESULTS

The resulting time-to-escape maps for the energy levels of the MMX nominal orbits QSO-H, QSO-M and QSO-L (see Chapter 2) are plot together in Fig. 5.3. As shown, the color scale represents the time that it takes for the spacecraft to escape or impact with the surface, in Phobos orbital periods (7.65 h). The maximum propagation time was, as shown, 400 periods, which implies that the regions exposed in white are *stable* for this time or longer. It is also important to highlight that Fig. 5.3 shows three maps with each a different value of the Jacobi constant. They are presented together, as well as the location and size of Phobos, for scale and position comparison. For each of the three maps, at least two separated regions of stability can be distinguished:

Stability continent: Adjacent to the bottom of the map (zero-inclination border) there is a moon-shaped region of stability which is in general the largest stability area in the map. The nominal MMX QSO's presented in Chapter 2 are contained in this region. However, the maximum accessible latitudes on the surface of Phobos are relatively low when compared with the stability islands. An example of an orbit belonging to the stability continent would be the one located at $(-0.01, 0.004)$ on the QSO-H time-to-escape map (see Figs. 5.3 and 5.6).

Stability island(s): Separated from the stability continent, there are generally one or more stability regions which allow access to higher latitudes over the surface of Phobos. The relative size of this region is in general smaller than that of the continent, however it becomes bigger as the value of the Jacobi constant increases (i.e. the orbits are closer to the moon). An example of a stability island QSO would be the one located at $(-0.0028, 0.0015)$ the the QSO-L time-to-escape map (see Figs. 5.3 and 5.8).

[1] A passing orbit is an orbit whose level of the adiabatic invariant is higher than any of the maxima of the disturbing function. Thus, the guiding center moves in one direction without ever rebounding, passing through the location of the second primary.

The existence of the ***escape gap*** between the stability continent and island(s) is currently a mystery, and its explanation is also one of the goals of the present work.

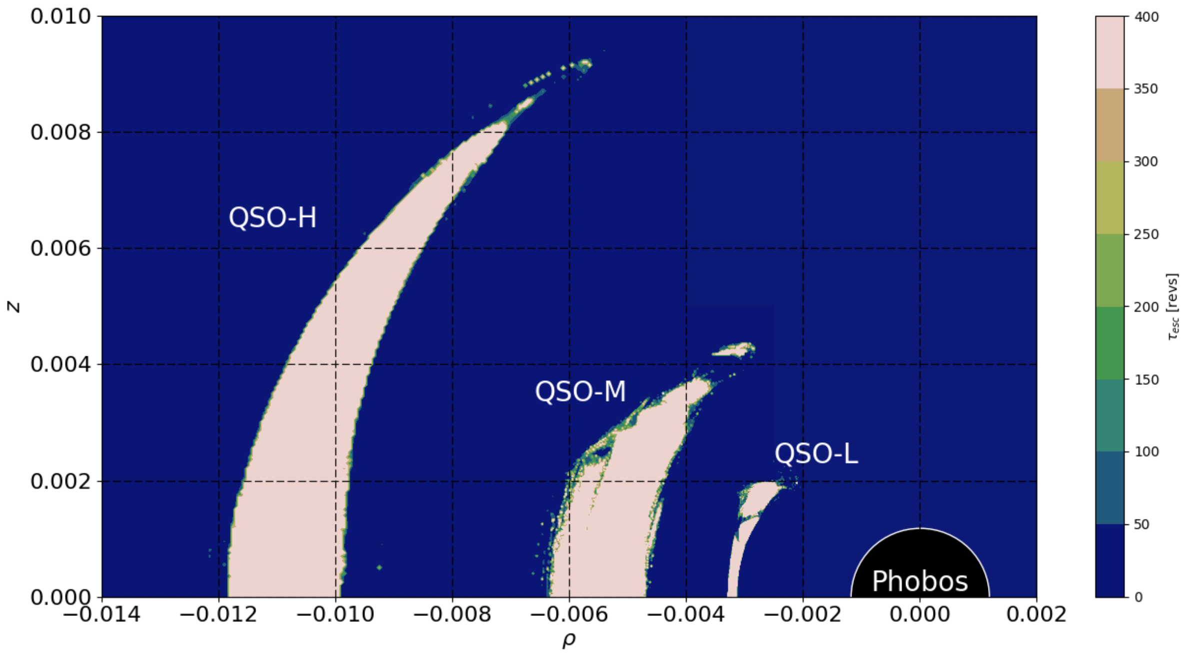

Figure 5.3: Time to escape maps computed from each of the three nominal planar QSO's of MMX. Phobos location and mean sphere are drawn for comparison.

Note that the time-to-escape maps are symmetric with respect to the ρ axis. This is the reason why negative values of z are not included. The overall semi-lunar form of the maps is due to the conservation of the Jacobi constant imposed when computing the maps. This is why the maps have a similar shape to the zero-velocity curves around Phobos.

5.2. BIFURCATION ANALYSIS

The most common approach to periodicity and stability analyses in the Three-Body Problem is through the study of eigenvalues of the monodromy matrix (i.e. the STM when propagated over time). Given their definition, these eigenvalues determine the stability of the reference trajectory against perturbations in the initial state. Eigenvalues whose real part is positive imply that deviations along the respective eigenvector are propagated exponentially, whereas negative eigenvalues show that perturbations in such direction tend to be mitigated.

Given the Hamiltonian nature of the dynamics, eigenvalues in the CR3BP show up in reciprocal pairs $(\lambda, 1/\lambda)$ and one of the eigenvalues is always trivial $(\lambda = 1)$ [40]. This implies that there are only two uncoupled eigenvalues in the problem: one corresponding to the motion in the plane and one governing the out-of-plane dynamics. Taking these additional considerations into account, the two stability indices of the motion are defined as shown in Eq. (5.4), where the sub-index i applies to both the horizontal (h) and vertical (v) dynamics.

$$b_i = \lambda_i + 1/\lambda_i \tag{5.4}$$

Linear stability is thus defined when b_i is real and $-2 < b_i < 2$. Following [40], when one of the stability indices reaches the critical value $b_i = \pm 2$, families of three-dimensional periodic QSO's may bifurcate from the two-dimensional branch depicted in Fig. 2.3. This is only satisfied when the following condition is met:

$$\lambda = \cos 2\pi \frac{d}{n} + j \sin 2\pi \frac{d}{n} \tag{5.5}$$

which is equivalent to:

$$b = 2\cos 2\pi \frac{d}{n} \tag{5.6}$$

where the parameters d and n are both integers representing the number of revolutions covered along the horizontal and the out-of-plane axes respectively. The letter j represents the imaginary unit.

According to [40], the orbits in the 2D branch shown in Fig. 2.3 that meet Eq. (5.5) shall be referred to as *d:n-resonant* orbits, leading to the bifurcation of their respective *d:n-resonant* families. Starting from the *d:n-resonant* orbits identified through this analysis of the monodromy matrix, a continuation technique can be triggered by slightly modifying the Jacobi constant and using a shooting algorithm. Following this procedure, complete *d:n-resonant* families can be retrieved.

5.2.1. RESULTS

Following the procedure exposed in [40] and summarized above, several three-dimensional periodic branches can be identified bifurcating from the planar periodic QSO regime. Fig. 5.4 presents the periodic QSO families that were identified following this procedure, for a parametrization in ρ, z and C_j at each crossing with the $\theta = 0$ plane. Families under the name $B_{d:n}$ are found by setting the initial conditions within the $\theta = 0$ plane and for $z = 0$, whereas $C_{d:n}$ families are found for $\dot{z} = 0$.

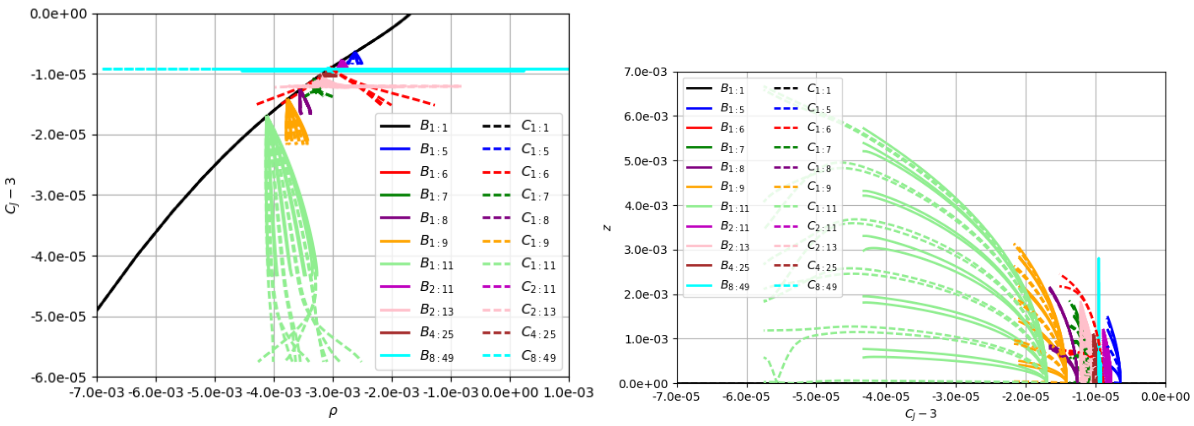

Figure 5.4: Families of three-dimensional periodic QSO found through bifurcation analysis. Each of the branches shows the coordinates ρ, z for all crossings the orbit has with the $\theta = 0$ plane, as well as the value of the Jacobi constant of the orbit.

As shown in Fig. 5.4, all branches are propagated by gradually decreasing the value of the Jacobi constant (C_j). By contrast, the evolution of values of ρ and z required for periodicity is far more unpredictable. As illustrated, each of the $B_{d:n}$ and $C_{d:n}$ families lead to $d \cdot n$ branches originated at the same point, since those are the times that the periodic orbit in question crosses the $\theta = 0$ plane before repeating itself. Note that the end of the branches depicted in Fig. 5.4 is reached when the algorithm fails to converge anymore, however the branches might continue longer. Nevertheless, because of the sudden turns observed in the branches (e.g. the sudden turns in z for the $C_{1:11}$ branches), performing an extrapolation is not reliable. This is one of the limitations of the bifurcation technique to compute periodic orbits, which is also one of the reasons why no periodic orbits were found on the stability islands using this method (see Section 5.2.2).

Regarding the stability of the QSO families, it was found to change from branch to branch, and even switch along each family. Fig. 5.5 illustrates this behavior, where dots with colors blue and red have been superimposed upon the branches depicted in Fig. 5.4, to differentiate between stable and unstable orbits respectively.

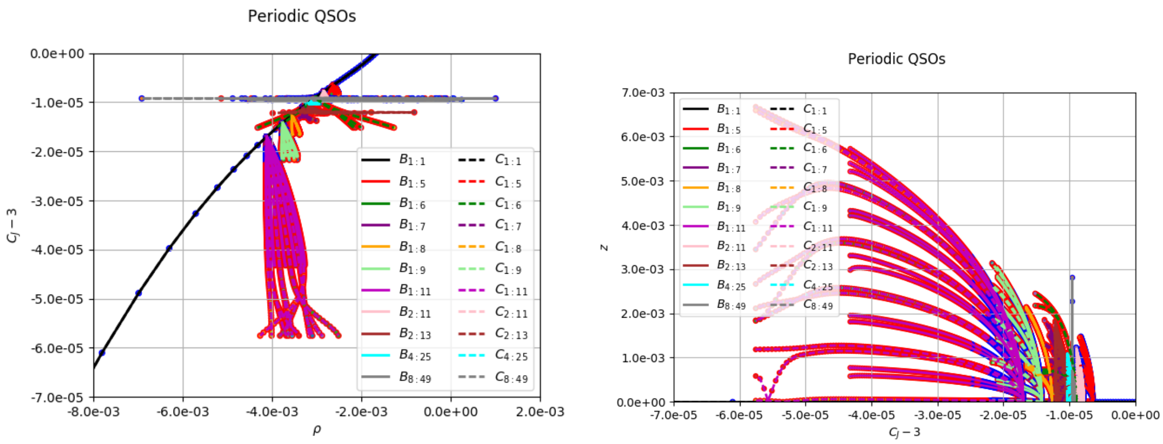

Figure 5.5: Stability of the families of three-dimensional periodic QSO's found through bifurcation analysis, superimposed upon the families identified in Fig. 5.4. Red dots represent unstable orbits (maximum real eigenvalue larger than unit) whereas blue dots represent stable orbits (maximum eigenvalue below one).

5.2.2. CORRELATION WITH TIME-TO-ESCAPE MAPS

With the use of an interpolation algorithm, for each value of the Jacobi constant it is possible to identify and locate the initial conditions leading to a periodic orbit belonging to the branches exposed in Fig. 5.4. In the same fashion, the maximum eigenvalue of the orbit can also be interpolated, providing an approximation for the stability of the orbit. With the help of these tools, three-dimensional periodic orbits can be found on the time-to-escape maps provided in Section 5.1.

Figs. 5.6, 5.7 and 5.8 show the position and stability of the periodic orbits intersecting with the time-to-escape maps at the energy levels of the three MMX nominal QSO's, belonging to the bifurcated families shown in Figs. 5.4 and 5.5. Note that only branches for which $\theta = \dot{\rho} = \dot{z} = 0$ are considered, since this is the condition used to draw the time-to-escape maps. This automatically discards orbits from the families $B_{d:n}$.

In the case of the time-to-escape map with the lowest energy level, the one referring to QSO-H (Fig. 5.6), no intersection was found with any of the periodic bifurcated branches presented in Fig. 5.4. Furthermore, note that the value of the Jacobi constant of this map lays outside of the limits of Fig. 5.4. This could be one of the reasons for the relative absence of texture in the time-to-escape map, when compared to the ones referring to QSO-M and QSO-L. The 2-dimensional periodic QSO that is seed of the stability continent is located at roughly the center of the base of the continent.

Fig. 5.7 shows the time-to-escape map and intersecting bifurcated periodic branches for the energy level of QSO-M. As shown, only the family $C_{1:11}$ intersects with this level of the Jacobi constant. The intersecting periodic orbit has an eigenvalue larger than 6, way beyond unit, which indicates that the orbit is highly unstable. This fact, together with the location of the periodic orbit (just at the tip of the continental stability region), proves the high correlation between the presence of periodic orbits and the shape of the time-to-escape maps. In this case, one could speculate that the existence of the escape gap between the island and the continent arises from small deviations from the highly unstable $C_{1:11}$ periodic orbits, which lead to escaping trajectories. Regarding the 2-dimensional periodic QSO, in this case it is slightly shifted to the right side of the continental base.

Finally, Fig. 5.8, the time-to-escape map belonging to the energy level of QSO-L, exhibits the highest number of intersecting periodic branches. In this case, there are two quite stable orbits located within the stability continent ($C_{2:13}$ and $C_{4:25}$) which explains why the region around them is very stable. On the other hand, the highly unstable $C_{1:6}$ branch intersects the time-to-escape map through the left border of the escape gap, which separates island and continent. Again, this suggests that there is a correlation between the presence of periodic unstable orbits and the existence of an escape gap.

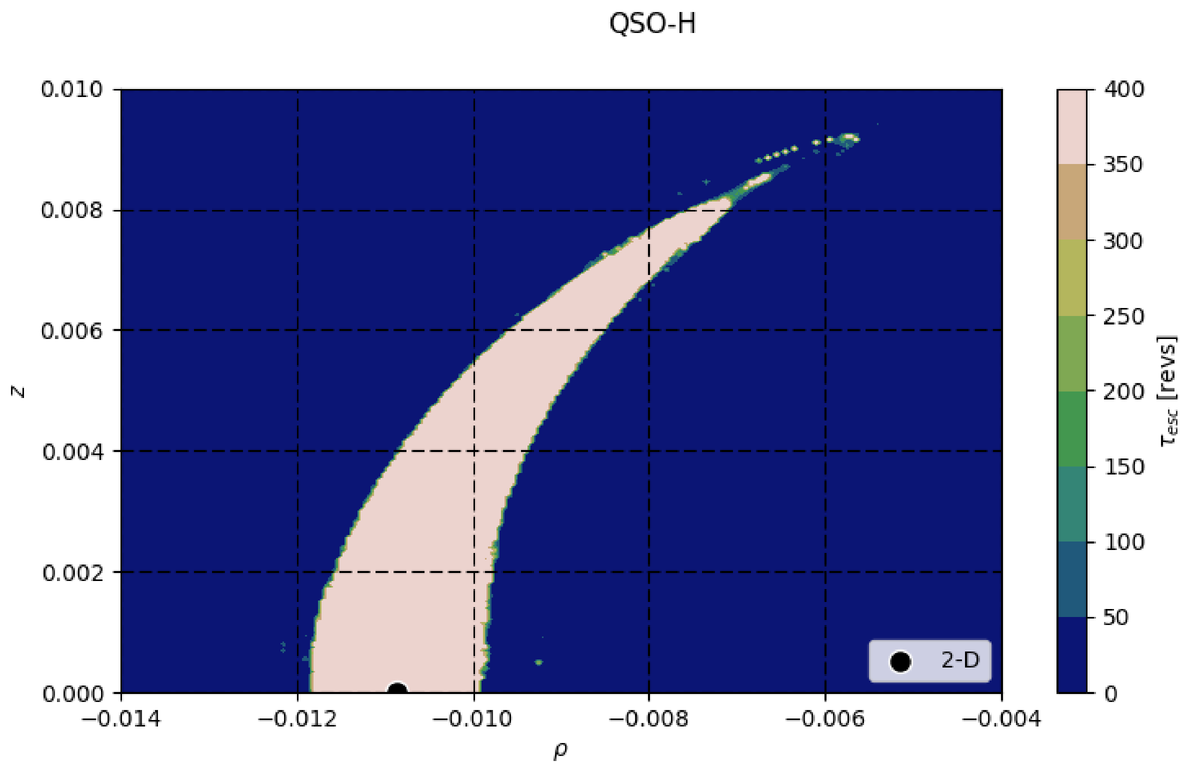

Figure 5.6: 3D periodic orbits found on the time-to-escape map for the energy level of QSO-H ($C_j = 3 - 0.0001234328435555$), via bifurcation analysis. Note that no 3D orbit was found.

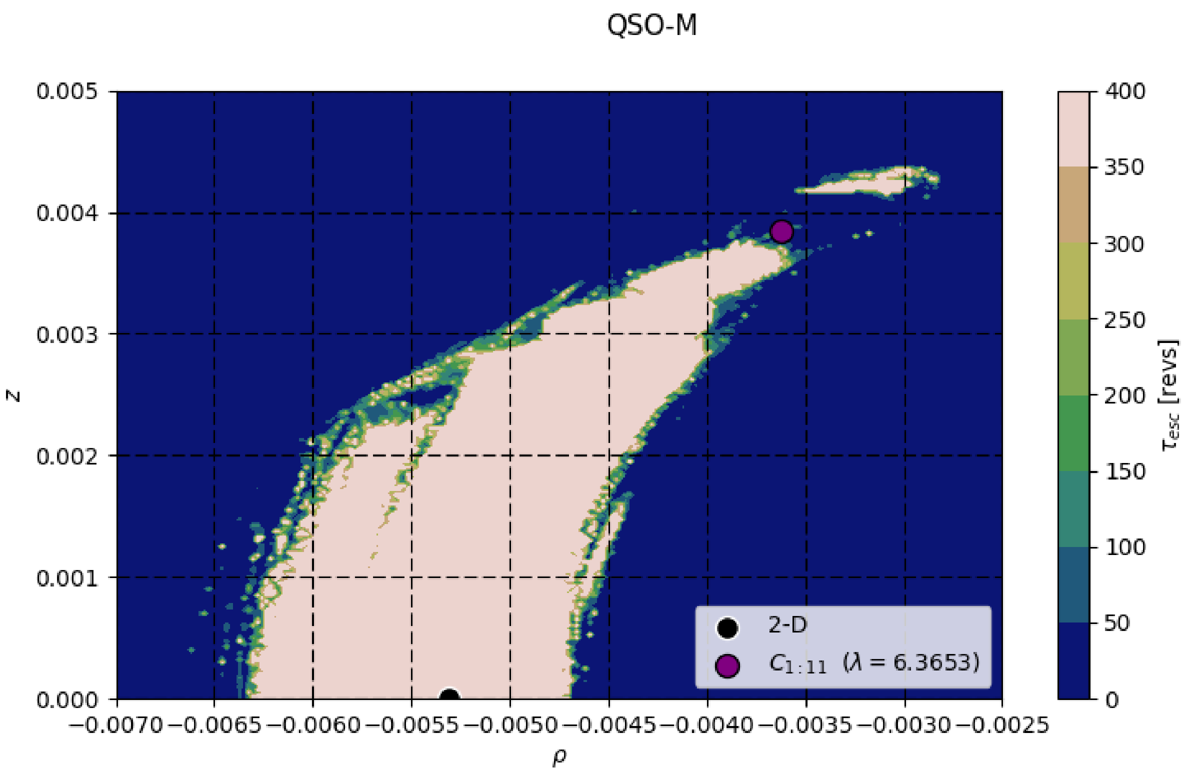

Figure 5.7: 3D periodic orbits found on the time-to-escape map for the energy level of QSO-M ($C_j = 3 - 0.0000289435706313$), via bifurcation analysis.

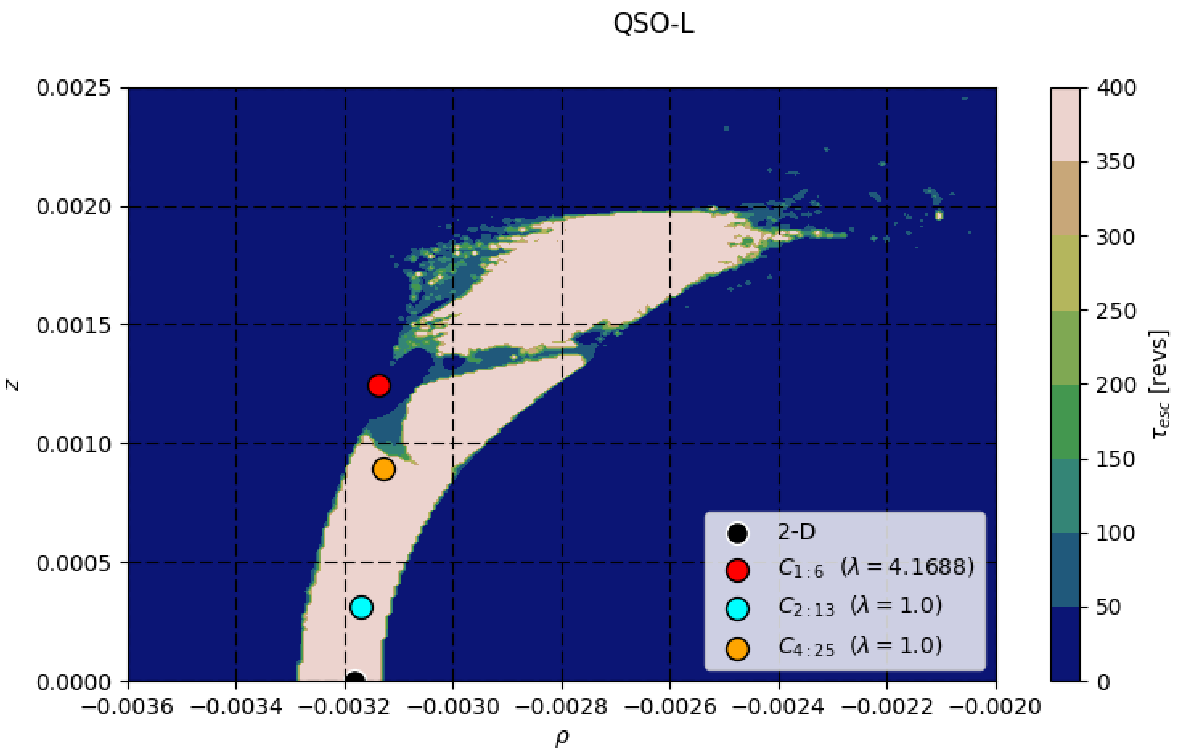

Figure 5.8: 3D periodic orbits found on the time-to-escape map for the energy level of QSO-L ($C_j = 3 - 0.0000101835101867$), via bifurcation analysis.

6

Co-orbital analysis of 3D QSO

In order to provide additional insights about the dynamics for each of the stable/escape regions identified in Chapter 5 (continent, gap and islands), several orbits belonging to those locations and for each of the three target energy levels (QSO-H, QSO-M and QSO-L) were propagated and analyzed in terms of co-orbital motion. This was done by reconstructing the evolution of the shape of the slow disturbing function, R_{slow}, as well as the motion of the guiding center, θ_{slow}. In addition, in order to qualitatively understand potential changes in the slow disturbing function, the slow component of some orbital elements (a_{slow}, e_{slow}, i_{slow}) was also analyzed.

6.1. High QSO

The largest of the planar QSO's to be flown by MMX around Phobos, QSO-H, is located at a minimum distance of 100 km from the center of the moon. The value of the Jacobi constant, as pointed out in Chapter 2, is $C_j = 3 - 0.00012343284356$. Being located relatively far from Phobos, the gravitational potential of the moon is in this case very small when compared to that of Mars, and the slow and fast components of the motion (see Chapter 4) are not coupled in excess. This is translated in a smooth shape of the time-to-escape map, where the continental region is dominant and there is only a small number of very tiny islands, as shown in Fig. 5.6. In the following sections these regions will be examined separately in order to draw overall conclusions and connections between the escape conditions and the co-orbital parameters for this energy level.

6.1.1. Stability continent

In order to grasp the co-orbital dynamics within the stability continent of QSO-H, one arbitrary orbit was picked for analysis. Note that several other analysis were conducted for other locations within the stability continent. The one exposed below was selected among those for being representative of the dynamics in the continental region.

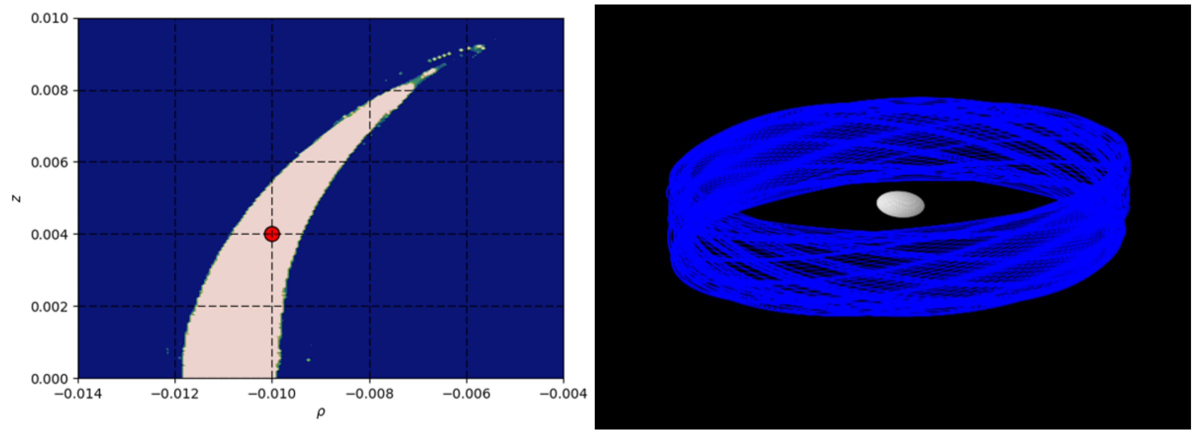

Figure 6.1: Initial conditions and trajectory of a stable QSO from the continent of the QSO-H time-to-escape map.

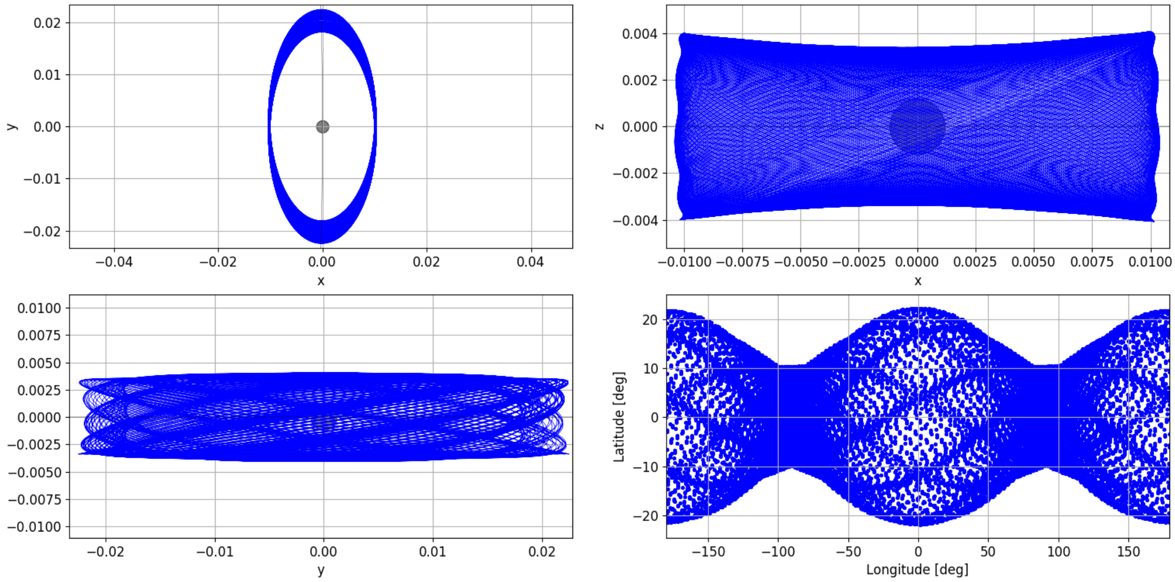

Figure 6.2: Projections of the trajectory of a stable QSO from the continent of the QSO-H time-to-escape map.

Fig. 6.1 shows the location of the orbit within the stability continent of the QSO-H time-to-escape map ($\rho = -0.01$, $z = 0.004$). At the right side of Fig. 6.1, the three-dimensional trajectory is also shown, whereas the projections of the trajectory on the planes and over the surface of Phobos are presented in Fig. 6.2. As shown, the orbit is non-periodic, since the trajectory does not repeat itself. Nevertheless, the trajectory is at all times bounded by a three-dimensional surface, which prevents it to escape. Furthermore, when looking at the three-dimensional trajectory, certain pattern can be recognized, indicating that the path is very close to repeating itself in some occasions. This might be a symptom of a periodic orbit located nearby..

When the orbit is analyzed in terms of co-orbital motion, the evolution of the slow disturbing function shall be analyzed together with the motion of the guiding center (see Chapter 4). This implies adding an extra dimension to the plots shown in that chapter, which is achieved by adding a color scale or using a 3D plot. To facilitate the interpretation of the results, both kinds of plot are combined in Fig. 6.3. Also, the expected location of the peaks of the function (twice the eccentricity at both sides from the position of Phobos) is highlighted in the picture. As illustrated in the figure, even though there is an oscillation in the maxima of the disturbing function with a period of roughly 70 revolutions, the value of the peaks is always significantly larger than the one seen by the guiding center. Moreover, the shape of the slow disturbing function close to the center hardly changes at all, resulting in a static constraint to the motion of the guiding center. As a result, the guiding center oscillates between roughly $-0.11° < \theta_{slow} < 0.11°$, with a period of about 14 Phobos

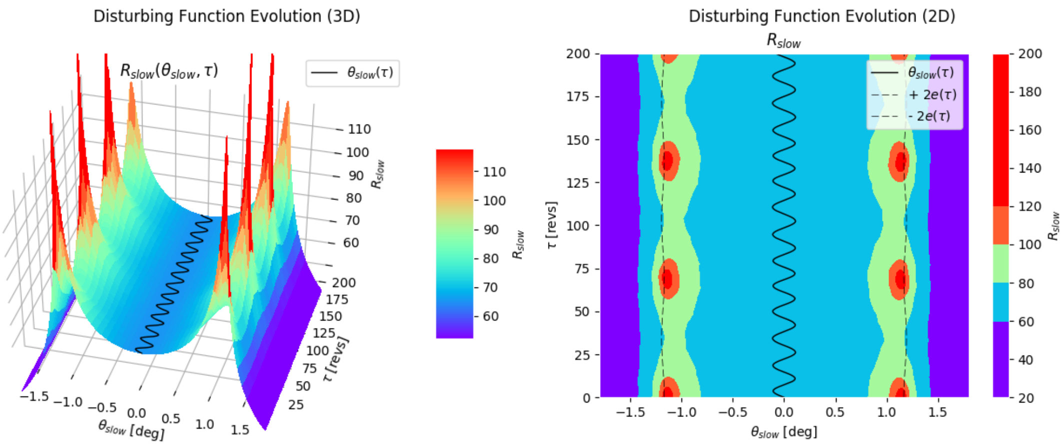

Figure 6.3: Motion of the guiding center and evolution of the disturbing function, for a stable QSO from the continent of the QSO-H time-to-escape map.

revolutions. Fig 6.4 shows a detail of the evolution of the value of the peaks in the disturbing function as a function of the location of the guiding center, as well as the value seen by the guiding center itself. Note the difference in scales between the value of the maxima and the disturbing function seen by the guiding center.

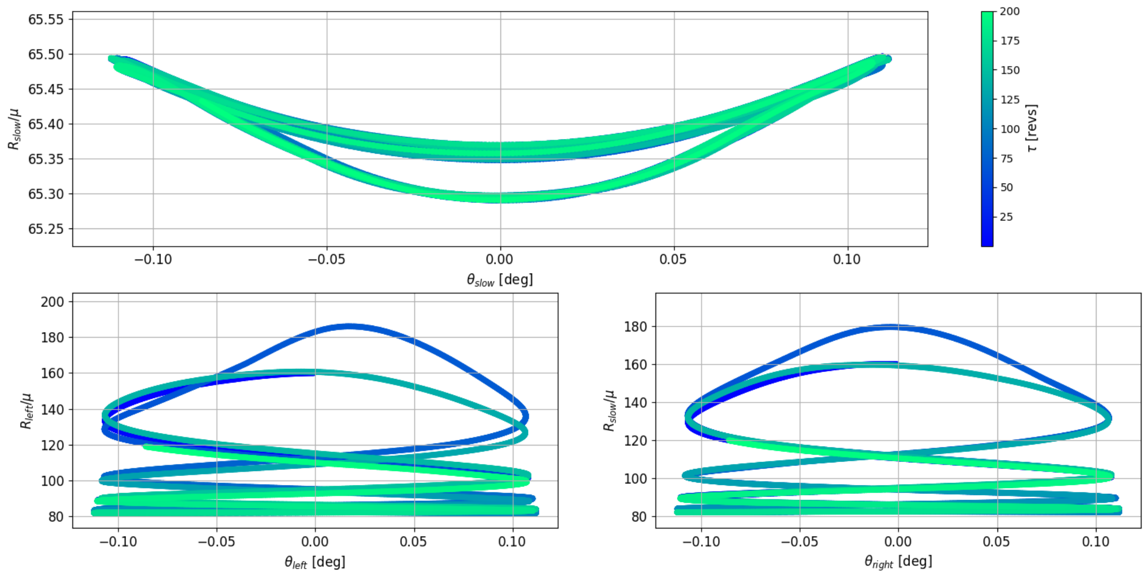

Figure 6.4: Value of the disturbing function seen by the guiding center (top) and value of the left and right maxima (bottom), as a function of the location of the guiding center in time.

Finally, in order to understand what is behind the evolution in the shape of the slow disturbing function, the slow evolution of the orbital parameters is presented in Fig. 6.5. On the one hand, the semi-major axis oscillates with the same frequency as the guiding center. This is actually expected, since the semi-major axis is known to be responsible of the velocity of the guiding center (see Eq. (4.10)). On the other hand, the eccentricity and inclination evolve cyclically with the same period as the peaks of the disturbing function, following also the Kozai mechanism [41]. These therefore seem to be the major responsible parameters that govern the shape of the disturbing function, at least in the continental region. When the eccentricity is small, the inclination is high (compensating the Tisserand parameter [42]) and the peaks of the disturbing function are high. By contrast, high eccentricity together with small inclination results in a small value of the peaks in this case.

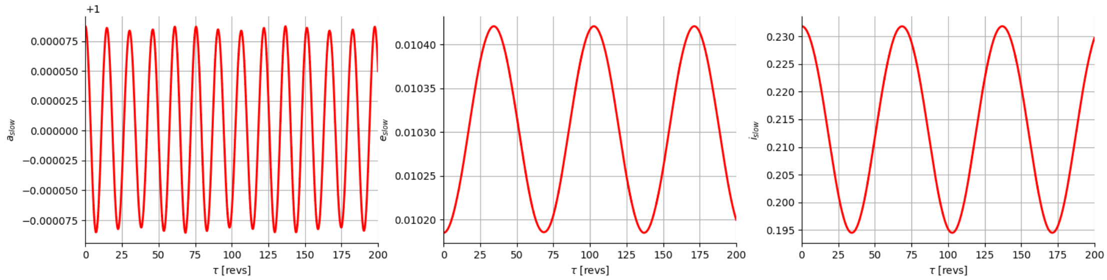

Figure 6.5: Slow evolution of the orbital parameters of a stable QSO from the continent of the QSO-H time-to-escape map.

6.1.2. ESCAPE GAP

The next step in analyzing the co-orbital dynamics along the different regions within the time-to-escape map of QSO-H, is focusing on the gap between the stability continent and the major stability island. For this, an orbit located on the position highlighted in Fig. 6.6 ($\rho = -0.007$, $z = 0.00825$) and with the reproduced trajectory was analyzed. As expected from the position of the orbit on the map, the spacecraft follows a QSO-like orbit around Phobos for about 150 revolutions, until it suddenly escapes from the moon. This is also confirmed when looking at the projections of the trajectory, shown in Fig. 6.7.

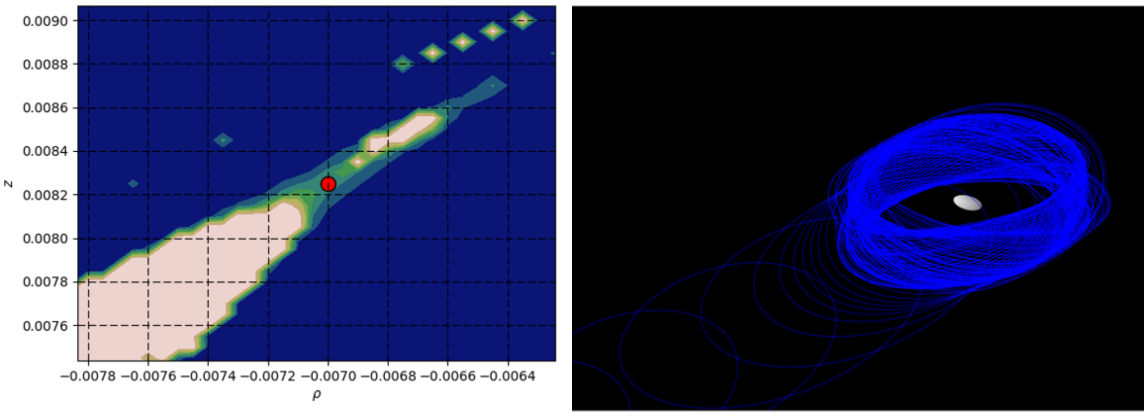

Figure 6.6: Initial conditions and trajectory of an escaping QSO from the escape gap of the QSO-H time-to-escape map.

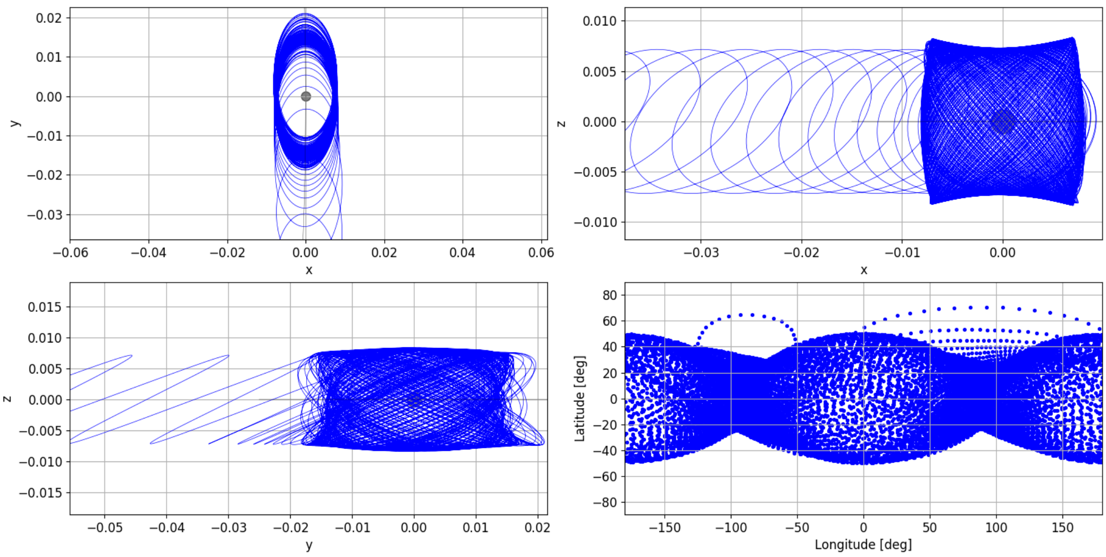

Figure 6.7: Projections of the trajectory of an escaping QSO from the escape gap of the QSO-H time-to-escape map.

Regarding the evolution of the disturbing function and guiding center, Fig. 6.8 shows a similar phenomenon to the one in the continental region: both peaks oscillate with a longer frequency than the guiding center. However, in this case the peaks go even far below the value of the disturbing function at the position of Phobos. This means that the convexity of the disturbing function close to Phobos changes periodically. At the times where the disturbing function is concave, the guiding center is not bounded, so it gains kinetic energy and is able to move further on a constant direction. This is shown in Fig. 6.8 around the epochs 20, 50, 80 and 115. At some point ($\tau \approx 150\, revs$), the guiding center oscillates so fast that the motion of the peaks is not able to catch up, allowing the guiding center to escape from the QSO region.

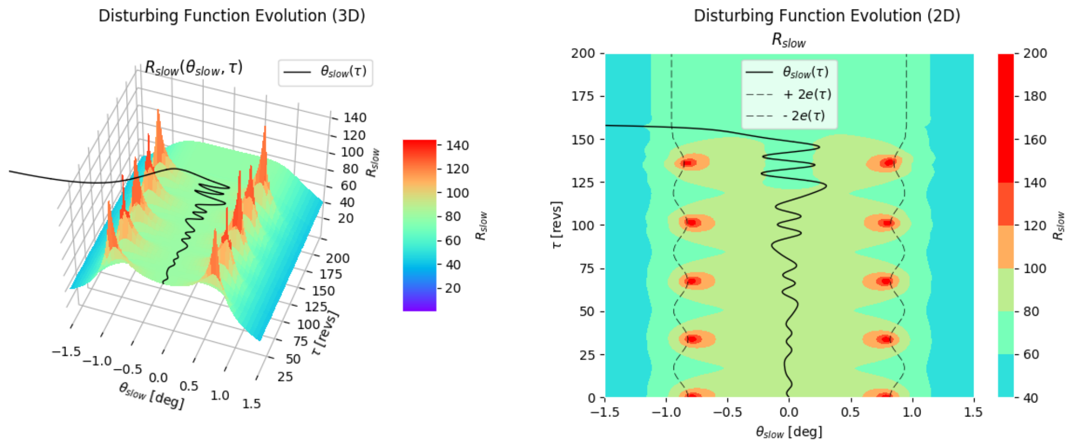

Figure 6.8: Motion of the guiding center and evolution of the disturbing function, for an escaping QSO from the escape gap of the QSO-H time-to-escape map.

The increase in the kinetic energy reached by the guiding center as well as the amplitude of its oscillations is reflected more clearly in Fig. B.1. As shown, when time goes on, the value of the disturbing function that the guiding center reaches when it crosses $\theta_{slow} = 0$ becomes smaller. In accordance with Eq. (4.12), this implies an increase in the kinetic energy which allows the guiding center to enlarge the amplitude of its oscillations and eventually escape from the QSO regime.

As for the evolution of the orbital parameters, presented in Fig. 6.9, the most insightful one is probably the semi-major axis, which determines the kinetic energy of the guiding center. As illustrated, the amplitude of its oscillations about unit also increases in time until the moment when it reaches a much higher value, meaning that the guiding center has escaped through the left side (i.e. the spacecraft rotates slower than Phobos when it escapes). Regarding eccentricity and inclination, a secular increase in eccentricity and decrease in inclination can be observed, but the major reason for the escape is the difference between the frequency of the oscillations of e and i with respect to the semi-major axis, thus, guiding center.

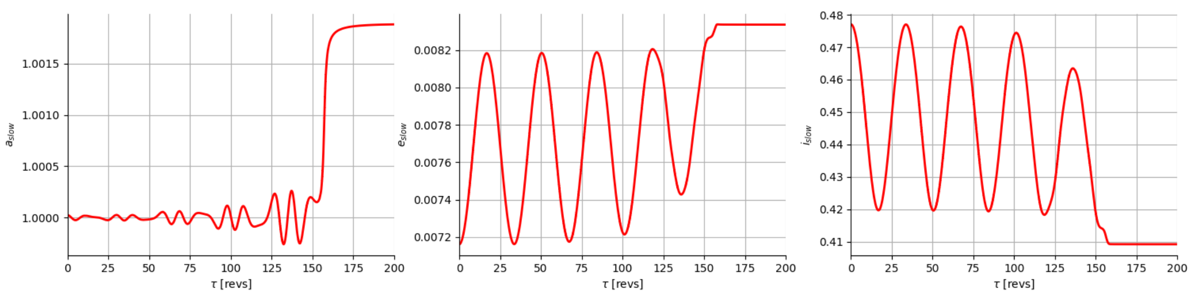

Figure 6.9: Slow evolution of the orbital parameters of an escaping QSO from the escape gap of the QSO-H time-to-escape map.

6.1.3. STABILITY ISLAND

Finally, the dynamics of the stability island (the biggest of the ones present in the time-to-escape map) of QSO-H were analyzed. The location of the orbit picked in this case, as well as the resulting orbit, is illustrated in Fig. 6.10. The projections of this orbit are presented in Fig. 6.11. As shown there, the trajectory reaches much higher positions in the out-of-plane component when compared with the continental QSO (Fig. 6.2).

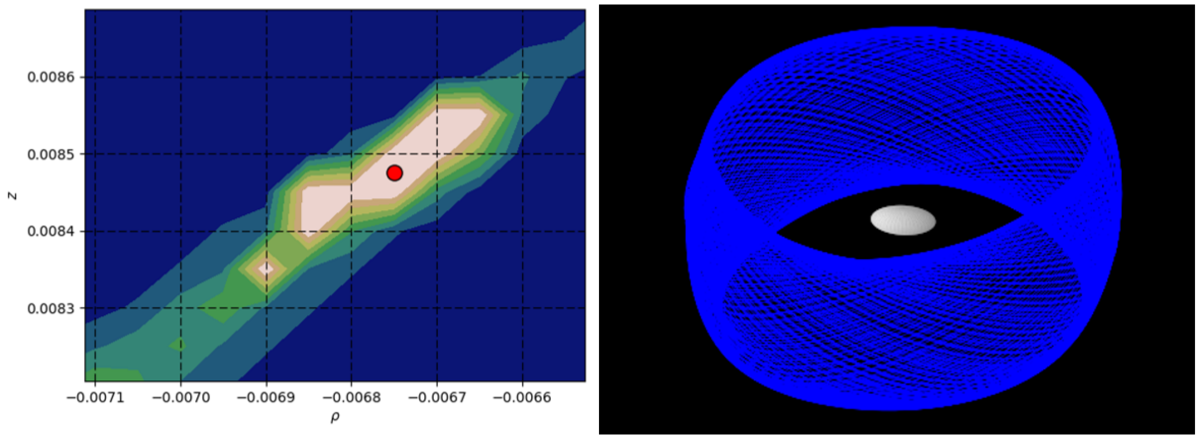

Figure 6.10: Initial conditions and trajectory of a stable QSO from the major island of the QSO-H time-to-escape map.

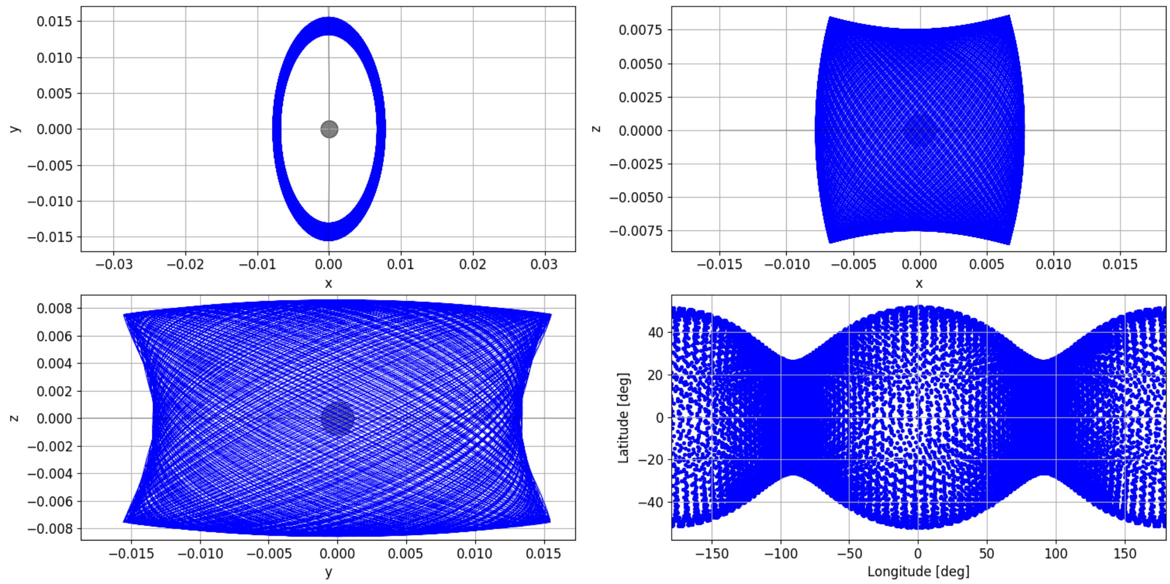

Figure 6.11: Projections of the trajectory of a stable QSO from the major island of the QSO-H time-to-escape map.

In terms of co-orbital motion, as shown in Figs. 6.12 and B.2, the behavior of the disturbing function is very similar to the one found in the escape gap (Figs. 6.8 and B.1). Nevertheless, in the case of the stability island the guiding center is very close to zero and with little velocity when the peaks go down. Hence, it is not able to increase its kinetic velocity and amplitude of its oscillations, which forces it to be forever trapped within the QSO region.

When looking at the evolution of the orbital parameters, one can see a quite erratic evolution of the semi-major axis (thus, the velocity of the guiding center). However, the amplitude of this erratic oscillation is always bounded and very small. On the other hand, the evolution of the eccentricity and inclination is again complementary and almost periodic in time. This means that the evolution of the shape in the disturbing function hardly changes secularly.

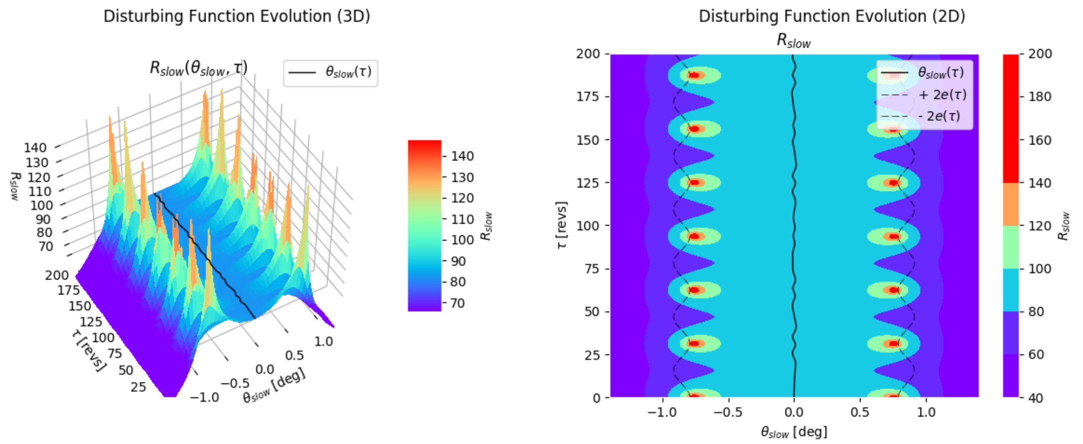

Figure 6.12: Motion of the guiding center and evolution of the disturbing function, for a stable QSO from the major island of the QSO-H time-to-escape map.

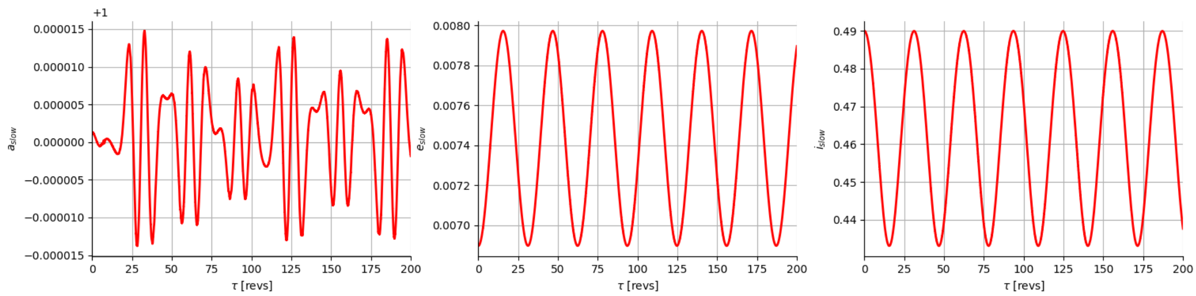

Figure 6.13: Slow evolution of the orbital parameters of a stable QSO from the major island of the QSO-H time-to-escape map.

6.2. MEDIUM QSO

The intermediate planar QSO to be flown by MMX lays 50 km away from the center of Phobos, with a value of the Jacobi constant of $C_j = 3 - 0.0000289435706313$. In this case, the gravitational potential of Phobos is already comparable to that of Mars, which leads to a time-to-escape map which is richer in texture when compared to QSO-H. In the case of QSO-M, the lateral boundaries of the continent are not so smooth, and the stability island is clearly separated from the continent and with a larger extension.

6.2.1. STABILITY CONTINENT

First, a stable QSO picked from the center of the continental region was examined, as shown in Fig. 6.14. As also shown in Fig. 6.15, the trajectory in this case is obviously much closer to the surface of Phobos than in the previous cases.

In terms of co-orbital motion, Figs. 6.16 and 6.17 reveal a similar behavior to the one observed in the continent of QSO-H: the guiding center oscillates relatively fast around the position of Phobos and it is always bounded by the shape of the disturbing function, whereas the peaks of the disturbing function rise and decrease together with a smaller frequency. Again, when looking at the value of the peaks, one can observe that they are at all times larger than the value of the disturbing function that the guiding center encounters. However, the strongest difference with respect to the continental orbit of QSO-H is that both the guiding center and the peaks of the disturbing function oscillate faster in the case of QSO-M.

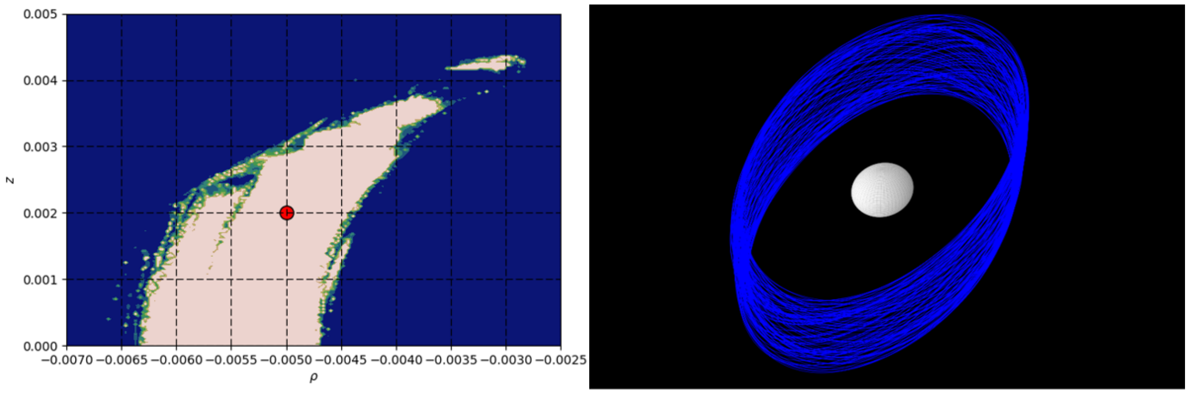

Figure 6.14: Initial conditions and trajectory of a stable QSO from the stability continent of the QSO-M time-to-escape map.

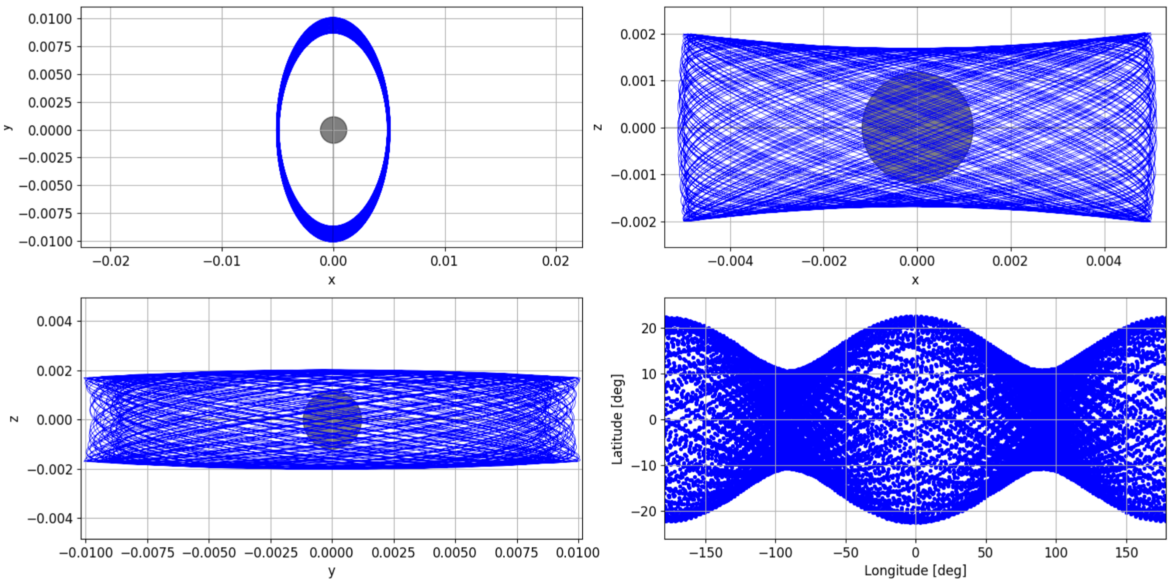

Figure 6.15: Projections of the trajectory of a stable QSO from the stability continent of the QSO-M time-to-escape map.

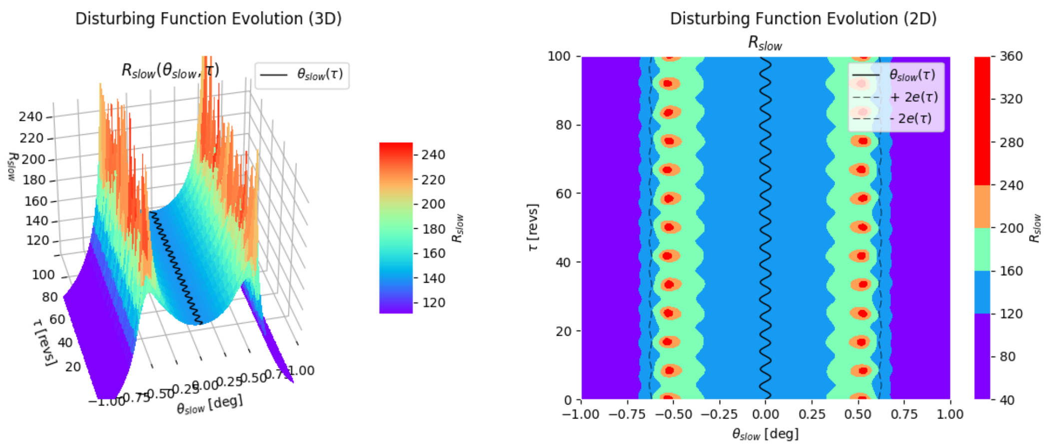

Figure 6.16: Motion of the guiding center and evolution of the disturbing function, for a stable QSO from the stability continent of the QSO-M time-to-escape map.

The faster oscillations are also reflected in the evolution of the orbital elements presented in Fig. 6.18.

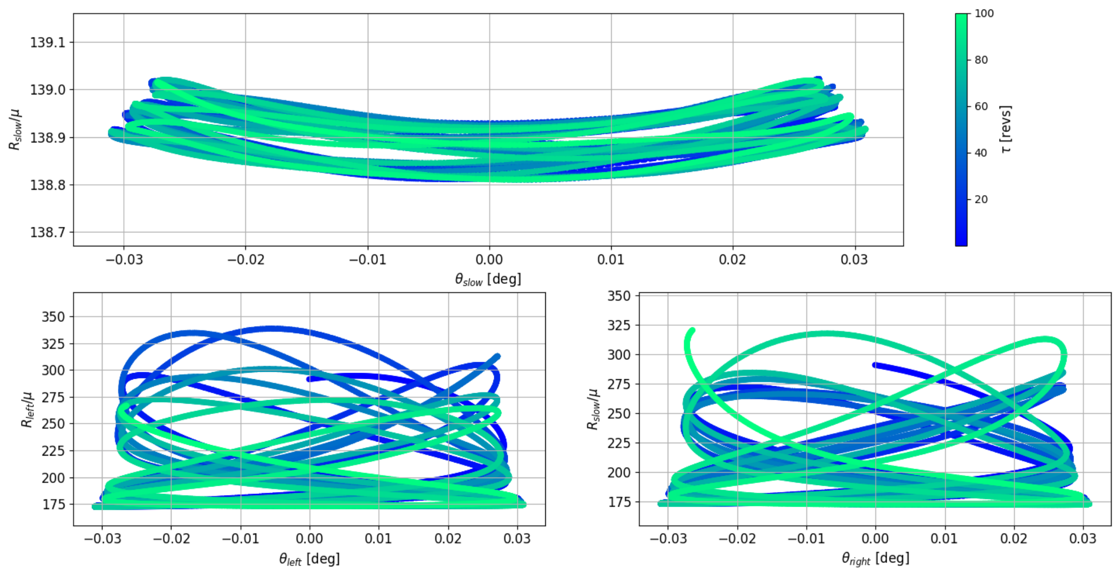

Figure 6.17: Value of the disturbing function seen by the guiding center (top) and value of the left and right maxima (bottom), as a function of the location of the guiding center in time.

Also, as in the case of QSO-H, the semi-major axis oscillates faster than the eccentricity and inclination, with the frequency of the guiding center and the peaks of the slow disturbing function respectively. Again, when the eccentricity is large and the inclination small, the value of the peaks in the disturbing function is larger than in the opposite situation.

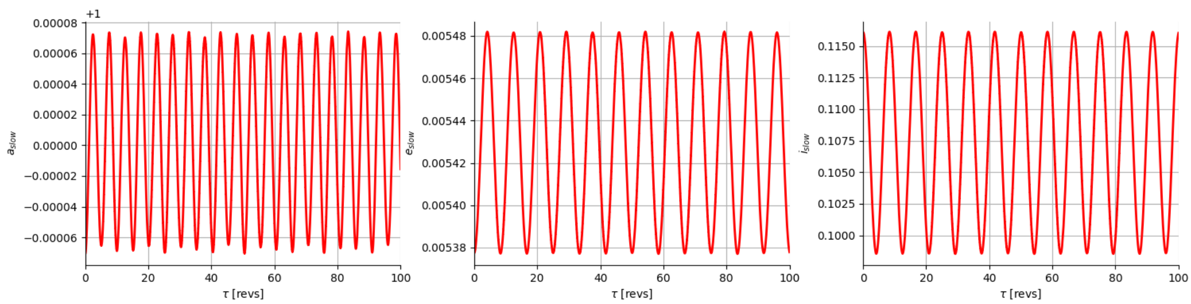

Figure 6.18: Slow evolution of the orbital parameters of a stable QSO from the stability continent of the QSO-M time-to-escape map.

6.2.2. ESCAPE GAP

Following the same analysis as in the previous section, the next region to study is the gap between the stability continent and the island of QSO-M. The orbit to be simulated in this region is shown in Fig. 6.19. Fig. 6.20 shows the 2-dimensional projections of the trajectory of the spacecraft around Phobos. As shown, and in accordance with the position of the orbit in the time-to-escape map, the spacecraft escapes the vicinity of Phobos very soon, just after a few revolutions around the moon. Furthermore, the trajectory passes really close to the surface of Phobos, so the risk of collision is very high in this orbit.

The early escape is also noticeable in the co-orbital analysis, Figs. 6.21 and B.3, where it is shown that the guiding center leaves the region between the peaks of the slow disturbing function after just about 12 revolutions of Phobos. As in the case of the gap of QSO-H, the peaks recursively rise and decrease, while the guiding center earns kinetic energy and amplitude of motion when the peaks are at their lowest, eventually escaping. This however occurs much more rapidly than in the case of QSO-H.

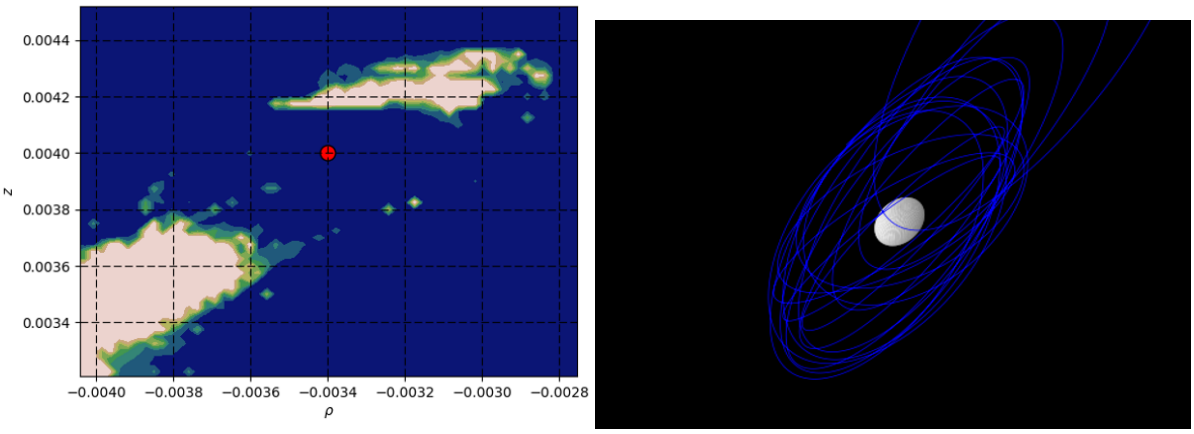

Figure 6.19: Initial conditions and trajectory of an escaping QSO from the escape gap of the QSO-M time-to-escape map.

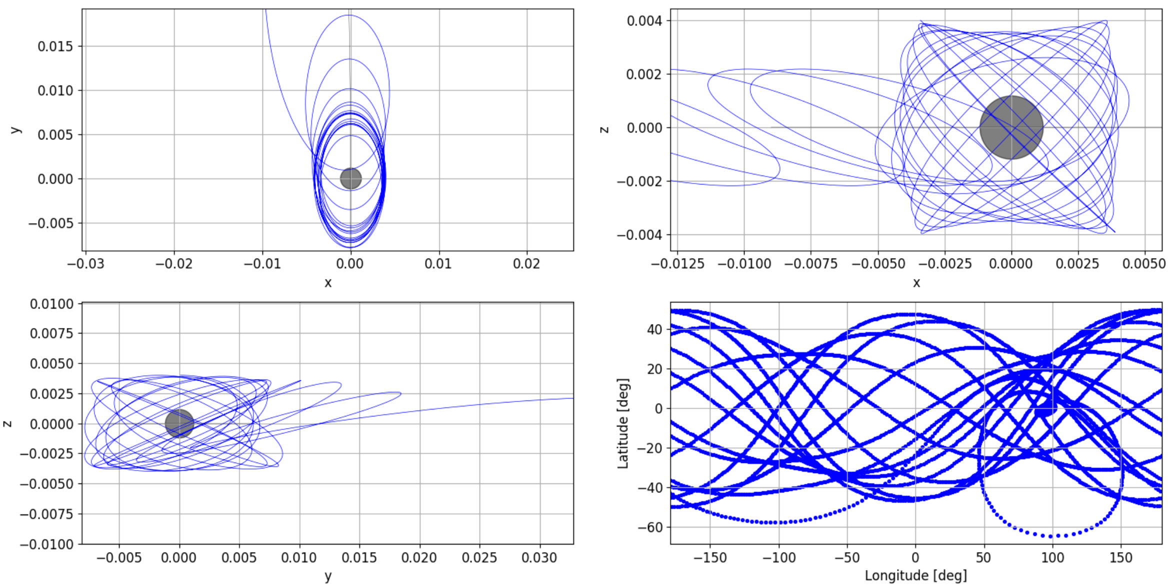

Figure 6.20: Projections of the trajectory of an escaping QSO from the escape gap of the QSO-M time-to-escape map.

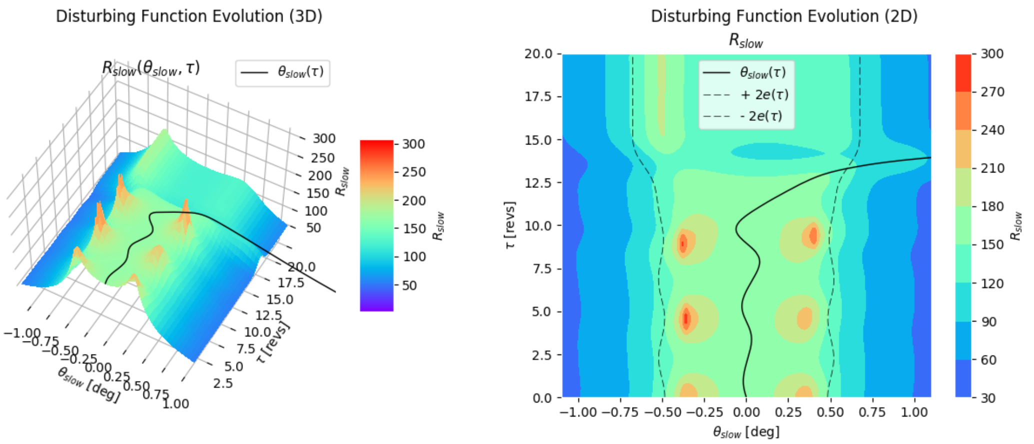

Figure 6.21: Motion of the guiding center and evolution of the disturbing function, for an escaping QSO from the escape gap of the QSO-M time-to-escape map.

Regarding the orbital parameters, depicted in Fig. 6.22, the increase in kinetic energy of the guiding center is again reflected in the semi-major axis, until it reaches a significantly smaller value than unit, meaning that the guiding center escapes through the right side. Note however that the guiding center can in principle escape through each of the two sides, since both peaks decrease at the same time. The eccentricity and inclination evolve again with the frequency of the peaks of the disturbing function, but with a secular component that tends to increase the eccentricity and decrease the inclination. By looking at the correlation of the hills of those parameters with the motion of the peaks in the disturbing function, one can determine that this leads to a secular decrease in the value of the peaks, which also contributes to the prompt escape of the guiding center.

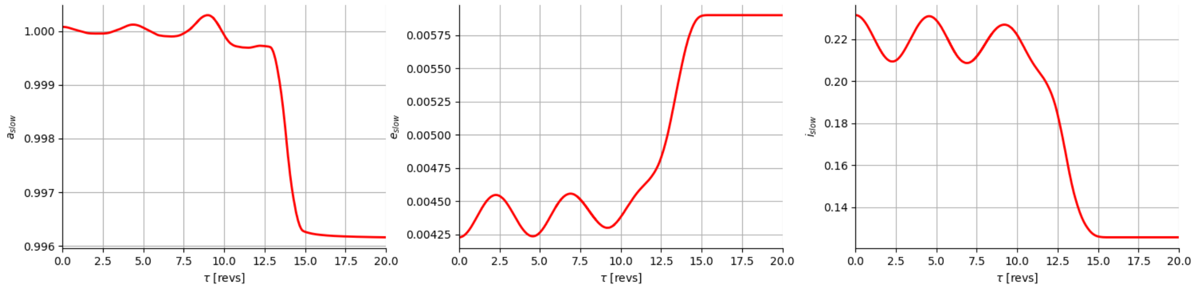

Figure 6.22: Slow evolution of the orbital parameters of an escaping QSO from the escape gap of the QSO-M time-to-escape map.

6.2.3. STABILITY ISLAND

Finally, the stability island of QSO-M is studied, by analyzing the orbit presented in Fig. 6.23. As shown in Fig. 6.24, the latitudes reached by this orbit go beyond all the ones of the previous cases, over 50°.

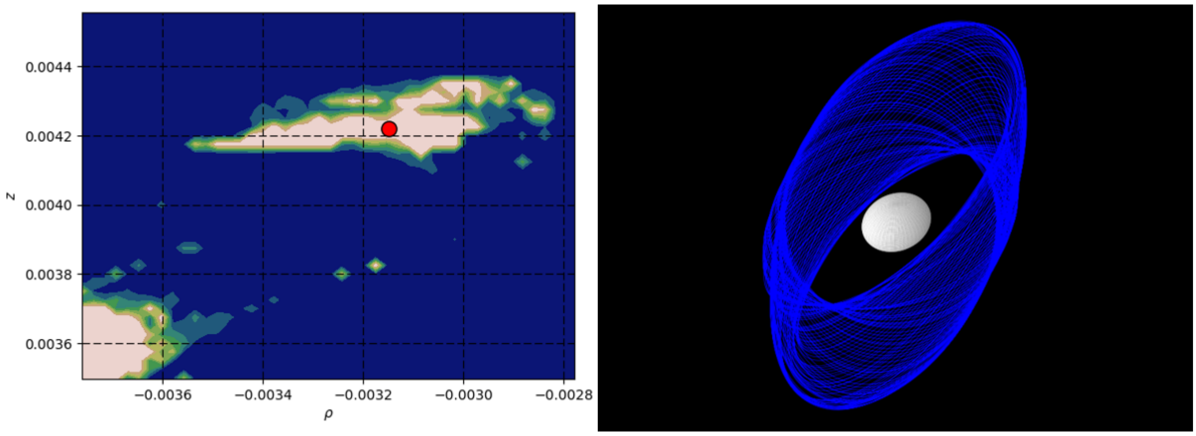

Figure 6.23: Initial conditions and trajectory of a stable QSO from the major island of the QSO-M time-to-escape map.

The disturbing function (Figs. 6.25 and B.4) again evolves with an oscillation of the value of its peaks, where the convexity of the function changes alternatively. however, in this case the oscillation is fast enough to block the motion of the guiding center repeatedly, without allowing it to increase its kinetic energy and amplitude of the oscillations. A difference with respect to the island of QSO-H is the asymmetry of the motion of the peaks in this case.

Finally, regarding the orbital elements, Fig. 6.26 exposes a similar behavior to the one observed in QSO-H: a repetitive complementary oscillation of eccentricity and semi-major axis, which correlates with the motion of the peaks, and an erratic –though small in amplitude– evolution of the semi-major axis.

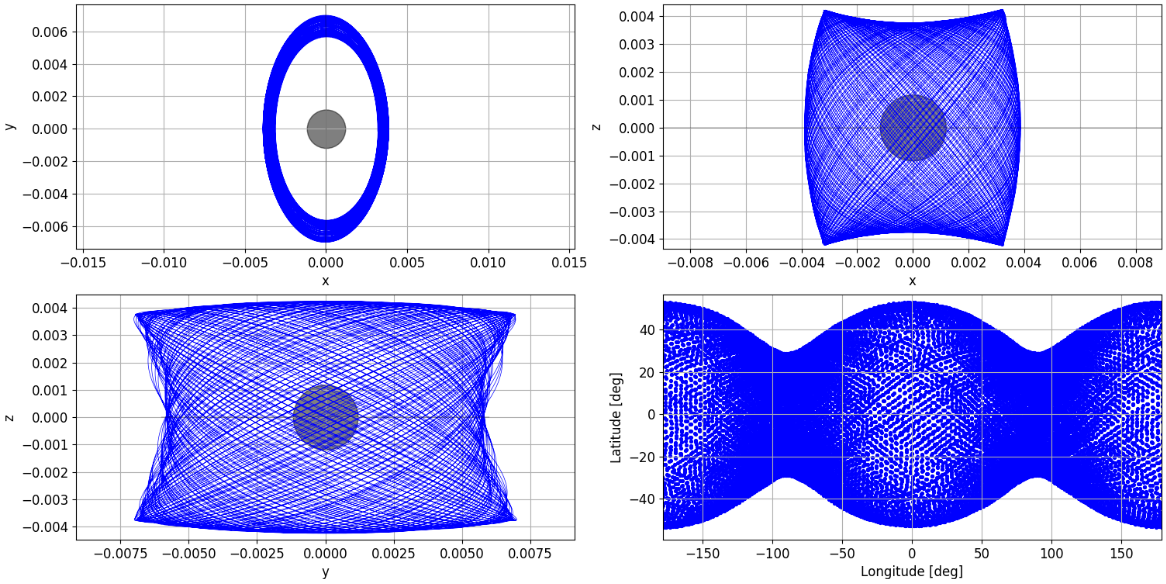

Figure 6.24: Projections of the trajectory of a stable QSO from the major island of the QSO-M time-to-escape map.

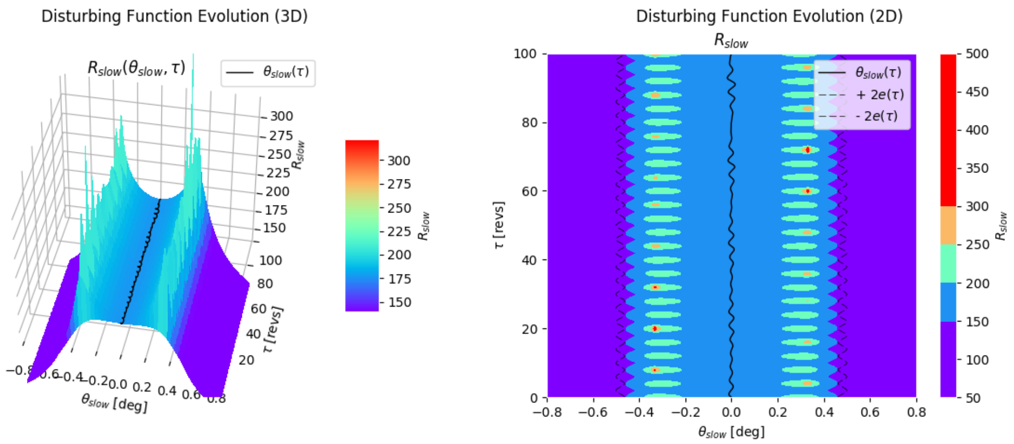

Figure 6.25: Motion of the guiding center and evolution of the disturbing function, for a stable QSO from the major island of the QSO-M time-to-escape map.

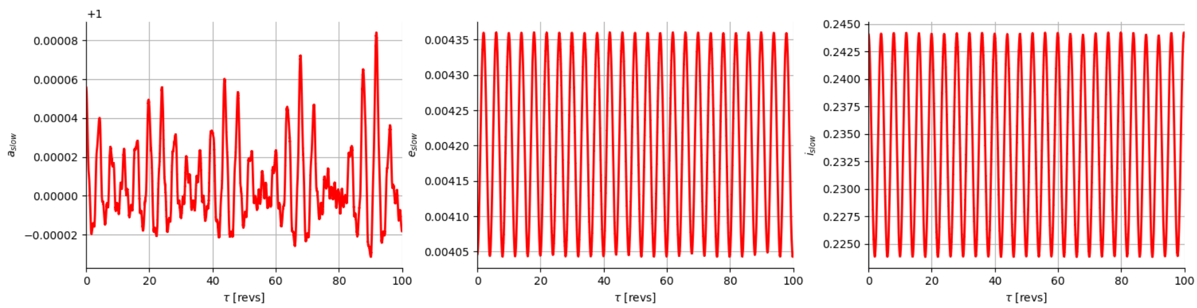

Figure 6.26: Slow evolution of the orbital parameters of a stable QSO from the major island of the QSO-M time-to-escape map.

6.3. Low QSO

The last and most demanding nominal orbit to be flown by MMX is QSO-L, which lays about 30 km from the center of Phobos. This orbit is clearly the one for which the gravitational effect of Phobos on the spacecraft is the largest, quite comparable to the attraction of Mars. This phenomenon is also responsible of the shape of the time-to-escape map, where the extension of the island is even comparable to the continent.

6.3.1. Stability continent

As usual, the first region to focus on is the continent of the time-to-escape map, this time of QSO-L. For this, the orbit highlighted in Fig. 6.27 was analyzed. When looking at the projections of the trajectory in Fig. 6.28, it is easy to recognize the proximity of the trajectory to Phobos. Also, the shape of the envelope defined by this non-periodic orbit is slightly different to the ones presented before (e.g. the lateral limits of the x-z projection).

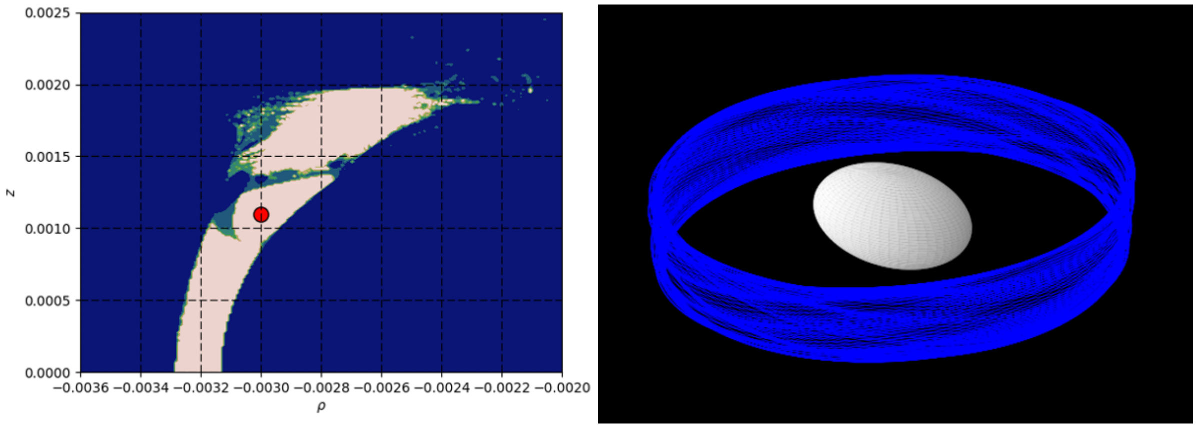

Figure 6.27: Initial conditions and trajectory of a stable QSO from the stability continent of the QSO-L time-to-escape map.

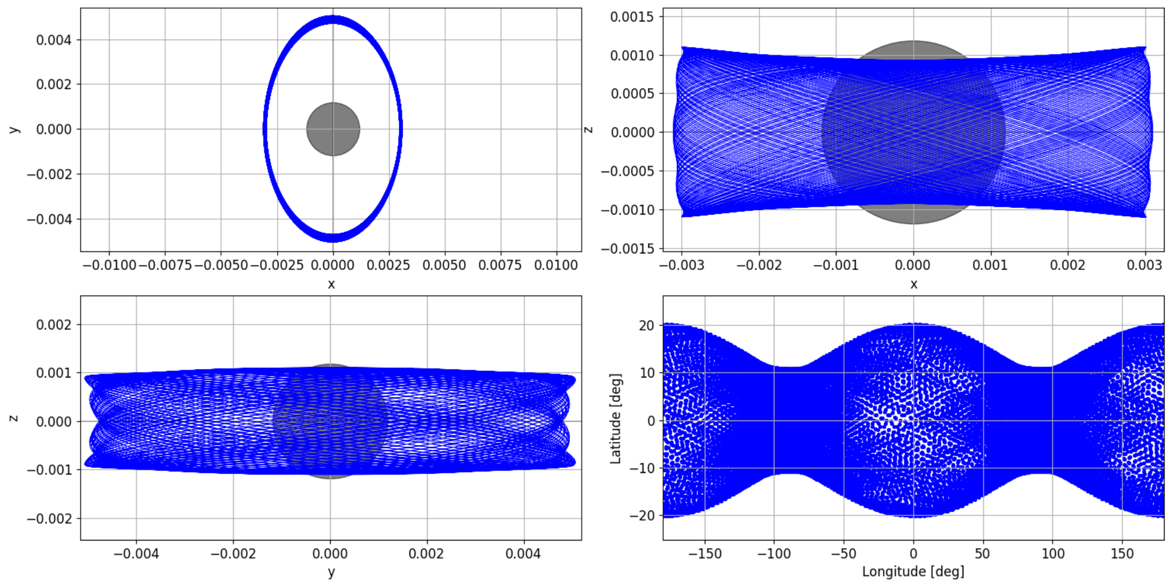

Figure 6.28: Projections of the trajectory of a stable QSO from the stability continent of the QSO-L time-to-escape map.

With respect to the disturbing function, one can observe a really fast oscillation of the peaks with a period of just a small number of revolutions. Nevertheless, there is a longer oscillation of about 30 revolutions period, which causes the extremes of the disturbing function to rise very sharply. Nevertheless, the guiding center is bounded very deep within the valley of the disturbing function at all times, just as in the previous continental orbits. Another different feature to note in this case is the great inaccuracy in the analytic prediction of the peaks at $\pm 2e$. This is a sign of the unsuitability of the analytic expressions for the disturbing function when being so close to the moon.

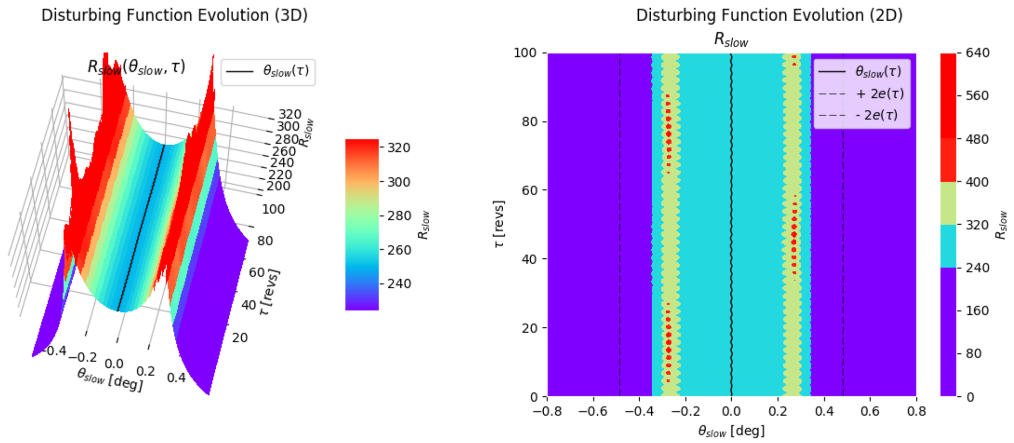

Figure 6.29: Motion of the guiding center and evolution of the disturbing function, for a stable QSO from the stability continent of the QSO-L time-to-escape map.

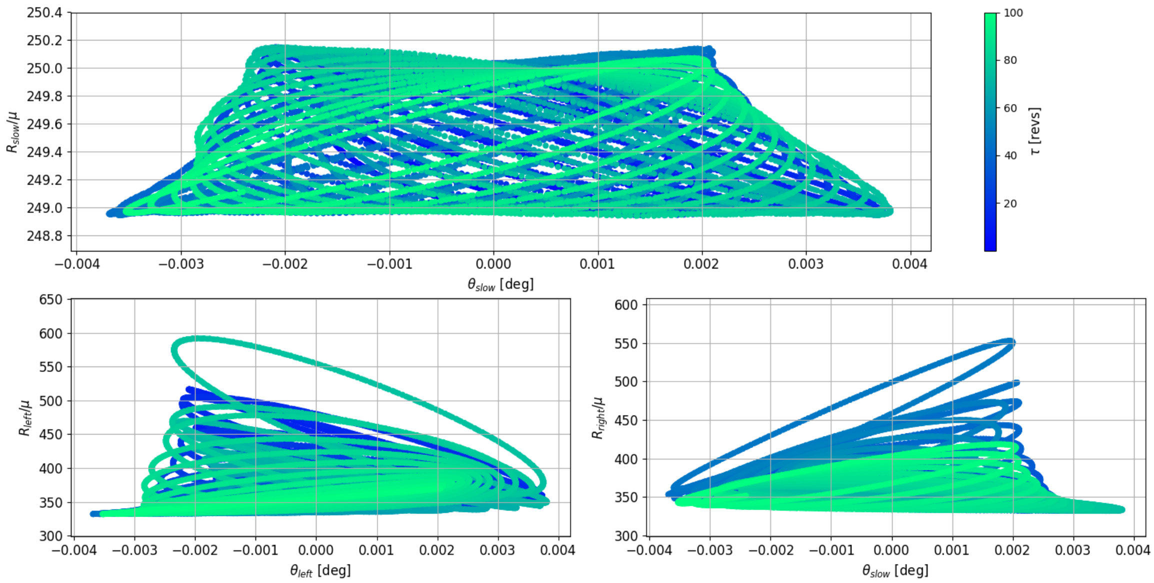

Figure 6.30: Value of the disturbing function seen by the guiding center (top) and value of the left and right maxima (bottom), as a function of the location of the guiding center in time.

Fig. 6.31 shows the evolution of the orbital parameters of the spacecraft. As shown, eccentricity and inclination experience a fast oscillation with period of a few revolutions, which are correlated with those seen in Fig. 6.29. Also, on top of those there is a slower quasi-periodic oscillation which also leads to the change in the peaks, with a period of about 30 revolutions. The semi-major axis, as always responsible for the velocity of the guiding center, also experiences fast oscillations superimposed upon a longer period motion. However, the values that it reaches are always bounded and very close to unity.

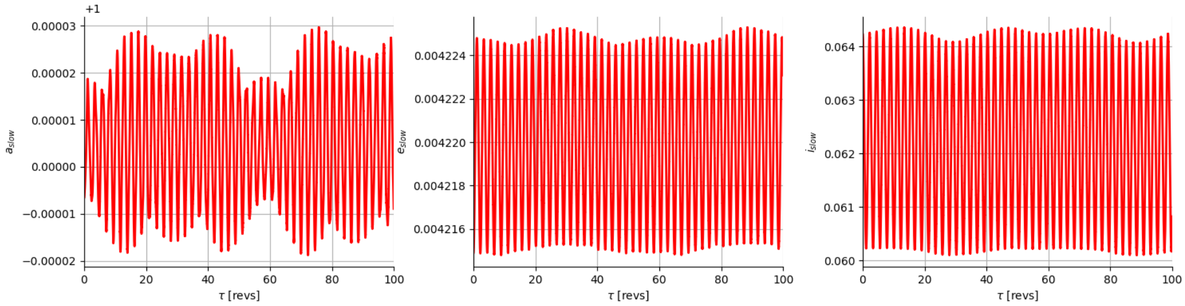

Figure 6.31: Slow evolution of the orbital parameters of a stable QSO from the stability continent of the QSO-L time-to-escape map.

6.3.2. Escape gap

Second, orbits within the gap between the continent and main island were studied for QSO-L, as they were for the previous cases. The escaping orbit selected as benchmark for this region is depicted in Fig. 6.32, whereas the projections of the trajectory are depicted in Fig. 6.33. As shown, in this case the spacecraft not only escapes from the QSO regime after a number of revolutions, but it also impacts with the surface of Phobos along the way. This is a sign of the importance of stability analysis like the present one for the safety of the mission, especially for orbits close to the surface of Phobos like those in the QSO-L time-to-escape map.

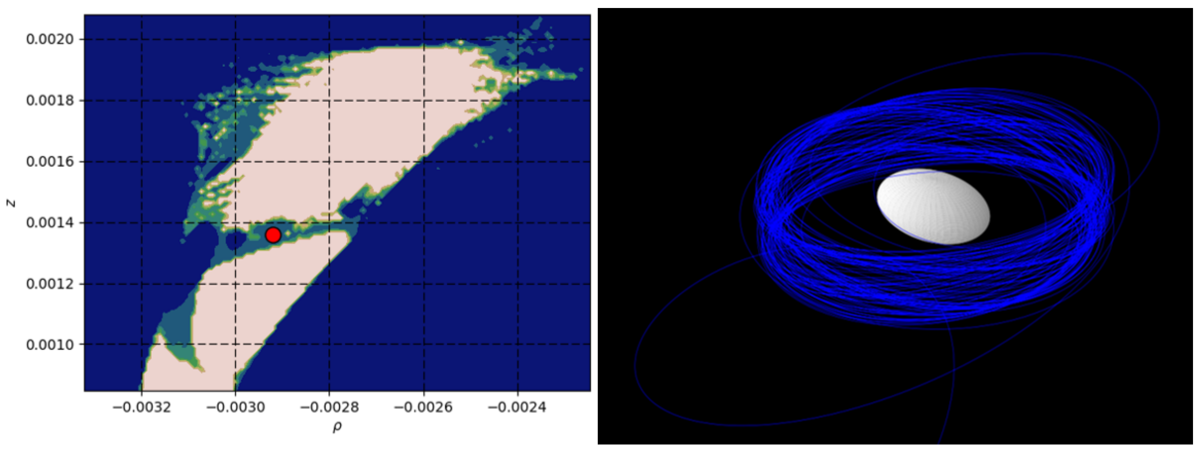

Figure 6.32: Initial conditions and trajectory of an escaping QSO from the escape gap of the QSO-L time-to-escape map.

As Figs. 6.34 and B.5 show, the co-orbital behavior is relatively similar to the ones observed in the gap regions of QSO-H and QSO-M: the guiding center increases the amplitude of its oscillations until a point when it is able to overcome the value of one of the peaks of the disturbing function. However, a feature to be noted in Fig. B.5 which contrasts with the previous cases is the fact that the disturbing potential seen by the guiding center also increases in time. This means that both the kinetic and potential terms in (4.12) increase at the same time for this orbit, which again proves that some of the analytic expressions derived in Chapter 4 are no longer valid in the case of QSO-L. Note however that the results presented in this analysis are obtained purely numerically, so they are independent of those analytic expressions.

The evolution of the orbital parameters, shown in Fig. 6.35, shows again an increase in the amplitude of the oscillations of the semi-major axis, until the moment when it increases far beyond unity (escape through the left side). With respect to eccentricity and inclination, the first one slowly decreases while the second increases, up until a moment when there is a sudden step in the two, leading to the exit of the guiding center. After the escape, both inclination and eccentricity reach much higher values than in the QSO regime, so the disturbing function decreases globally. The Tisserand parameter is balanced through the also dramatic change in the semi-major axis mentioned before.

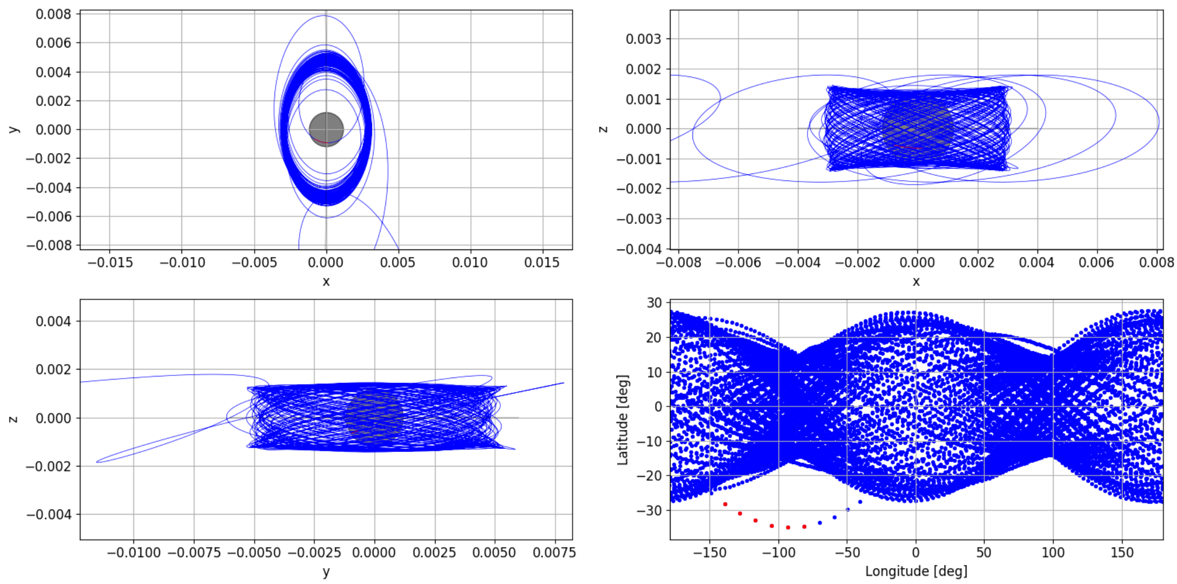

Figure 6.33: Projections of the trajectory of an escaping QSO from the escape gap of the QSO-L time-to-escape map.

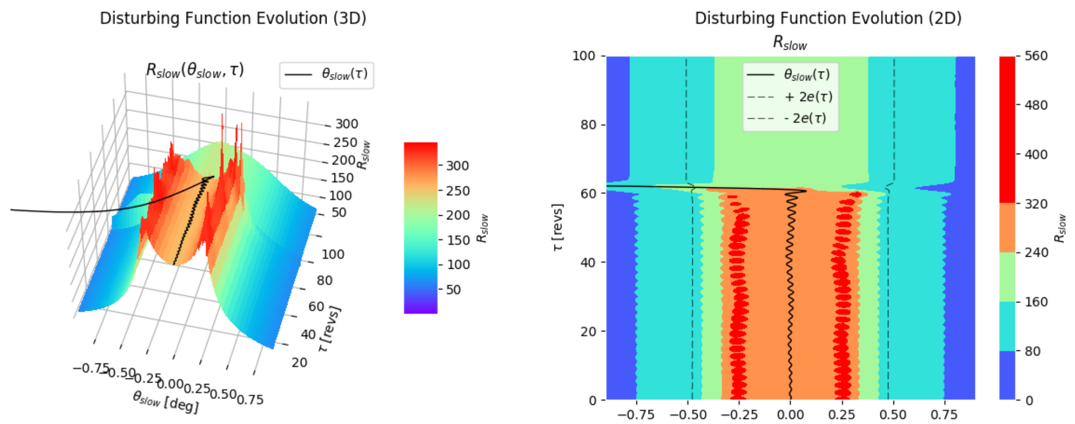

Figure 6.34: Motion of the guiding center and evolution of the disturbing function, for an escaping QSO from the escape gap of the QSO-L time-to-escape map.

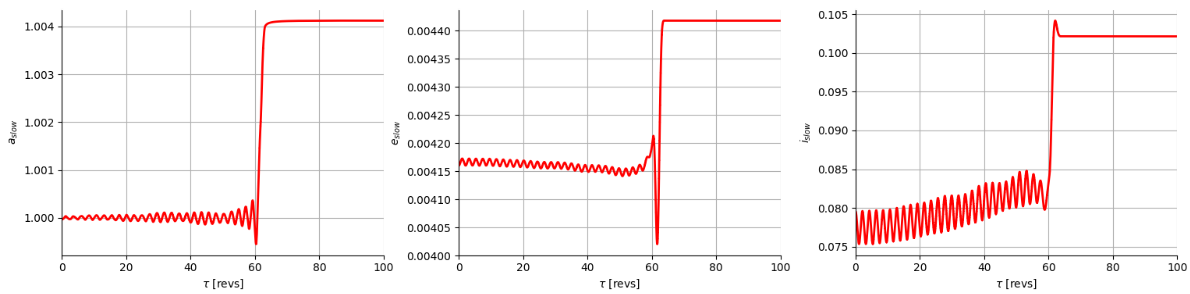

Figure 6.35: Slow evolution of the orbital parameters of an escaping QSO from the escape gap of the QSO-L time-to-escape map.

6.3.3. Stability island

Finally, an orbit within the stability island of QSO-L, shown in Fig. 6.36, was examined. The projections of the trajectory are presented in Fig. 6.37, where it is shown that latitudes of about 30° are reachable. Since the orbit is also close to the surface of Phobos, the resolution of the scientific measurements attainable from this kind of orbit will be higher than from those of stability islands of QSO-H and QSO-M, despite its lower inclination.

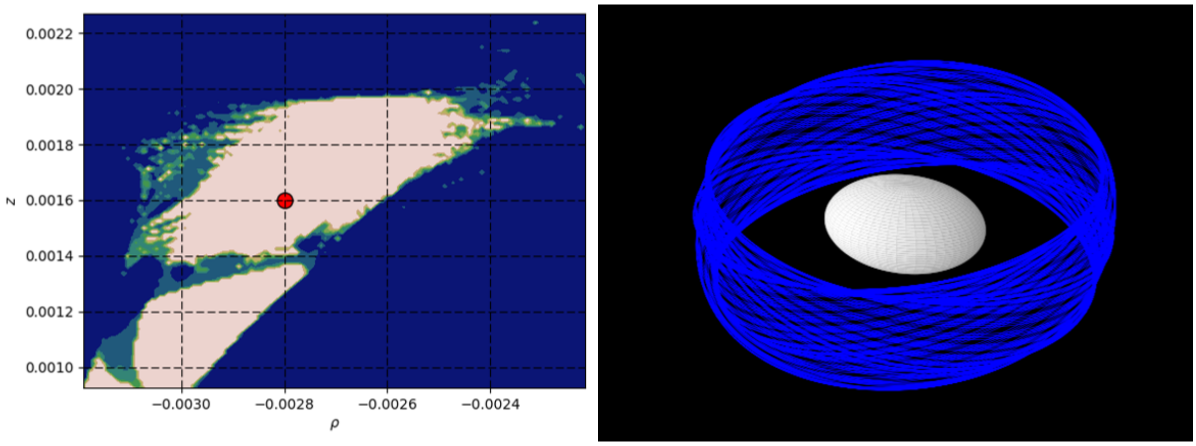

Figure 6.36: Initial conditions and trajectory of a stable QSO from the major island of the QSO-L time-to-escape map.

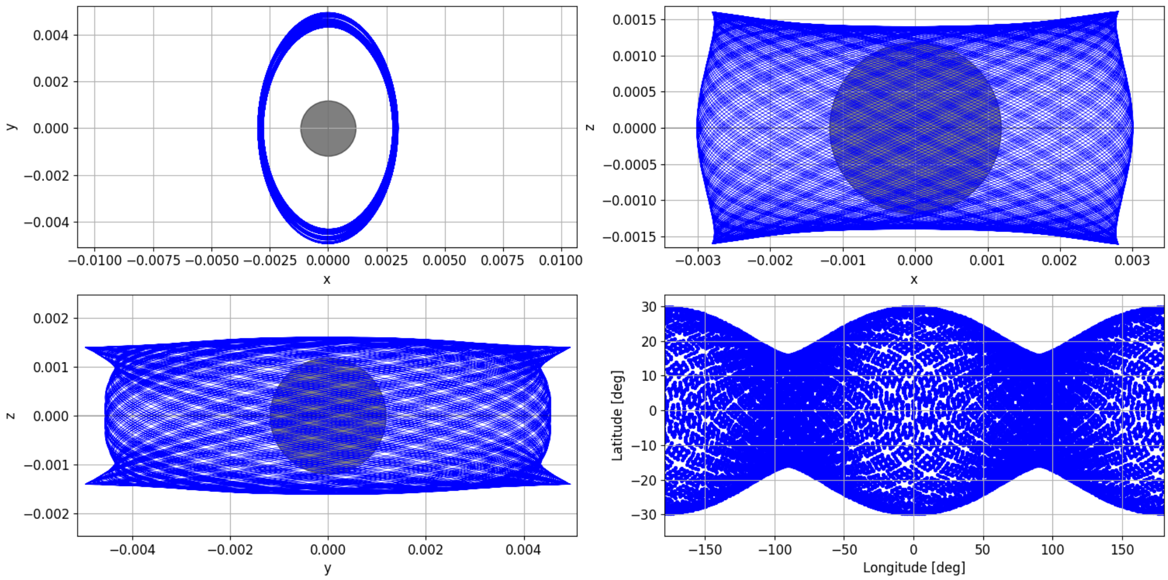

Figure 6.37: Projections of the trajectory of a stable QSO from the major island of the QSO-L time-to-escape map.

With respect to the co-orbital analysis of the orbit, Figs. 6.38 and B.6 show a different behavior to those on the islands of QSO-H and QSO-M. In this case, even though the minimum value of the peaks is considerably smaller and the oscillations of the guiding center larger than in the continental orbit, the convexity of the disturbing function never changes, and the guiding center is always bounded deep inside the QSO valley. As shown in Fig. B.6, the value of the disturbing potential seen by the guiding center is bounded and hardly varies, whereas the peaks suffer intense but bounded oscillations, always being much higher than the disturbing function seen by the guiding center.

Finally, the orbital parameters exhibit again fast oscillations about their mean values, however hardly any secular evolution is noticeable. In particular, the changes in the semi-major axis are very small in amplitude, which explains the little oscillations of the guiding center.

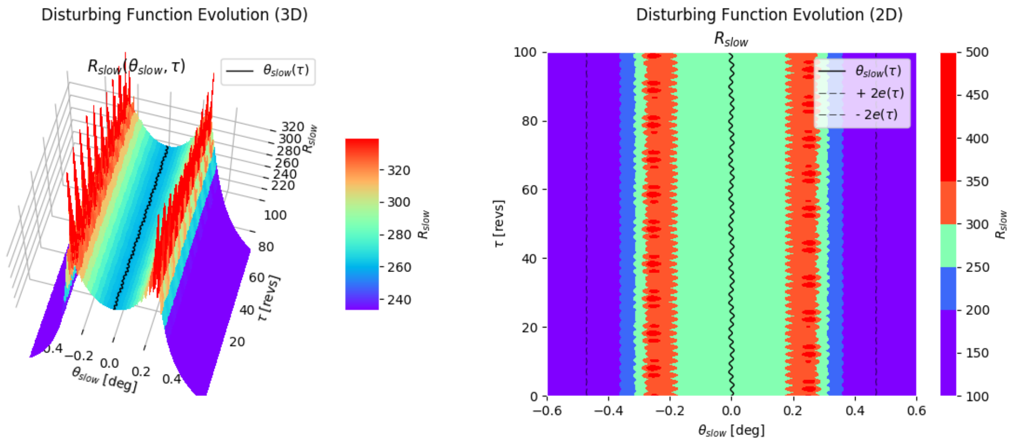

Figure 6.38: Motion of the guiding center and evolution of the disturbing function, for a stable QSO from the major island of the QSO-L time-to-escape map.

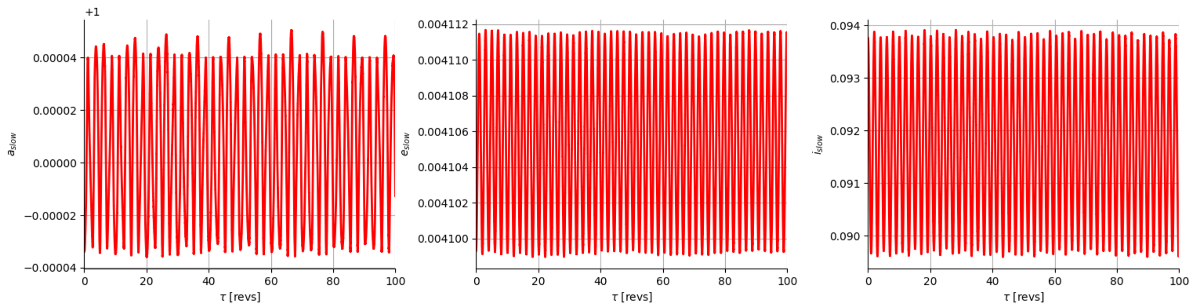

Figure 6.39: Slow evolution of the orbital parameters of a stable QSO from the major island of the QSO-L time-to-escape map.

7

PERIODIC QSO WITHIN STABILITY ISLANDS

Once the characteristics of co-orbital motion within different regions in the time-to-escape map (continent, gap and islands), and for different energetic levels (QSO-H, QSO-M and QSO-L) have been analyzed, the next natural step is to exploit these insights in benefit of the MMX mission. The present chapter will be devoted to express a novel methodology designed to find periodic and stable orbits able to reach high latitudes over the surface of Phobos, based on the co-orbital analysis provided in Chapter 6. This methodology involves two consecutive steps: a multi-objective optimization to isolate good candidates, based on co-orbital motion, followed by a single-shooting technique to arrive at the actual optimal periodic QSO.

The goal of this methodology is to find periodic QSO's on the islands of the time-to-escape maps. Those are reasonably wide stability regions (particularly wide for QSO-M and QSO-M) where no periodic orbit was found so far, and where the highest latitudes on each map are reached. On top of the direct applicability for MMX, finding periodic stable orbits on the islands would serve as an explanation for the existence of such stability regions separated from the continent.

7.1. CONCLUSIONS FROM CO-ORBITAL ANALYSIS

The co-orbital analysis conducted in Chapter 6 resulted in several global conclusions. First of all, as already predicted in Chapter 4, the shape of the disturbing function evolves in time given the change in the orbital elements induced by the perturbing effect of Phobos' gravity. When the disturbing function is clearly convex and the guiding center is located near the bottom of the valley, as in the continental orbits, the motion is in general stable in the long run.

However, as the inclination of the orbits increase, sometimes the changes in the shape of the disturbing function allow for the guiding center to gradually increase its kinetic energy, thus enlarging the amplitude of its oscillations. When this happens, the orbital parameters experience secular changes that might affect the shape of the disturbing function so drastically that in the end the guiding center is able to escape from the QSO regime. This is the situation that takes place in the escape gap.

The co-orbital dynamics observed in the stability islands is quite unique and different to that of the continent. In general, the peaks of the disturbing function fluctuate as in the case of the escape gap, sometimes even shifting the convexity of the disturbing function close to Phobos. Nevertheless, when the peaks of the disturbing function are at their lowest, the guiding center is always located very close to Phobos and with little velocity. This means that the kinetic energy of the guiding center hardly increases, so it remains locked in the vicinity of Phobos.

Regarding the differences between the energy levels, several conclusions can also be drawn. First of all, the evolution of the guiding center, disturbing function and orbital parameters is in general smoother the larger the distance of the spacecraft to Phobos. In this sense, the oscillation of all these parameters is faster when the size of the orbit is smaller. With respect to the shape of the slow disturbing function, the closer the orbit, the sharpest are the peaks, and the higher the value of the disturbing function at $\theta_{slow} = 0$. Also, the disturbing function is more convex close to Phobos the smaller the orbit. In particular, regarding the stability islands, only for QSO-H and QSO-M the convexity changes sign when the peaks are at their lowest.

7.2. CO-ORBITAL MULTI-OBJECTIVE OPTIMIZATION

The first step in the proposed strategy to search for periodic three-dimensional QSO's with high inclinations (on stability islands) consists in a multi-objective minimization based on the conclusions of the co-orbital analysis summarized in Section 7.1. The two independent variables of this optimization are (ρ, z), which point at a specific location on each time-to-escape map. After recomputing the value of $\dot{\theta}$, the orbit is propagated forwards over about 40 Phobos revolutions (design parameter), using the equations of motion in curvilinear coordinates (see Section 3.3) and an RK45 algorithm with absolute and relative tolerances of 10^{-12}. With the propagated orbit, the position and velocity of the guiding center are obtained through numerical averaging, as well as the evolution of the complete disturbing function (see Section 4.5).

7.2.1. TARGET FUNCTIONS

As pointed out in Section 7.1, for orbits on stability islands the disturbing function changes shape drastically and repeatedly. At certain times, the peaks of the disturbing function lower their values so dramatically that the guiding center becomes unbounded, but before it moves far from Phobos the peaks of the function rise again. This only occurs because the guiding center is close to Phobos and with little velocity when the peaks are at their lowest. Hence, the position and velocity of the guiding center when the peaks are at their lowest are the first two target functions to minimize:

$$f_1 = \frac{1}{2}\left(|\theta_{slow}|_{R_{left,min}} + |\theta_{slow}|_{R_{right,min}}\right) \tag{7.1}$$

$$f_2 = \frac{1}{2}\left(|\dot{\theta}_{slow}|_{R_{left,min}} + |\dot{\theta}_{slow}|_{R_{right,min}}\right) \tag{7.2}$$

In addition, according to the results of the analysis, it is known that orbits within the stability gap become unstable due to an increase in the kinetic energy of the guiding center, which enlarges the amplitude of its oscillations. In order to minimize this effect, the extremes of each oscillation of the guiding center are identified. Then, a linear interpolation is performed in order to identify the trend in the amplitude of the oscillations. The absolute value of this trend, i.e. the linear coefficient in the interpolation, is chosen as the last target function in the multi-objective minimization, Eq. (7.3), so that the amplitude of the oscillation ideally hardly changes. Fig. 7.1 illustrates the procedure followed to obtain the value of f_3: motion of the guiding center (cyan), absolute value of the guiding center (blue), absolute value of the peaks (red) and linear interpolation of the peaks (black). The absolute value of the slope of the interpolated black line (i.e. long-term trend of the amplitude of motion) is the computed value of f_3.

$$f_3 \approx \left|\frac{d\left(\theta_{max}\right)}{d\tau}\right| \tag{7.3}$$

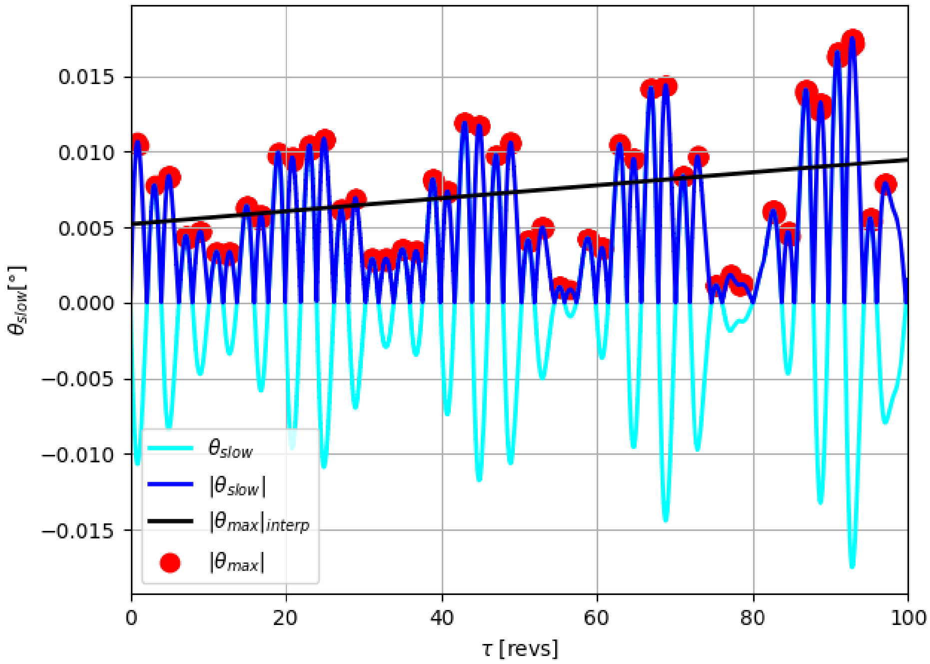

Figure 7.1: Interpolation performed to obtain f_3 for the orbit in the island of QSO-M (see Fig. 6.23). The motion of the guiding center is shown in cyan whereas its absolute value is in blue. The absolute value of the peaks are identified with the red dots, and they are linearly interpolated by the black line, whose slope is f_3.

7.2.2. ALGORITHM AND PARETO FRONT

The multi-objective minimization consist in an algorithm that tries to improve at the same time the three objective functions. However, in general a trade-off is to be made in order to choose between solutions that minimize different functions. This is in particular the case when a weighted linear combination of the three performance indices is made. Clearly, in that case the optimum would depend on the values given to those weighting factos. Nevertheless, since no weighting factor is provided in this case, the algorithm aims to find the so-called Pareto front of the problem. This is, in general, a hyper-surface beyond which no solution exists, which defines the locus of all the optimal solutions, for any value of the weighting parameters. In the current application, since there are three target parameters to minimize, the Pareto front is a three-dimensional surface.

With respect to the implementation, the software used for multi-target optimization in Python is *platypus.py* [43], an open-source library with multiple algorithms implemented and validated. The algorithm used is the Elitist Non-dominated Sorting Genetic Algorithm (NSGA-II). With this algorithm, a randomly distributed population is initially generated and improved after each iteration through breeding and mutation, while maintaining the closest individuals to the Pareto front (elite). The details of the implementation and performance of this algorithm are beyond the scope of this report, but they can be found in [44].

7.3. SHOOTING OPTIMIZATION

The second part of the method consists in a conventional single-shooting method. Up to this point, nothing is known about the period of the potential orbit to be found. Furthermore, only regions with several potential candidates are identified, of which the best guess is in principle unknown. Therefore, an intermediate optimization is required in order to provide a single best guess for the single-shooting method, together with a guess for the period of the orbit. The output of this optimization is directly inputted into the single-shooting algorithm, providing if successful the resulting optimal fully periodic orbit.

7.3.1. SLSQP OPTIMIZATION

For the intermediate step between the multi-objective optimization and the single-shooting, a Sequential Least Squares Quadratic Programming (SLSQP) algorithm is chosen. This is essentially a variation of the Newton-Raphson method to find the zero of the gradient of the objective function in constrained problems. In particular, this problem is only constrained to the limits of the map. The SLSQP algorithm is available and validated for Python within the *scipy.py* library [45].

As in the previous step, the independent variables of the optimization are the coordinates on the time-to-escape map (ρ, z), whereas the velocity $\dot{\theta}$ is recomputed using the value of the Jacobi constant, and the remaining coordinates are fixed at zero. In this case, the target function will be just the minimum distance between the initial state and the states at each of the crossings with the $\theta = 0$ plane. Mathematically, this can be expressed as:

$$f_{SLSQP} = \min\left(||\mathbf{s}|_{\theta=\mathbf{0}}(\tau) - \mathbf{s}_0||\right) \tag{7.4}$$

where the crossings with the $\theta = 0$ can be accurately found through the use of the *event* functionality of the $solve_{ivp}$ Python function, which makes use of a bisection technique combined with the RK45 propagation.

Once the function is minimized, a single candidate first guess for the coordinates (ρ, z) is attained. Furthermore, the epoch for which the minimum distance between states is achieved is also retrieved, to be used as the fist guess for the period of the orbit.

7.3.2. SINGLE-SHOOTING

Finally, the last step in the search for periodic orbit is a classical single-shooting algorithm. The input for this algorithm is of dimension seven: the initial state $\mathbf{s_0}$ plus the period of the orbit T. In essence, the single-shooting algorithm is a Boundary Value Problem (BVP) defined by the equations of motion (see Section 3.3), subject to the boundary constraints defined in Eq. (7.5) [46].

$$\mathbf{F}(\mathbf{s_0}, T) = \begin{bmatrix} \mathbf{g}(\mathbf{s_0}, \mathbf{s}(T)) \\ p(\mathbf{s_0}) \\ q(\mathbf{s_0}) \end{bmatrix} = 0 \tag{7.5}$$

where the functions $\mathbf{g}$, p, q are equivalent to the periodicity condition, the restriction of the initial conditions to a certain plane ($\theta = 0$) and the conservation of the Jacobi constant respectively. Mathematically, those are expressed as:

$$\mathbf{g}(\mathbf{s_0}, \mathbf{s}(T)) = \mathbf{s}(T) - \mathbf{s_0} \tag{7.6}$$

$$p(\mathbf{s_0}) = \theta_0 \tag{7.7}$$

$$q(\mathbf{s_0}) = C_j(\mathbf{s_0}) - C_{j,map} \tag{7.8}$$

In order to solve Eq. (7.5), a Newton-Raphson method is used, taking advantage of the knowledge of the analytic expression of the Jacobian of the equations of motion, presented in Eq. (3.18).

$$D\mathbf{F}(\mathbf{s_0}, T) = \begin{bmatrix} & \left[\Phi_{(T,0)} - \mathcal{I}_{6\times6}\right] & & & \dot{\mathbf{s}}(T) \\ 0 & 1 & 0 & \dots & 0 \\ & \left[\dfrac{\partial C_j}{\partial \mathbf{s}}(\mathbf{s_0})\right] & & & 0 \end{bmatrix} \tag{7.9}$$

Finally, the iterative Newton-Raphson method is implemented in Python as follows:

$$(\mathbf{s_0}, T)_{j+1} = (\mathbf{s_0}, T)_j - D\mathbf{F}_j^+ \cdot \mathbf{F}_j \tag{7.10}$$

where the matrix $D\mathbf{F}_j^+$ is the pseudo-inverse of the Jacobian of F evaluated at the initial state and period of the iteration j. The initial condition for state and period is the output of the SLSQP optimization of the previous step.

7.4. RESULTS

Following the novel methodology introduced in the previous sections, two periodic and stable orbits were found within the stability islands of QSO-M and QSO-L. Unfortunately, the algorithm did not yet succeed in converging into a periodic orbit for the stability island of QSO-H. The achieved orbits are able to reach higher latitudes than all of the periodic orbits encountered before, while still being robust against small perturbations. Hence, they provide a significant enhancement to the operations and scientific return of MMX.

7.4.1. MEDIUM QSO

In the case of QSO-M, about 50 km far from the center of Phobos and with $C_j = 3 - 0.0000289435706313$, the search space within the time-to-escape map in which the multi-objective minimization (see Section 7.2) was applied was restricted to the QSO-M stability island (see Fig. 5.7):

$$-0.0036 \leq \rho \leq -0.0028$$
$$0.0041 \leq z \leq 0.0044$$

The solutions to be found will always be located within the stability island of QSO-M and its surroundings. Regarding the implementation settings, a population of 20 individuals was selected and evolved over 2000 generations.

The resulting Pareto front and the location of the solutions on the time-to-escape map are presented in Fig. 7.2, where a specific region on the map is clearly defined. This region has therefore potential to hold a periodic QSO. As for the Pareto front, it seems clear that the candidate solutions populate a surface-like space where the points are roughly equidistant from the direction opposite to the improvement (shown by the black arrow), meaning that the optimization was successful.

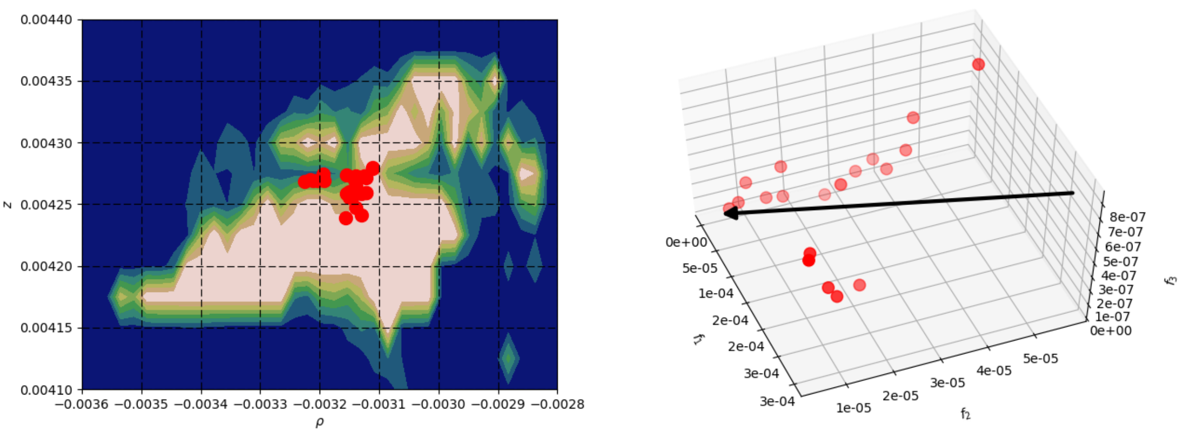

Figure 7.2: Results of the multi-objective optimization for QSO-M (left) and Pareto front (right). The black arrow indicates the direction for which all the objectives are improved at the same time.

Starting at the position ($\rho = -0.0033$, $z = 0.00427$), located within the region highlighted red in Fig. 7.2, the SLSQP algorithm (see Subsection 7.3.1) was initialized with a step tolerance of 10^{-14}, and it converged after 24 iterations and 96 function evaluations. The resulting optimal point, estimation for the period and function value are:

$$\rho = -0.0031053372705761$$
$$z = 0.0042782949920145$$
$$T = 7.6873272398058319\,\text{rev}$$
$$f_{SLSQP} = 4.46813639 \cdot 10^{-15}$$

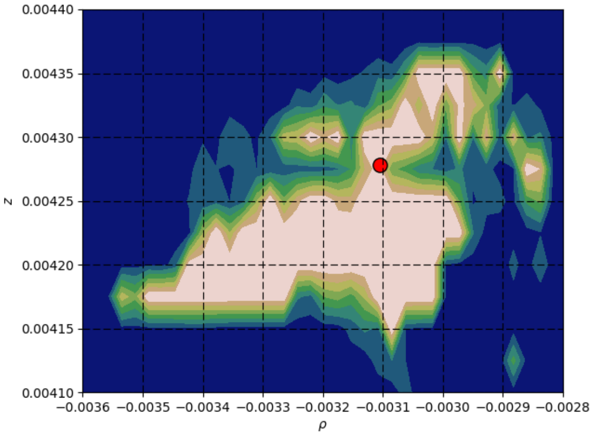

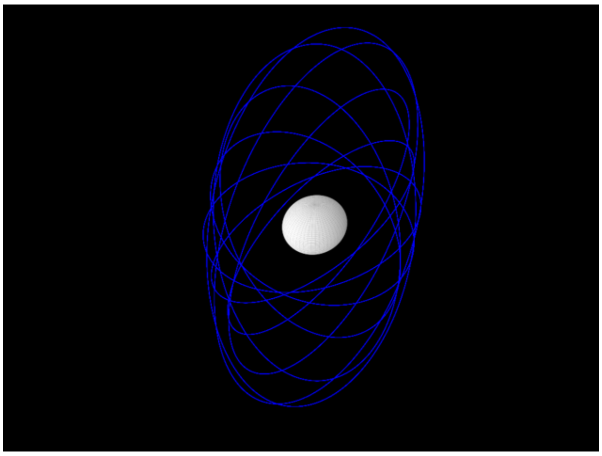

Figure 7.3: Initial conditions and trajectory found after SLSQP minimization, for QSO-M.

The location of the orbit found and its shape are presented in Fig.7.3. As shown, the orbit is already periodic, so the use of the conventional single-shooting technique seems to be redundant in this case. Nevertheless, it was initialized with these initial conditions for validation purposes and in order to show the limitations of classical shooting algorithms when compared to the new methodology proposed here. The single-shooting algorithm converged only after 212 iterations with a step tolerance of just 10^{-11}, even though the initial guess is clearly very close to the solution. The final solution found is:

$$
\begin{aligned}
\rho &= -0.003105342723228646 \\
\theta &= -3.807024523040921 \cdot 10^{-15} \\
z &= 0.004278291202264042 \\
\dot{\rho} &= 2.36956990382877 \cdot 10^{-9} \\
\dot{\theta} &= 0.0067343983803259391 \\
\dot{z} &= -1.872145916962639 \cdot 10^{-7} \\
T &= 7.68733020391094\,\text{rev} \\
||\mathbf{F}|| &= 1.179398 \cdot 10^{-11}
\end{aligned}
$$

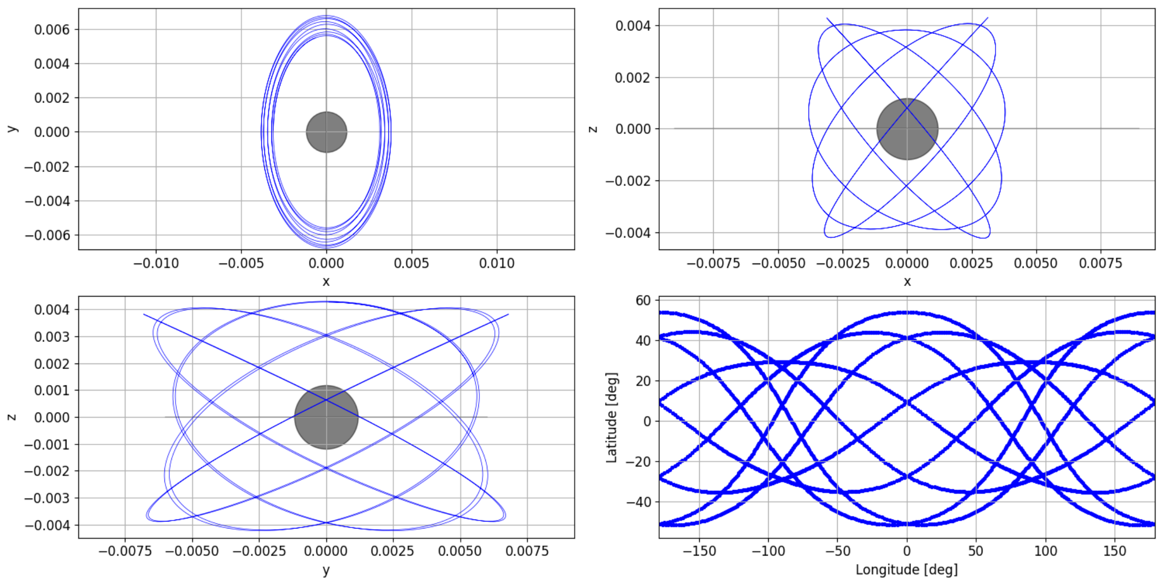

Figure 7.4: Projections of the periodic QSO found at the stability island of QSO-M.

The projections of the periodic trajectory found following the methodology exposed above are presented in Fig. 7.4. Note that the latitudes reached by this orbit are as high as 54°, well beyond all the periodic QSO's found so far. The evolution of the disturbing function and guiding center, as well as the detail of the motion of the peaks, are presented in Figs. 7.5 and 7.6. Note that the evolution of both disturbing function and guiding center are purely periodic and with equal period. In Fig. 7.6, the fact that the peaks of the disturbing function go below the value seen by the guiding center periodically is exposed. With respect to the evolution of the orbital parameters, shown in Fig. 7.7, the same periodic behavior was found.

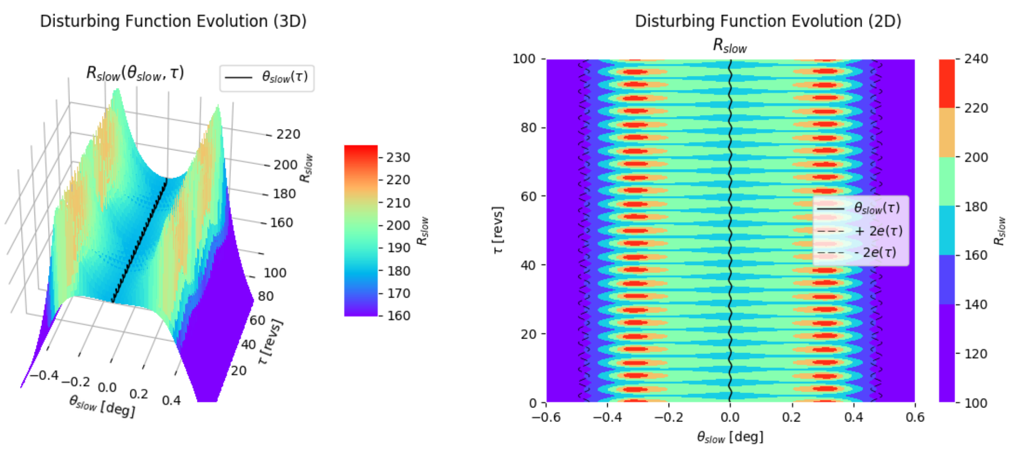

Figure 7.5: Motion of the guiding center and evolution of the disturbing function, for the periodic QSO found at the stability island of QSO-M.

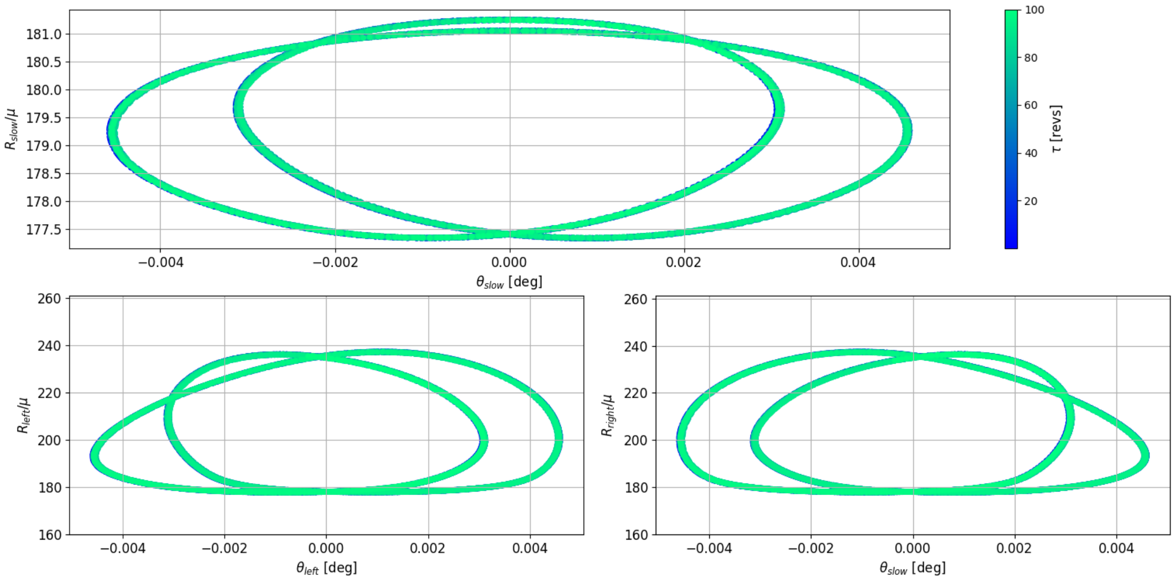

Figure 7.6: Value of the disturbing function seen by the guiding center (top) and value of the left and right maxima (bottom), as a function of the location of the guiding center in time.

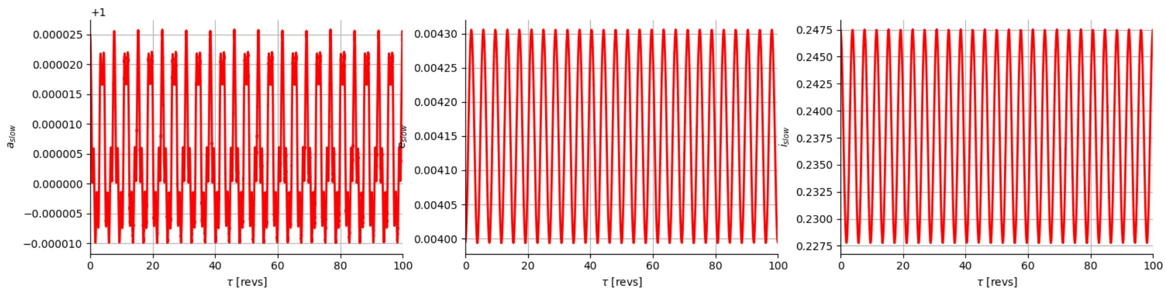

Figure 7.7: Slow evolution of the orbital parameters of the periodic QSO found at the stability island of QSO-M.

7.4.2. Low QSO

In the QSO-L time-to-escape map, located about 30 km from the center of Phobos and with a value of the Jacobi constant $C_j = 3 - 0.0000101835101867$, the stability island (see Fig. 5.8) is contained within the region:

$$
\begin{aligned}
-0.00315 \leq &\rho \leq -0.00225 \\
0.00135 \leq &z \leq 0.002
\end{aligned}
$$

Again, a random population of 20 individuals was generated in the area specified above and evolved over 2000 generations, arriving at the results presented in Fig. 7.8. The Pareto front again shows that the optimization has been successful, however in this case two different regions show up on the map. For the purpose of this thesis, only the region with the highest inclination and greater number of individuals was kept for further study. Note that the remaining few points from outside that region are located far away on the Pareto front. For those, the amplitude of the oscillations hardly varies, whereas the guiding center has a significantly higher velocity when the peaks of the function are at their lowest.

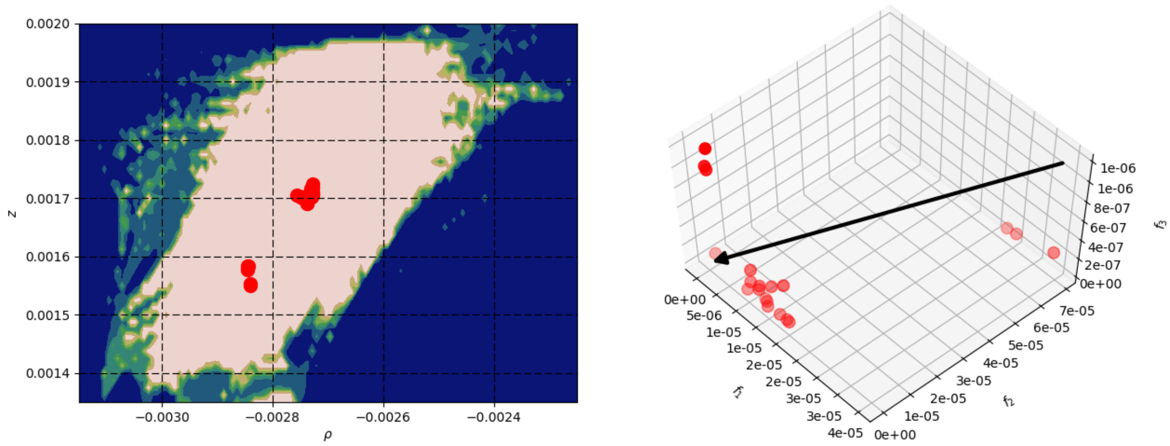

Figure 7.8: Results of the multi-objective optimization for QSO-L (left) and Pareto front (right). The black arrow indicates the direction for which all the objectives are improved at the same time.

After the multi-target optimization, the SLSQP algorithm was initialized starting at the location ($\rho = -0.00275$, $z = 0.0017$), at the center of the top region shown in Fig. 7.8, and with a tolerance of 10^{-14} again. After just 10 iterations and 40 function evaluations, the algorithm converged at the solution:

$$
\begin{aligned}
\rho &= -0.0027447381001587 \\
z &= 0.0016918289531681 \\
T &= 7.8690083990095125\,\text{rev} \\
f_{SLSQP} &= 4.127055319 \cdot 10^{-11}
\end{aligned}
$$

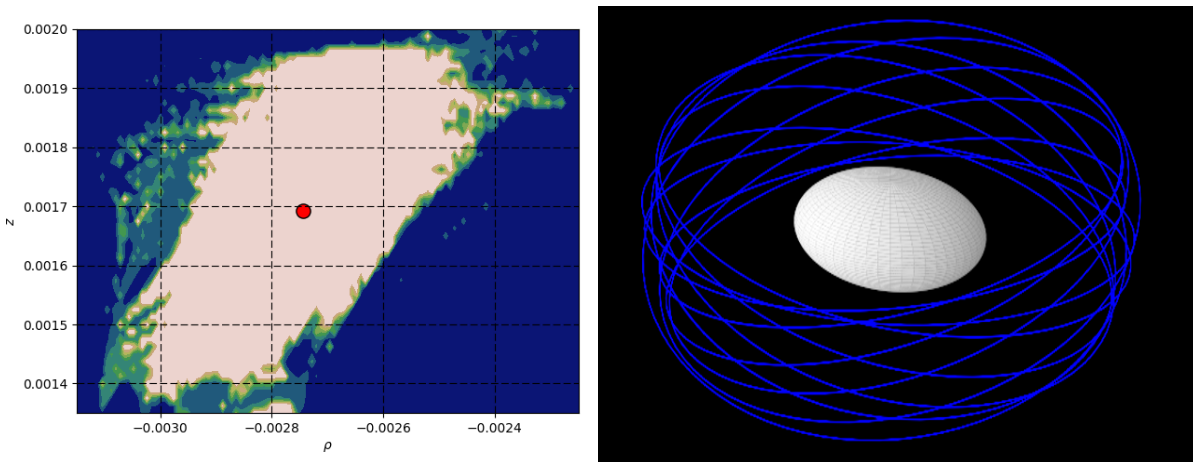

Figure 7.9: Initial conditions and trajectory found after SLSQP minimization, for QSO-L.

As in the previous case, the resulting orbit, shown in Fig. 7.9, seems to be already periodic, and the state is repeated with a tolerance in the order of 10^{-11}, meaning that in principle the final single-shooting technique is unnecessary. Nevertheless, the single-shooting converged with a step tolerance of 10^{-11} after 110 iterations, to the following solution:

$$
\begin{aligned}
\rho &= -0.0029686895747658448 \\
\theta &= 2.949975399645272 \cdot 10^{-14} \\
z &= -0.00019756841693771866 \\
\dot{\rho} &= 0.00010238408002831103 \\
\dot{\theta} &= 0.006714816468761156 \\
\dot{z} &= 0.0016697720480029566 \\
T &= 7.86874983265783\,\text{rev} \\
||\mathbf{F}|| &= 3.981440 \cdot 10^{-11}
\end{aligned}
$$

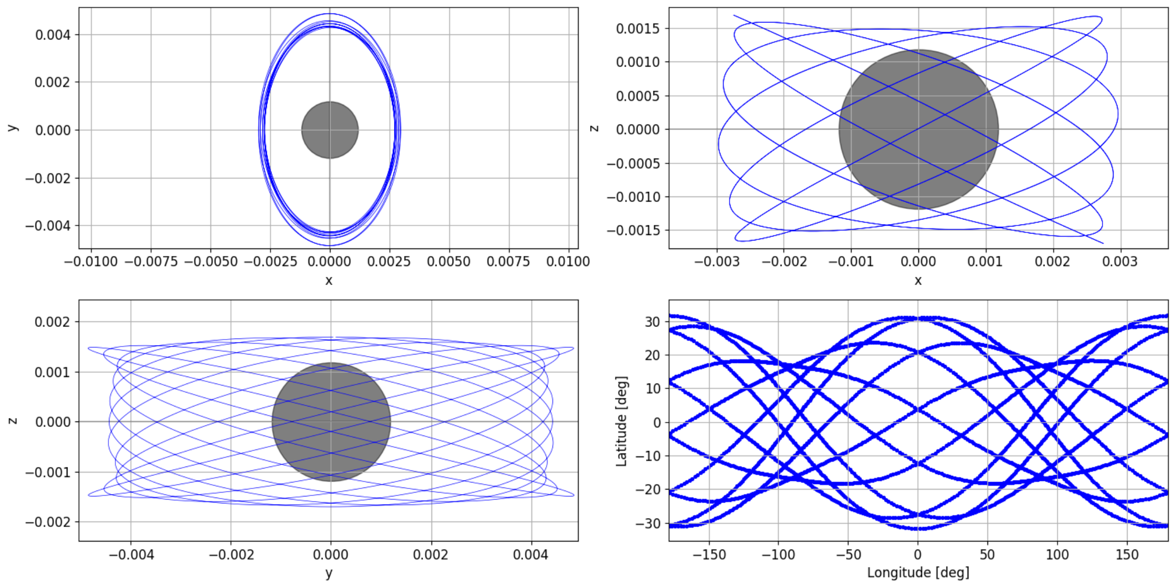

Figure 7.10: Projections of the periodic QSO found at the stability island of QSO-L.

The projections of the resulting periodic trajectory are shown in Fig. 7.10, where it can be seen that the resulting orbit reaches latitudes of about 32° in this case. Nevertheless, the distance to the surface is substantially smaller than in the case of the periodic orbit on the QSO-M island, meaning that the resolution attainable from this orbit is higher. As for the evolution of the disturbing function, the oscillations of the peaks are in this case asymmetric and sharper, as shown in Figs. 7.11 and 7.12. The sharpness of the peaks is actually the reason why the trace of the peaks shown in Fig. 7.12 seems not to be completely periodic, due to the limited resolution in computing R_{slow}. Finally, Fig. 7.13 shows the periodic nature of the evolution of the orbital elements governing the shape of the disturbing function.

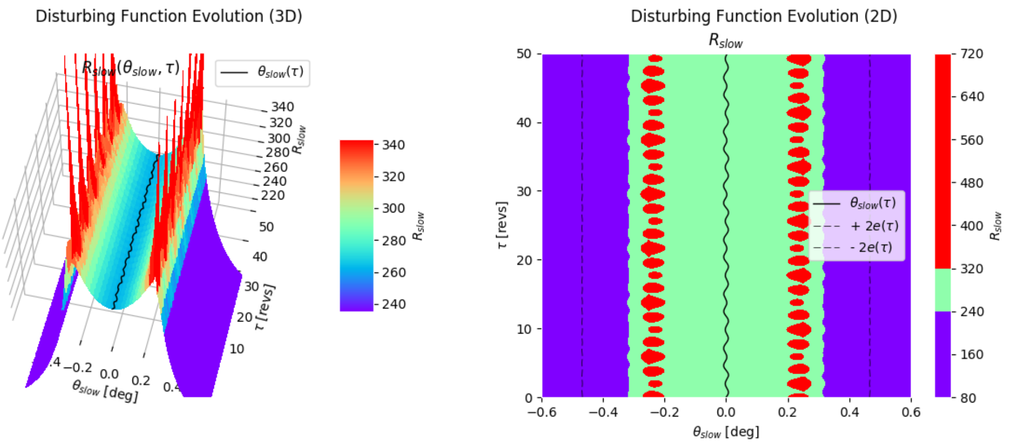

Figure 7.11: Motion of the guiding center and evolution of the disturbing function, for the periodic QSO found at the stability island of QSO-L.

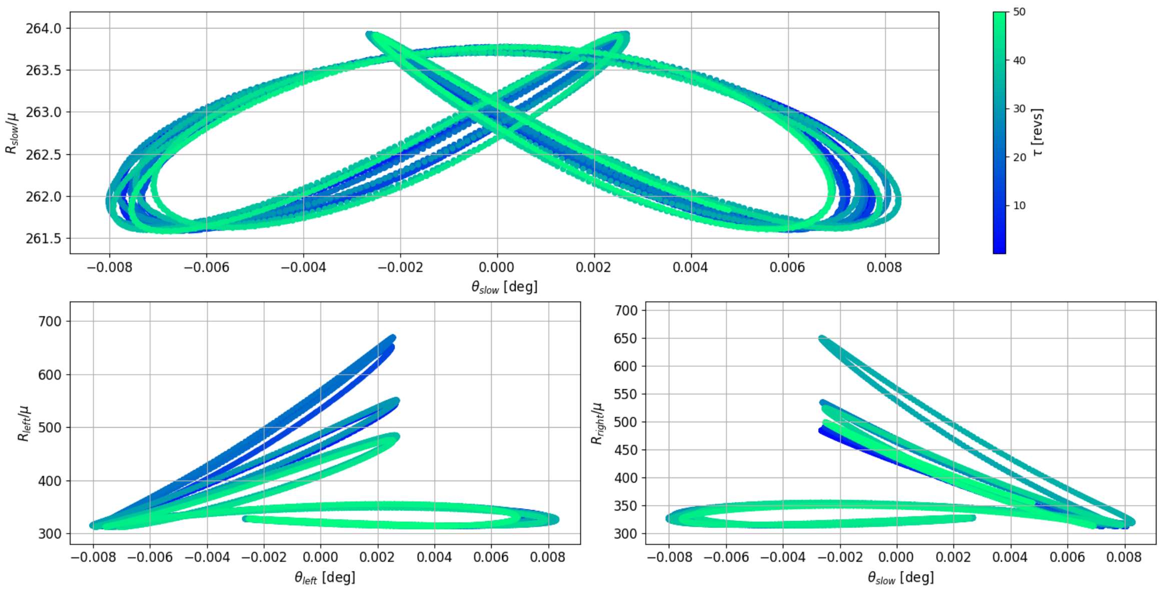

Figure 7.12: Value of the disturbing function seen by the guiding center (top) and value of the left and right maxima (bottom), as a function of the location of the guiding center in time.

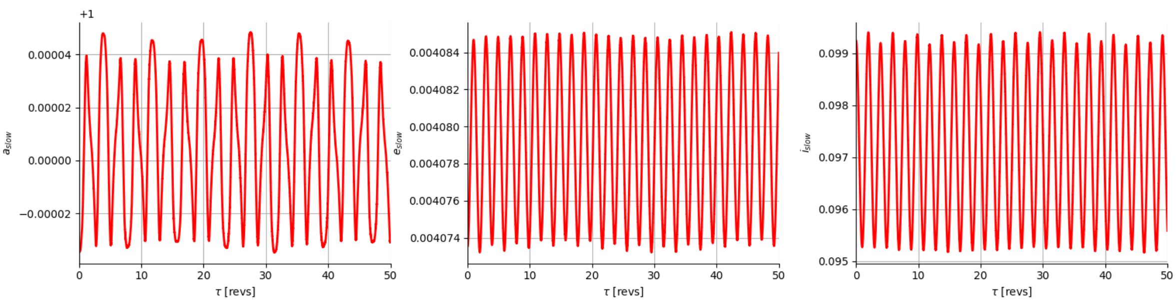

Figure 7.13: Slow evolution of the orbital parameters of the periodic QSO found at the stability island of QSO-L.

8

Conclusions

In the framework of the PPP of the MMX mission developed by JAXA, where Phobos will be characterized from orbit and a sample retrieval module will be launched to its surface, a stability analysis was conducted by making use of the co-orbital motion theory. As the final and most relevant result of this study, two periodic, highly-inclined and stable orbits were found at 50 and 30 km from the center of Phobos, allowing access to higher latitudes over the surface of the moon than any the periodic orbits found before. This result represents an important contribution to the mission design of MMX, providing not only an enhancement in the scientific return and robustness of the mission, but also a novel tool to obtain periodic orbits at high inclinations.

The PPP is one of the most critical phases of MMX, since orbiting Phobos is very challenging as its sphere of influence lays within its own surface. In this context, QSO are chosen as the most adequate solution to quasi-orbit the Martian moon in a stable and maintainable manner. Furthermore, for most of the duration of the PPP, planar QSO will be flown around Phobos, at distances of 100, 50 and 30 km from its center. These planar orbits received the names QSO-H, QSO-M and QSO-L respectively. Planar QSO dynamics are well understood and analytic relations are in general available, nevertheless they have the drawback of providing poor observability of the higher latitudes over the surface of the moon. To cope with this limitation, this thesis was focused on three-dimensional QSO's, aiming to assess the stability of these orbits and providing a safe alternative to the planar QSO already included in the baseline of MMX.

The analysis and methodologies proposed in this thesis are innovative in the sense that they make use of a co-orbital interpretation of the QSO dynamics, traditionally used to model the long-term evolution of asteroids and other astronomy features. In this work, however, this interpretation was applied to the actual orbit design of a real space mission such as MMX. This interpretation of the dynamics is based on the motion of the so-called guiding center of the spacecraft, which accounts for the long-term evolution of the position of the spacecraft. The guiding center moves under the effect of a disturbing potential, caused by the gravitational and inertial perturbation of Phobos. Thanks to the existence of a quasi-constant of this long-term motion, additional to the well-known Jacobi constant, the motion of the guiding center can be predicted to a certain extent, allowing to extract insights about the ballistic capture and escape phenomena.

After an introduction to the problem, the mathematical background and the motivation behind this work, a preliminary analysis of the three-dimensional QSO stability was conducted, introducing the concept of time-to-escape map. The time-to-escape map is nothing but a parametrization of the initial coordinates for a certain value of the Jacobi constant, where each condition is propagated over a long time, measuring the time that it takes for the spacecraft to leave the vicinity of Phobos. The correlation of this map with the existence of periodic orbits was then confirmed by overlapping them to the position of periodic three-dimensional QSO found via a bifurcation analysis already available in the literature.

Once the time-to-escape map, basis of this work, was computed and examined for the energy levels of QSO-H, QSO-M and QSO-L, a full analysis in terms of co-orbital motion was performed for orbits belonging to the three different regions distinguishable in each of the maps: stability continent, escape gap and stability island. By analyzing the results of this study, several conclusions were drawn about the escape condition. In particular, it was found that the escape at high inclination occurs due to the oscillations of the peaks of the disturbing potential, induced by changes in the eccentricity and inclination of the orbit. When the peaks decrease substantially, the guiding center is able to move freely, increasing the amplitude of its oscillations until it finally escapes. On stability islands this does not take place because the guiding center is located close to Phobos and with little velocity whenever the peaks are very low.

By exploiting these conclusions, a novel strategy to search for stable periodic orbits on stability islands was derived, based on a multi-objective optimization of the co-orbital parameters governing the escape condition, followed by a shooting technique. With the multi-objective minimization, the areas on the time-to-escape map which are likely to hold a periodic orbit are highlighted. By setting a first guess located at one of those regions, the shooting algorithm is able to converge reaching the periodic and stable orbit in question, if existing. This methodology was successfully tested on the stability islands of QSO-M and QSO-L, leading to the discovery of two periodic QSO able to reach latitudes of 54° and 32° respectively, way beyond the latitudes attainable by the periodic orbits found prior to this study.

The contribution of the present study to the development of the PPP of MMX is twofold. On the one hand, two periodic and stable orbits were found at the desired distances from the center of Phobos, with the enhancing feature of having a high inclination. This directly implies an enhancing of the scientific return of the mission. Indirectly, it implies that MMX will be able to model more adequately the gravity field and shape of Phobos before performing critical operations such as landing and sample return. Since the navigation or the spacecraft relies on this model, one could argue that this result will improve the operational robustness and safety of MMX. On the other hand, new methodologies and tools were proposed, able to find periodic and stable orbits as well as to assess the stability in an innovative fashion. This contribution might be relevant not only for MMX but also for different missions or applications in different planetary systems.

9

RECOMMENDATIONS

Throughout the development of this thesis, several aspects with potential to be researched in further studies were identified. Because of time constraints, these were not included in this investigation, but they will be briefly summarized here as recommendations for further work.

First, the time-to-escape map was found to be a very useful tool to assess the stability of out-of-plane orbits. However, it requires a long-time propagation of a large set of different initial conditions, which was found to be demanding even implementing it a multi-processing fashion. In order to extract additional insights, the resolution of the maps was already achieved to be improved by applying available machine-learning algorithms, such as decision trees, as means of an interpolation, with very little error especially far from the boundaries of the stable regions. A further study proposed here is to apply similar algorithms to achieve three-dimensional maps where, for instance, a position could be determined by the three values (ρ, z, C_j). With this, a mission designer could have a continuous set of energy levels in which finding the most suitable orbit for the application in question would be more likely.

Second, and also related to the limitations in the computation of the time-to-escape map, the optimization algorithm proposed to find periodic three-dimensional QSO's was only tested for the energy levels of QSO-M and QSO-L. In order to generalize the tool to the whole range of energy levels between these two, it should be applied for more intermediate cases between the QSO-M and QSO-L energy levels. Also, to find the range of applicability of the method, energy levels lower and beyond those should be tested, to check when finding a periodic orbit is no longer possible. A further generalization of the method could also be attained by applying it to different CR3BP systems with scientific interest, such as the Mars-Deimos, Earth-Moon, Sun-Earth or Sun-Jupiter systems.

Third, the methodology proposed to find periodic orbits could be further improved by coming up with an adequate set of weighting coefficients, converting the multi-objective minimization into a single-objective one. For this, the regions on the time-to-escape map identified by the multi-objective step should be linked to their position on the Pareto front, highlighting those regions where an actual periodic orbit was found. A possibility here is for the selection of the most adequate weighting coefficients to be a function of the energy level. If that were the case, an algorithm able to interpolate accurately the most suitable set of weighting coefficients with the value of the Jacobi constant as the single input would be a valuable contribution.

Fourth, the resulting periodic orbits that were found within the stability islands were not tested against perturbations. In order to do so, first a sensitivity analysis is recommended for small deviations of the initial conditions in any direction[1]. Then, a natural step would be increasing the complexity of the model. In particular, including additional effects such as the effect of the moon's eccentricity (ER3BP) or the spherical harmonics of the moon's gravity would be very valuable for the applicability of the results to MMX, given their important effect on the dynamics close to Phobos.

[1] Note that small deviations in ρ and z are affordable, since the orbits are located within a stability region in the time-to-escape maps.

Finally, if the proposed orbits were to be flown by MMX, a study about the ΔV required to arrive at those in an optimal way would be required. On top of that, a trade-off would likely be needed between the robustness of the transfer against errors like miss-thrust or thrust miss-alignment, and the amount of propellant required. For these two, co-orbital analysis is recommended as an additional tool to incorporate to the study, because of its potential to attain overall insights about the dynamics such as the ones achieved in the present work.

Bibliography

[1] F. Namouni, *Secular interactions of coorbiting objects,* Icarus **137**, 293 (1999).

[2] Y. Kawakatsu, K. Kuramoto, N. Ogawa, H. Ikeda, Y. Mimasu, G. Ono, H. Sawada, K. Yoshikawa, T. Imada, H. Otake, H. Kusano, K. Yamada, M. Otsuki, and M. Baba, *Mission Concept of Martian Moons Exploration (MMX),* in *Proceedings in the 68th International Astronautical Congress* (2017).

[3] M. Yoshikawa, A. Fujiwara, and J. Kawaguchi, *Hayabusa and its adventure around the tiny asteroid Itokawa,* Proceedings of the International Astronomical Union **2**, 323 (2006).

[4] S.-i. Watanabe, Y. Tsuda, M. Yoshikawa, S. Tanaka, T. Saiki, and S. Nakazawa, *Hayabusa2 mission overview,* Space Science Reviews **208**, 3 (2017).

[5] I. De Pater and J. J. Lissauer, *Planetary sciences* (Cambridge University Press, 2015).

[6] M. Zamaro, *Natural and artificial orbits around the Martian moon Phobos*, Ph.D. thesis, University of Strathclyde (2015).

[7] J. Oberst, A. Zakharov, and R. Schulz, *Why study Phobos and Deimos? An introduction to the special issue,* Planetary and Space Science **102**, 1 (2014).

[8] E. V. Bell, *Phobos Project Information,* NSSDCA NASA Goddard Space Flight Center (2016).

[9] R. Z. Sagdeev and A. V. Zakharov, *Brief history of the Phobos mission,* Nature **341**, 581 (1989).

[10] G. Avanesov, B. Bonev, F. Kempe, A. Bazilevsky, V. Boycheva, K. Chikov, M. Danz, D. Dimrtrov, T. Duxbury, P. Gromatikov, *et al.*, *Television observations of Phobos,* Nature **341**, 585 (1989).

[11] M. Y. Marov, V. Avduevsky, E. Akim, T. Eneev, R. Kremnev, S. Kulikov, K. Pichkhadze, G. Popov, and G. Rogovsky, *Phobos-Grunt: Russian sample return mission,* Advances in Space research **33**, 2276 (2004).

[12] P. Lee, *First International Conference on the Exploration of Phobos and Deimos, 5-7 Nov 2007: Summary and Recommendations,* Mars Institute Technical Publication **1** (2009).

[13] T. McElrath, N. Strange, and J. Lang, *Phobos and Deimos Sample Return to Earth-Moon L2 using Small SEP Spacecraft in 2018-2023,* in *Concepts and Approaches for Mars Exploration*, Vol. 1679 (2012).

[14] P. Lee, M. Benna, D. Britt, A. Colaprete, W. Davis, G. Delory, R. Elphic, E. Fulsang, A. Genova, D. Glavin, *et al.*, *PADME (Phobos and Deimos and Mars Environment): A Proposed NASA Discovery Mission to Investigate the Two Moons of Mars,* in *46th Lunar and Planetary Science Conference* (2015).

[15] J. Oberst, K. Wickhusen, K. Willner, K. Gwinner, S. Spiridonova, R. Kahle, A. Coates, A. Herique, D. Plettemeier, M. D. Michelena, *et al.*, *DePhine: The Deimos and Phobos Interior Explorer,* Advances in Space Research **62**, 2220 (2018).

[16] S. F. Singer, *Origin of the Martian satellites Phobos and Deimos,* in *Exploration of Phobos and Deimos*, Vol. 1377 (2007) p. 36.

[17] S. L. Murchie, D. T. Britt, J. W. Head, S. F. Pratt, P. C. Fisher, B. S. Zhukov, A. A. Kuzmin, L. V. Ksanfomality, A. V. Zharkov, G. E. Nikitin, *et al.*, *Color heterogeneity of the surface of Phobos: Relationships to geologic features and comparison to meteorite analogs,* Journal of Geophysical Research: Solid Earth **96**, 5925 (1991).

[18] J. A. Burns, *The dynamical evolution and origin of the Martian moons,* Vistas in Astronomy **22**, 193 (1978).

[19] J. B. Pollack, J. A. Burns, and M. E. Tauber, *Gas drag in primordial circumplanetary envelopes: A mechanism for satellite capture,* Icarus **37**, 587 (1979).

[20] D. M. Hunten, *Capture of Phobos and Deimos by photoatmospheric drag,* Icarus **37**, 113 (1979).

[21] S. Sasaki, *Origin of Phobos–Aerodynamic Drag Capture by the Primary Atmosphere of Mars,* in *Lunar and Planetary Science Conference*, Vol. 21 (1990).

[22] R. I. Citron, H. Genda, and S. Ida, *Formation of Phobos and Deimos via a giant impact,* Icarus **252**, 334 (2015).

[23] P. Rosenblatt, S. Charnoz, K. M. Dunseath, M. Terao-Dunseath, A. Trinh, R. Hyodo, H. Genda, and S. Toupin, *Accretion of Phobos and Deimos in an extended debris disc stirred by transient moons,* Nature Geoscience **9**, 581 (2016).

[24] M. Wallace, J. Parker, N. Strange, and D. Grebow, *Orbital operations for Phobos and Deimos exploration,* in *AIAA/AAS Astrodynamics Specialist Conference* (2012) p. 5067.

[25] C. Bezrouk and J. S. Parker, *Ballistic capture into distant retrograde orbits around Phobos: an approach to entering orbit around Phobos without a critical maneuver near the moon,* **130**, 10.

[26] P. J. Gil and J. Schwartz, *Simulations of quasi-satellite orbits around Phobos,* Journal of Guidance, Control, and Dynamics **33**, 901 (2010).

[27] M. Lara, *Nonlinear librations of distant retrograde orbits: a perturbative approach—the Hill problem case,* Nonlinear Dynamics , 1 (2018).

[28] E. Canalias, L. Lorda, T. Martin, J. Laurent-Varin, J. C. Marty, and Y. Mimasu, *Trajectory analysis for the Phobos proximity phase of the MMX mission,* 26th International Symposium on Space Flight Dynamics (ISSFD) (2017).

[29] M. Giancotti, S. Campagnola, Y. Tsuda, and J. Kawaguchi, *Families of periodic orbits in Hill's problem with solar radiation pressure: application to Hayabusa 2,* Celestial Mechanics and Dynamical Astronomy **120**, 269 (2014).

[30] R. L. Anderson, S. Campagnola, and G. Lantoine, *Broad search for unstable resonant orbits in the planar circular restricted three-body problem,* Celestial Mechanics and Dynamical Astronomy **124**, 177 (2016).

[31] E. Canalias, L. Lorda, and J. Laurent-Varin, *Design of realistic trajectories for the exploration of Phobos,* in *2018 Space Flight Mechanics Meeting* (2018) p. 0716.

[32] C. Bombardelli, J. L. Gonzalo, and J. Roa, *Approximate solutions of non-linear circular orbit relative motion in curvilinear coordinates,* Celestial Mechanics and Dynamical Astronomy **127**, 49 (2017).

[33] C. Bombardelli and P. Bernal Mencia, *The circular restricted three body problem in curvilinear coordinates,* Celestial Mechanics and Dynamical Astronomy (accepted, 2018).

[34] R. H. Battin, *An introduction to the mathematics and methods of astrodynamics* (AIAA, 1999).

[35] K. Oshima, *The roles of L_4 and L_5 axial orbits in transport among co-orbital orbits,* Monthly Notices of the Royal Astronomical Society (accepted, 2018).

[36] C. Yoder, G. Colombo, S. Synnott, and K. Yoder, *Theory of motion of Saturn's coorbiting satellites,* Icarus **53**, 431 (1983).

[37] M. Morais, *A secular theory for Trojan-type motion,* Astronomy and Astrophysics **350**, 318 (1999).

[38] P. Wajer, *2002 AA29: Earth's recurrent quasi-satellite?* Icarus **200**, 147 (2009).

[39] A. Pousse, P. Robutel, and A. Vienne, *On the co-orbital motion in the planar restricted three-body problem: the quasi-satellite motion revisited,* Celestial Mechanics and Dynamical Astronomy **128**, 383 (2017).

[40] M. Lara, R. Russell, and B. F. Villac, *Classification of the distant stability regions at Europa,* Journal of Guidance, Control, and Dynamics **30**, 409 (2007).

[41] Y. Kozai, *Second-order solution of artificial satellite theory without air drag,* The Astronomical Journal **67**, 446 (1962).

[42] C. D. Murray and S. F. Dermott, *Solar system dynamics* (Cambridge University Press, 1999).

[43] A. Boryssenko and N. Herscovici, *Machine Learning for Multiobjective Evolutionary Optimization in Python for EM Problems,* in *IEEE International Symposium on Antennas and Propagation and USNC-URSI Radio Science Meeting*, Vol. 8 (2018) p. 13.

[44] K. Deb, A. Pratap, S. Agarwal, and T. Meyarivan, *A fast and elitist multiobjective genetic algorithm: NSGA-II,* IEEE transactions on evolutionary computation **6**, 182 (2002).

[45] F. J. Blanco-Silva, *Learning SciPy for Numerical and Scientific Computing* (Packt Publishing Ltd, 2013).

[46] N. Baresi, *Spacecraft Formation Flight on Quasi-periodic Invariant Tori*, phdthesis (2017).

A

VALIDATION

There are several expressions and algorithms developed and implemented by the author throughout this report which required to be validated prior to using them in the actual development of the thesis. This appendix aims to summarize the methodology used to perform the validation. In particular, only three different kind of tools required to be validated: Orbit propagation, coordinate transformations and numerical averaging. The remaining algorithms either made use of open-source and validated Python libraries (e.g. optimization tools) or were easy to validate visually (e.g. graphic tools).

A.1. ORBIT PROPAGATION

The correct implementation of the equations of motion provided in Chapter 3 was validated in two different ways:

- By monitoring the evolution of the Jacobi constant, whose expression is also provided in Chapter 3. Since this is a known first integral of the problem, it is known to remain constant along the propagated time. For this, the standard deviation of C_j divided by its mean value was used as Key Performance Index (KPI) (see Eq. (A.1)). This parameter was always found to be substantially smaller than 10^{-12}, which was the tolerance used for the RK45 numerical integrator.

$$KPI_{prop,1} = \frac{\sigma\left(C_j\right)}{C_{j,mean}} \leq \epsilon \tag{A.1}$$

- By comparing the results when propagating the orbit using the classical Cartesian formulation of the dynamics (Section 3.2) and propagating it with the less common curvilinear coordinates used throughout most of the work (Section 3.3). As shown in Eq. (A.2), the KPI was the maximum norm of the difference between the states obtained at each epoch through both implementations, after a conversion of the curvilinear coordinates into Cartesian ones:

$$KPI_{prop,2} = \max\left(||\mathbf{s}_{cart} - \mathbf{s}_{curv}||\right) \leq \epsilon \tag{A.2}$$

The final propagation time was set at 1000 Phobos revolutions, larger than any of the propagations shown in this report. An orbit for each of the three QSO energy levels and regions (9 in total) was subjected to this validation, and in all cases the maximum deviation was way bellow 10^{-12}, the numerical error of the integration algorithm.

A.2. COORDINATE TRANSFORMATIONS

An important unit in the software developed involved transformations between the three sets of coordinates used: Cartesian, curvilinear and Kepler elements. The equations that allow these transformations are provided in [32] and [33]. To validate the adequate implementation of those, the check performed was simply to perform a double transformation in both directions. This implies performing three tests in total:

- Transformation from Cartesian to curvilinear coordinates and vice versa.
- Transformation from Cartesian coordinates to Kepler elements and vice versa.
- Transformation from curvilinear coordinates to Kepler elements and vice versa.

The KPI was again the maximum norm of the difference between the initial state and the final one after performing a double transformation, as shown in Eq. (A.3). The error in this case was always in the order of the numerical error of Python, since the tolerance of the propagation does not intervene in this check.

$$KPI_{trans} = \max\left(||\mathbf{s}_{initial} - \mathbf{s}_{final}||\right) \leq \epsilon \tag{A.3}$$

A.3. NUMERICAL AVERAGING

Finally, the numerical averaging algorithm was validated visually, by overlapping the full (fast and slow) time evolution of the curvilinear coordinates and orbital elements to the time evolution of the slow component. Some of the results (one for each level of energy) are presented in Figs. A.1 to A.6. As shown, the averaged value (shown in blue) is always located at the center of the fast oscillations, and it follows the long-term evolution of the coordinates.

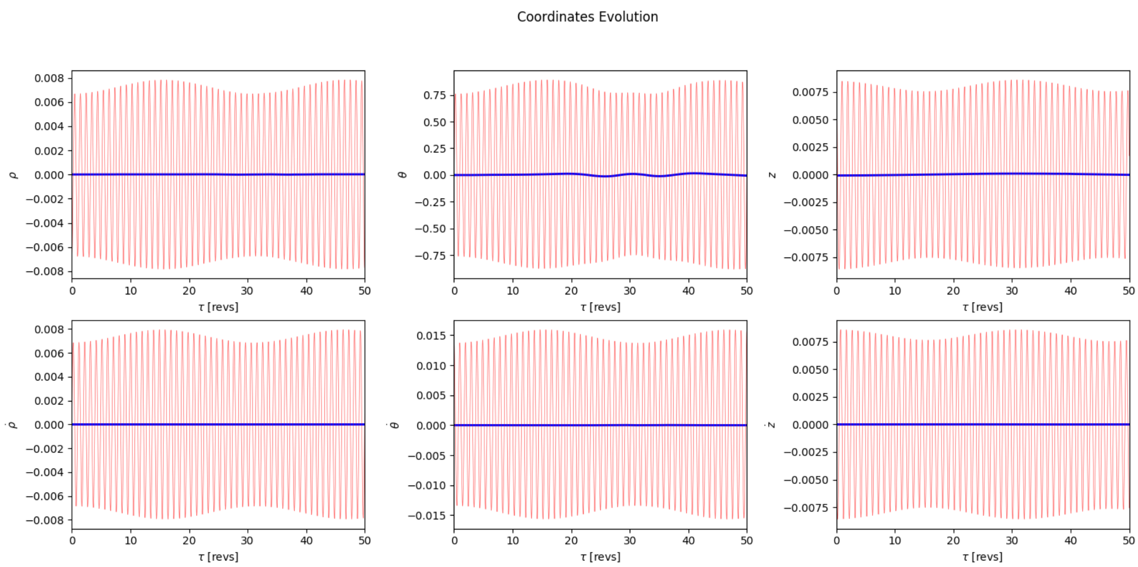

Figure A.1: Visual validation of the numerical averaging of the curvilinear coordinates, for a QSO on the stability island of QSO-H.

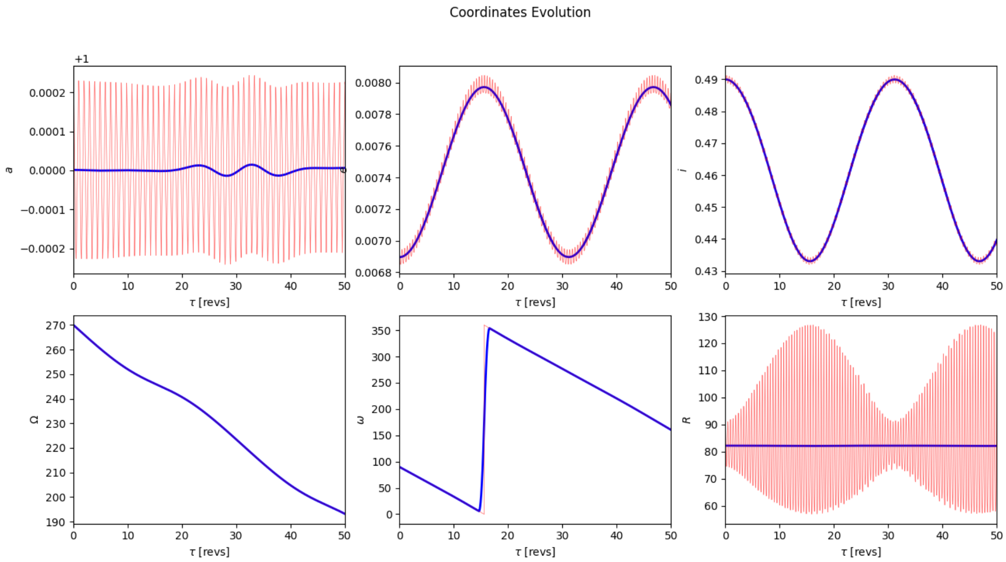

Figure A.2: Visual validation of the numerical averaging of the orbital elements, for a QSO on the stability island of QSO-H.

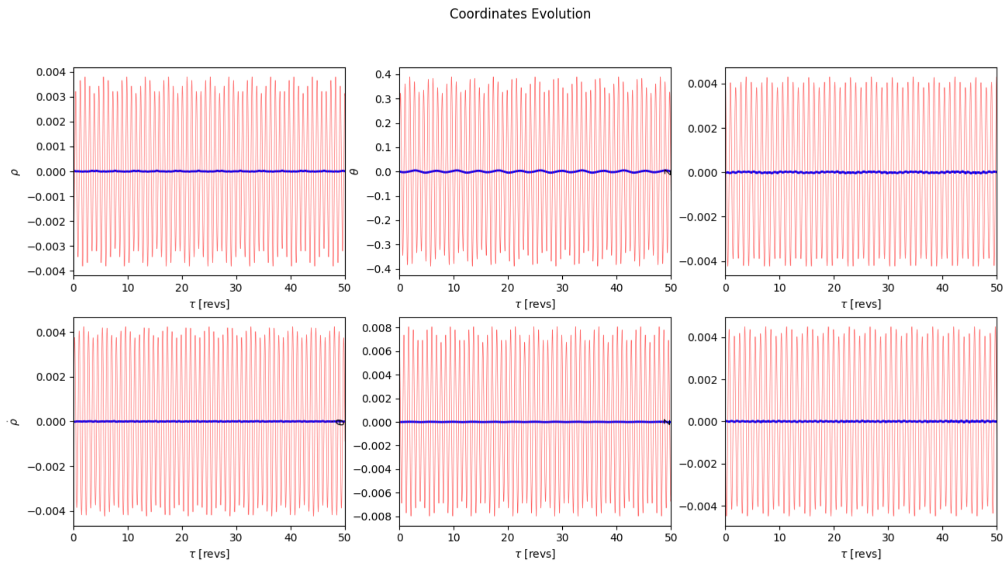

Figure A.3: Visual validation of the numerical averaging of the curvilinear coordinates, for a QSO on the stability island of QSO-M.

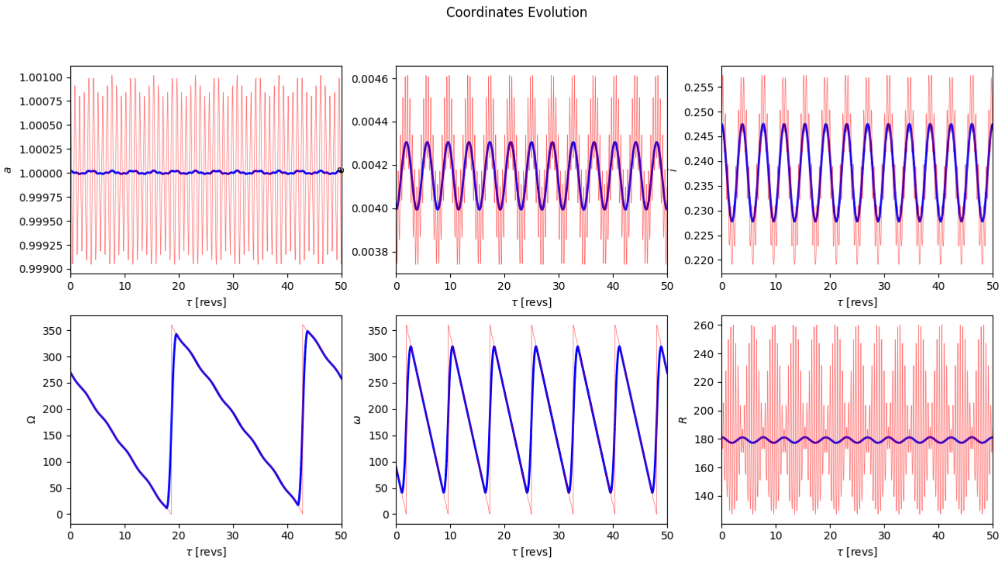

Figure A.4: Visual validation of the numerical averaging of the orbital elements, for a QSO on the stability island of QSO-M.

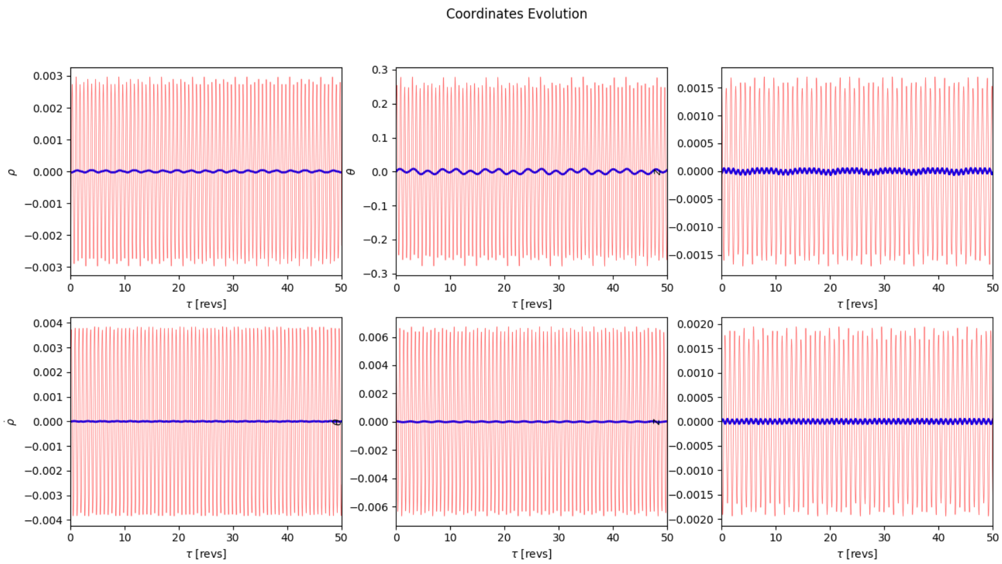

Figure A.5: Visual validation of the numerical averaging of the curvilinear coordinates, for a QSO on the stability island of QSO-L.

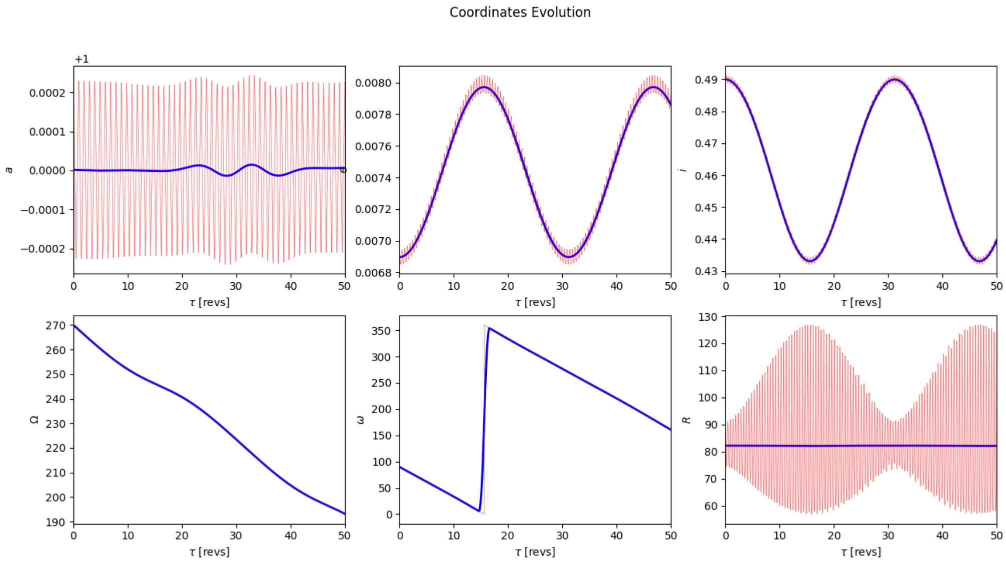

Figure A.6: Visual validation of the numerical averaging of the orbital elements, for a QSO on the stability island of QSO-L.

B

CO-ORBITAL ANALYSIS: ADDITIONAL FIGURES

In this appendix, some additional figures from the co-orbital analysis of three-dimensional QSO conducted in Chapter 6 can be found. These figures omitted from the main body for simplicity and to avoid repetition.

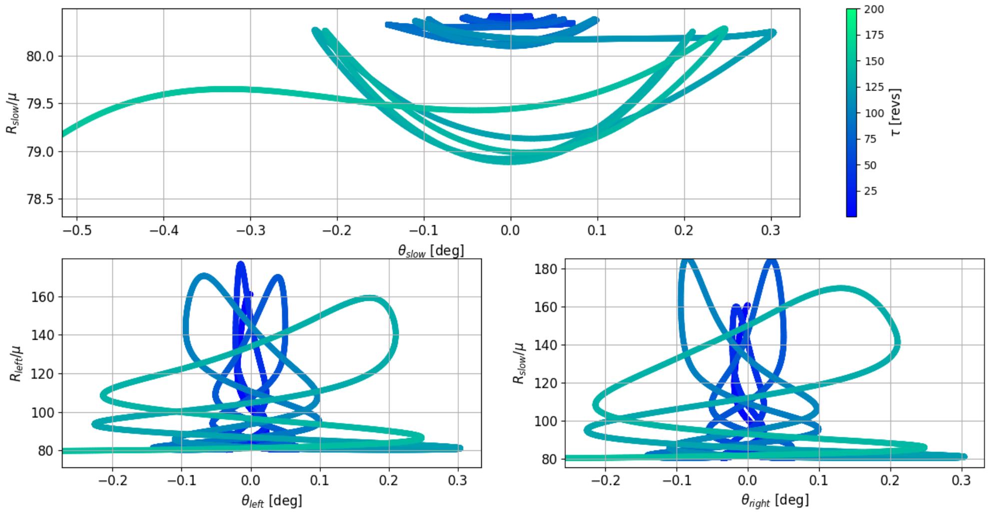

Figure B.1: Value of the disturbing function seen by the guiding center (top) and value of the left and right maxima (bottom), as a function of the location of the guiding center in time.

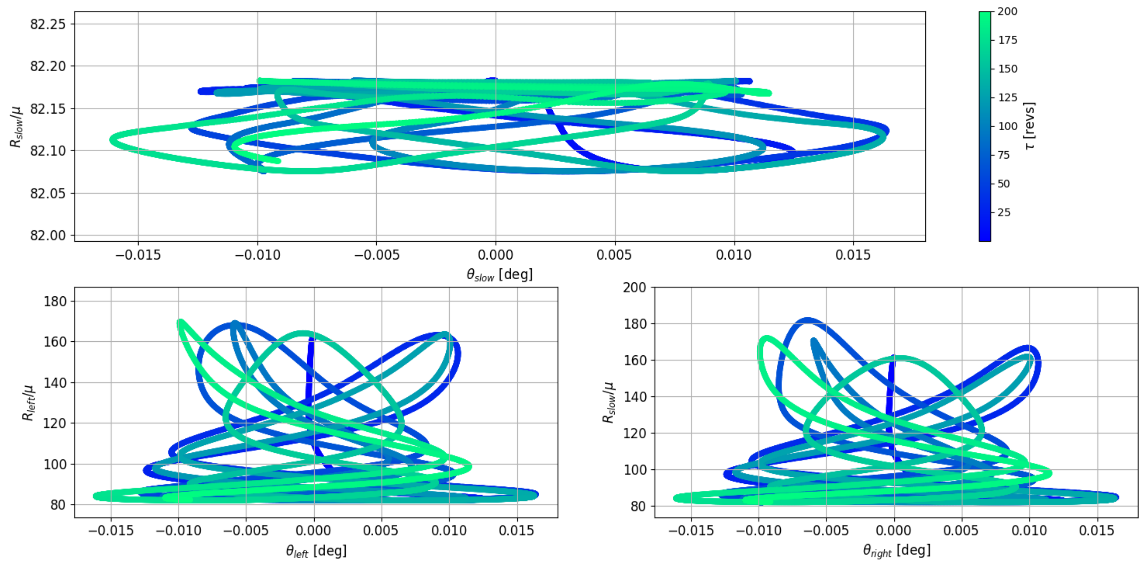

Figure B.2: Value of the disturbing function seen by the guiding center (top) and value of the left and right maxima (bottom), as a function of the location of the guiding center in time.

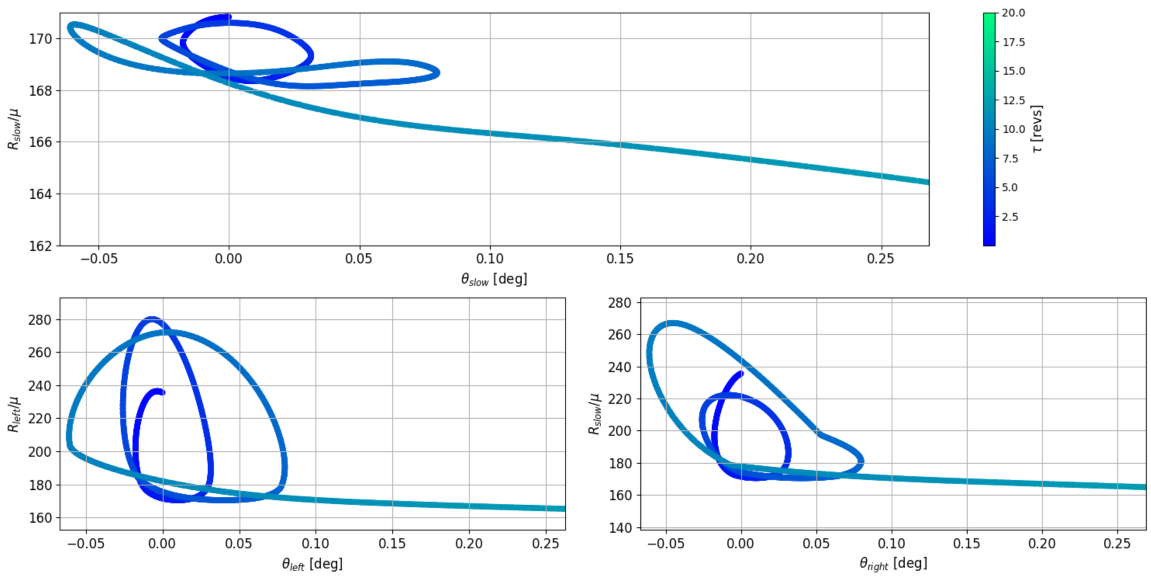

Figure B.3: Value of the disturbing function seen by the guiding center (top) and value of the left and right maxima (bottom), as a function of the location of the guiding center in time.

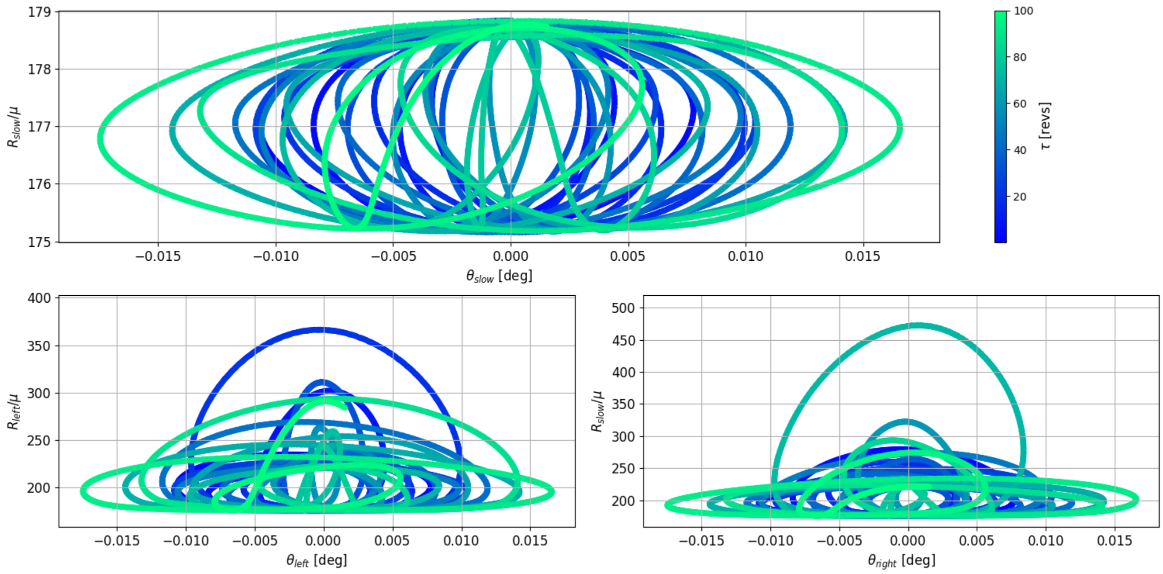

Figure B.4: Value of the disturbing function seen by the guiding center (top) and value of the left and right maxima (bottom), as a function of the location of the guiding center in time.

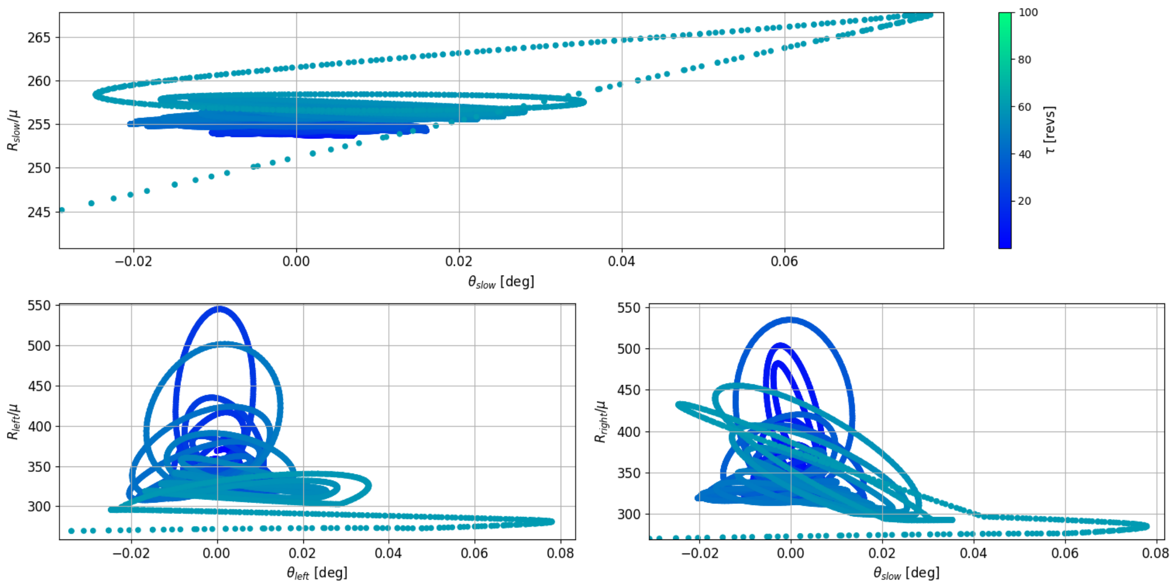

Figure B.5: Value of the disturbing function seen by the guiding center (top) and value of the left and right maxima (bottom), as a function of the location of the guiding center in time.

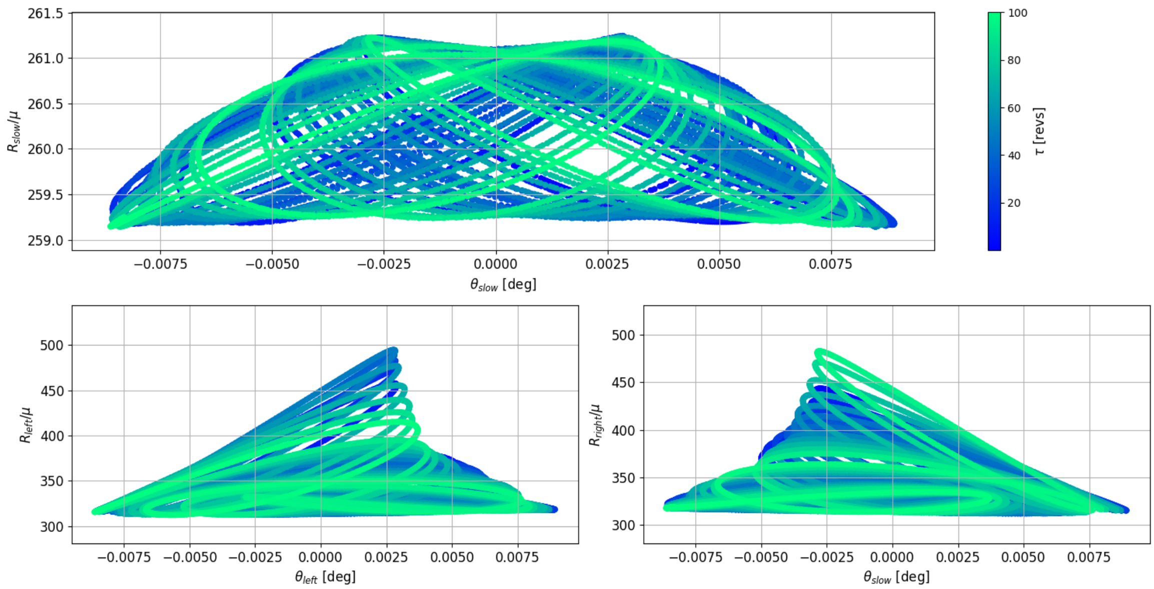

Figure B.6: Value of the disturbing function seen by the guiding center (top) and value of the left and right maxima (bottom), as a function of the location of the guiding center in time.